

# **Multi-Sensor Synergy For Persistent Scatterer Interferometry Based Ground Subsidence Monitoring**

## **Dissertation**

Zur Erlangung des akademischen Grades doctor rerum naturalium

(Dr. rer. nat.)

vorgelegt dem Rat der Chemisch-Geowissenschaftlichen Fakultät der  
Friedrich-Schiller-Universität Jena

von M.Sc. Nesrin Salepci  
geboren am 25.05.1981 in Çankırı, Türkei



Gutachter:

1. Prof. Dr. Christiane Schmallius, Jena
2. Dr. rer. nat. habil. Christian Thiel, Jena

Tag der Verteidigung: 11. Februar 2015



*To my parents, who made it possible...*



# Acknowledgments

Without the guidance and support of many people, the completion of this dissertation would not have been possible. For this reason, I would like to acknowledge their contribution.

I would like to express my deep gratitude to Prof. Dr. Christiane Schmallius for giving me the opportunity to pursue this research and for supporting me on this path. Her valuable advices and comments have inspired and guided this work through the years. I sincerely thank Dr. habil. Christian Thiel for his constant guidance and support as well as for the provision of the thrilling research topic. His profound vision of radar remote sensing has guided me all the way long and his valuable comments helped me to focus in crucial issues. I am very grateful for his trust in my abilities that lifted my spirit in the moments of doubt.

Very special thanks go to Arvid Kühl who has been a trustworthy and supportive companion in the course of INFLUINS. He helped me out in many ways including methodological developments and implementations such as surveying data processing, weather scoring and outlier removal. I owe him a debt of gratitude for the cooperative work that thrived into this thesis.

Refinement with synergy is a true story! The corrections and constructive suggestions from Robert Eckardt and Christian Berger significantly improved the final version of the thesis. I feel that words are finite to express my gratitude to Robert for his manifold support, including proof-reading of the manuscript, German translation of the abstract, offering his garden for working in the summer days and making tea. I am deeply indebted to him for being the closest, most critical and supportive companion in such a stressful time. I wholeheartedly thank you, Robs, for the times they are a-changin. I am very grateful to Christian for sharing his artistic LaTeX templates and his support on any kind of related issues. I appreciate a lot his constructive comments that improved the final version of the manuscript. Bärli, you are a true color!

I would like to thank Julian Schwilk and John Truckenbrodt for their assistance during the preparation of the scripts and data processing. I am obliged to my colleagues and friends who supported me in many different ways through the last years. Ralf Knuth, Claudia Hilbert, Tanvir Ahmed Chowdhury, Nicolas Ackermann, Martyna Stelmaszczuk-Górska, Mikhail Urbazhev, Sebastian Wilhelm and many others are sincerely thanked

for their comments, suggestions and contributions. I am also very grateful to Annett Habenstein who helped me a lot in administrative duties.

I thank all other fellow citizens of INFLUINS for the fruitful discussions and for their cooperation. I would like to also acknowledge GSES mbH, GVV mbH and TLUG for their collaboration and for providing the essential supplementary data.

I would like to send all my love to my friends who were always by my side through the way to the completion of this work. I profoundly thank Laurent Chevillard for his support by all means. I send him my tenderness and gratefulness for his delicious food and for his generosity of offering me an awesome environment in Lyon for working as well as for the leisure.

I would not be where I am without my family. I wish to express my indebtedness and heartfelt thanks to my parents, Zeliha & Hasan, to my dear sisters, Yasemin & Nermin and cousin-sister, Güneş for their endless support and love. I send all my love to the young spirits of the family, my beloved niece and nephew, Ece & Şafak. Thank you all for everything!

Jena, new moon in Libra, September 24, 2014



# Abstract

Ground subsidence is a common phenomenon which causes disturbances and damages on the Earth's surface. Especially in urban areas, it poses risk to life and property. Establishing solutions for damage prevention requires knowledge of subsidence behavior over time and space, which entails the collection of geospatial information. The present work investigates the ground surface dynamics over a field of deep mining in Sondershausen, Germany based on multi-temporal Synthetic Aperture Radar (SAR) images. Deformation patterns are extracted by means of Persistent Scatterer Interferometry (PSI), a technique that exploits the spatio-temporal characteristics of interferometric signatures from persistent scatterers. Since the impact of subsidence on surface structures varies spatially, high-risk areas can only be identified when the subsidence profile is known. To model the geometry of the subsidence bowl, the present study extends the extracted point information to a surface of estimations by interpolation. Furthermore, by the synergistic usage of PS estimations from different satellite sensors, this research addresses the problem of undersampling in critical areas, which is a common limitation of the PSI approach. The methodology developed here estimates missing information, i.e. refines the initial model, by deformation map of a different sensor covering a different time interval.

In order to extend the period of monitoring as well as to improve the spatial and temporal sampling, the ground subsidence in Sondershausen is monitored with a multi-sensor SAR dataset. The C- and L-band acquisitions of the sensors ERS-1/2 (1995–2005), Envisat-ASAR (2004–2010) and ALOS-PALSAR (2007–2010) are used to derive 15 years of subsidence information at the location of persistent scatterers. From a temporal viewpoint, the obtained deformation maps indicate a non-linearly decreasing trend of ground subsidence, which is consistent with the backfilling history of the mine. From a spatial viewpoint, the results suggest one major subsidence trough located in the urban area of Sondershausen and a minor one found in the nearby village of Großfurra. The PSI deformation maps and models are validated in reference to the available leveling measurements covering the site in Sondershausen. In general, the validation results suggest a good agreement between the PSI and surveying models with the normalized root-mean-square error (RMSE) lower than 0.11. However, some significant deviations of ERS estimations are also found for a critical region. In this area the absence of persistent scatterers contributes largely to the observed differences. Consequently, the spatial refinement by synergy is

applied to this region. The integration of points from ASAR or PALSAR deformation maps result in an improvement in the modeled geometry of the subsidence trough. With this improvement the RMSE calculated for the ERS model is decreased from 0.061 to 0.054. The application demonstrates the synergistic potential of multi-sensor PSI analysis to improve the interpretation of ground subsidence characteristics and, thus, to increase the confidence of risk assessment.

# Zusammenfassung

Absenkungen des Bodens stellen ein häufig auftretendes Phänomen dar. Diese Bodensenkungen verursachen Störungen und Schäden an der Erdoberfläche, die, insbesondere in urbanen Gebieten, Menschenleben gefährden und die bestehende Infrastruktur beschädigen können. Die Entwicklung von Lösungsansätzen zur Vermeidung von Schäden erfordert fundierte Kenntnisse über die räumliche und zeitliche Verteilung der Absenkungsbewegungen. Im Rahmen der vorliegenden Studie wurde die Dynamik der Bodenbewegungen über dem Salzabbaugebiet Sondershausen in Deutschland mittels Zeitserien von Synthetic Aperture Radar (SAR)-Aufnahmen untersucht. Zur Analyse der Zeitserien wurde das Verfahren der Persistent Scatterer Interferometry (PSI) eingesetzt. Diese Methode zur Extraktion der Bodendeformation basiert auf der Auswertung räumlicher und zeitlicher Charakteristika der interferometrischen Signaturen zeitlich stabiler Punktstreuer. Zur Bestimmung von Gebieten, die von den Bodensenkungen besonders stark betroffen sind, ist eine detailliertere Ermittlung der geometrischen Eigenschaften der Absenkung nötig, da die Oberflächenstrukturen entlang des Absenkungsprofils variieren. Aufgrund dessen wurde in der vorliegenden Studie die punktweise gewonnene Information in die Fläche extrapoliert, um eine räumliche Modellierung des Absenkungsbeckens zu ermöglichen. Zur genauen Vermessung von Absenkungen mittels PSI ist eine möglichst hohe räumliche und zeitliche Abtastrate anzustreben. Diese sind bei der Untersuchung eines Gebietes mithilfe eines einzelnen Radarsensors häufig nicht gewährleistet. Im Rahmen der vorliegenden Arbeit wird ein Lösungsansatz für diese Limitation vorgestellt, welcher auf der synergetischen Verschneidung von Deformationskarten mehrerer Radarsensoren basiert. Fehlende Messwerte in der ERS-Zeitreihe werden anhand von Punktstreuern in ASAR- und PALSAR-Szenen geschätzt.

Die Bodenbewegungen im Gebiet Sondershausen wurden mithilfe von Daten verschiedener Radarsensoren beobachtet, um eine verbesserte räumliche und zeitliche Abtastrate zu erzielen. Hierzu wurden Aufnahmen der C- bzw. L-Band Sensoren ERS-1/2 (1995–2005), Envisat-ASAR (2004–2010) und ALOS-PALSAR (2007–2010) auf zeitlich stabile Punktstreuer untersucht. Die zeitliche Analyse der resultierenden Deformationskarten zeigen eine nicht-lineare Abnahme der Bodenabsenkungen. Dieses Verhalten steht im Einklang mit den rezenten Verfüllungsaktivitäten in der stillgelegten Mine. Die räumliche Auswertung der Daten deutet auf ein Absenkungsbecken im Stadtgebiet von Sonder-

shausen hin. Ein weiteres, kleineres Becken konnte um die Siedlung Großfurra identifiziert werden. Sowohl die Deformationskarten als auch die abgeleiteten Modelle wurden einer umfangreichen Validierung anhand von Nivellement-Messungen unterzogen. Die Ergebnisse zeigen generell eine gute Übereinstimmung zwischen den PSI- und Bodenmessungen mit einem root-mean-square error (RMSE) von weniger als 0,11. Nur vereinzelt kommt es zu signifikanten Abweichungen, was insbesondere auf die ERS-Ergebnisse zutrifft. Dies lässt sich durch fehlende Punktstreuer in den aktiven Absenkungsbereichen während der ERS-Messungen begründen. Durch die Integration von Punkten aus den ASAR- oder PALSAR-basierenden Deformationskarten konnte die Geometrie der Absenkungen verbessert werden. Der für das ERS-Modell ermittelte RMSE verringert sich auf diese Weise von 0,061 auf 0,054. Die vorliegende Anwendung zeigt das Synergiepotential multisensoraler Daten und Methoden verbesserten Interpretation von Bodenabsenkungen sowie zur genaueren Abschätzung und Bewertung von daraus resultierenden Risiken.

# Contents

<b>Acknowledgments</b>	<b>vii</b>
<b>Abstract</b>	<b>ix</b>
<b>Zusammenfassung</b>	<b>xi</b>
<b>List of Figures</b>	<b>xvii</b>
<b>List of Tables</b>	<b>xix</b>
<b>Acronyms</b>	<b>xxi</b>
<b>1 Introduction</b>	<b>1</b>
1.1 Research context . . . . .	1
1.2 Thesis outline . . . . .	3
<b>2 Background and State Of the Art</b>	<b>5</b>
2.1 Ground subsidence monitoring and modeling . . . . .	5
2.1.1 Ground subsidence induced by underground mining . . . . .	6
2.1.1.1 Factors influencing mine subsidence . . . . .	6
2.1.1.2 Subsidence parameters . . . . .	7
2.1.1.3 Impact of subsidence on the surface . . . . .	9
2.1.2 Monitoring ground subsidence by radar remote sensing . . . . .	9
2.1.2.1 Radar imaging and SAR systems . . . . .	10
2.1.2.2 SAR interferometry . . . . .	12
2.1.2.3 Differential SAR interferometry . . . . .	14
2.1.2.4 DInSAR limitations . . . . .	15
2.1.2.5 Persistent scatterer interferometry . . . . .	19
2.1.3 Modeling ground subsidence by radar remote sensing observations	22
2.2 State of the art . . . . .	23
<b>3 Research Needs and Study Objectives</b>	<b>29</b>

<b>4</b>	<b>Research Site and Dataset Characteristics</b>	<b>31</b>
4.1	Glückauf potash mine field in Sondershausen . . . . .	31
4.1.1	Geological setting of the area . . . . .	31
4.1.2	The Glückauf mine . . . . .	32
4.2	Dataset . . . . .	33
4.2.1	SAR image datasets . . . . .	33
4.2.1.1	The ERS stack . . . . .	34
4.2.1.2	The ASAR stack . . . . .	35
4.2.1.3	The PALSAR stack . . . . .	35
4.2.2	Supplementary datasets . . . . .	36
<b>5</b>	<b>Methodology</b>	<b>37</b>
5.1	Supplementary data processing . . . . .	37
5.1.1	Weather data processing . . . . .	38
5.1.2	Surveying data processing . . . . .	40
5.2	Monitoring . . . . .	42
5.2.1	PSI analysis of SAR data . . . . .	42
5.2.1.1	Pre-Processing . . . . .	42
5.2.1.2	Master scene selection . . . . .	43
5.2.1.3	Coregistration . . . . .	46
5.2.1.4	PSI processing . . . . .	46
5.2.2	Post-Processing . . . . .	49
5.2.2.1	Removal of outliers and isolated points . . . . .	49
5.2.2.2	Derivation of vertical displacement rates . . . . .	51
5.2.3	Validation strategies . . . . .	52
5.2.3.1	Pointwise comparison . . . . .	52
5.2.3.2	Surfacewise comparison . . . . .	53
5.3	Modeling . . . . .	54
5.3.1	Generation of geometric models from PSI estimations . . . . .	55
5.3.2	Model refinement: synergy of PSI estimations . . . . .	56
<b>6</b>	<b>Results</b>	<b>59</b>
6.1	The PSI deformation maps . . . . .	59
6.2	Validation of the PSI deformation maps . . . . .	62
6.2.1	Pointwise validation . . . . .	62
6.2.2	Surfacewise validation . . . . .	65
6.3	The geometric models . . . . .	67
6.4	The refined model . . . . .	70

<b>7 Discussion</b>	<b>77</b>
7.1 Remarks on the methodology . . . . .	77
7.1.1 Premises of the methodology . . . . .	78
7.1.2 Transferability of the synergistic modeling . . . . .	79
7.2 Interpretation of the study results . . . . .	80
<b>8 Conclusions and Outlook</b>	<b>83</b>
8.1 Summary and conclusions . . . . .	83
8.2 Future directions . . . . .	85
<b>Bibliography</b>	<b>87</b>
<b>A Complementary Figures</b>	<b>95</b>
<b>Selbständigkeitserklärung</b>	<b>103</b>





# List of Figures

2-1	Subsidence trough and subsidence parameters . . . . .	8
2-2	Imaging geometry of SAR systems . . . . .	12
2-3	Imaging geometry of SAR interferometry . . . . .	13
2-4	Distributed and persistent scatterer pixels . . . . .	20
2-5	A selection of PSI studies for ground subsidence monitoring . . . . .	27
4-1	Research site . . . . .	32
4-2	Baseline graphs . . . . .	34
5-1	Flow chart of the methodology . . . . .	38
5-2	Two examples of surveying points . . . . .	40
5-3	Surveying deformation maps . . . . .	41
5-4	Master scene selection strategy . . . . .	45
5-5	Topographic height values . . . . .	46
5-6	Principle of outlier removal . . . . .	49
5-7	PALSAR deformation maps before and after point removal . . . . .	50
5-8	Principle of pointwise validation . . . . .	53
5-9	Principle of surfacewise validation . . . . .	54
5-10	Flow chart of modeling . . . . .	55
5-11	Principle of model refinement . . . . .	57
6-1	PSI deformation maps . . . . .	61
6-2	Pointwise validation of the PSI results . . . . .	64
6-3	Surfacewise validation of the PSI results . . . . .	66
6-4	The geometric models . . . . .	69
6-5	Refined deformation maps and models of ERS . . . . .	71
6-6	Validation of the refinement by ASAR . . . . .	74
6-7	Validation of the refinement by PALSAR . . . . .	75
A-1	Geological columnar section at the research site . . . . .	96
A-2	Weather parameter maps . . . . .	97
A-3	Histograms for LOS and vertical deformation rates . . . . .	98
A-4	Variograms of PS and surveying surfaces . . . . .	99
A-5	Maps of PS and surveying points . . . . .	100

*List of Figures*

A-6 Results of ERS-ASAR integration for three clusters . . . . .	101
A-7 Results of ERS-PALSAR integration for three clusters . . . . .	102

# List of Tables

4-1	Acquisition parameters of the SAR datasets . . . . .	33
6-1	Summary of the validation of the PSI deformation maps . . . . .	67
6-2	Summary of the validation of the PSI models . . . . .	72
7-1	Validation measures for some selected PSI studies . . . . .	81



# Acronyms

**ALOS** Advanced Land Observing Satellite

**ASAR** Advanced Synthetic Aperture Radar

**DEM** Digital Elevation Model

**DEOS** Department of Earth Observation and Space Systems

**DInSAR** Differential SAR Interferometry

**DLR** Deutsches Zentrum fuer Luft- und Raumfahrt (German Aerospace Center)

**DWD** Deutscher Wetterdienst (German Meteorological Service)

**ENVISAT** Environmental Satellite

**ERS** European Remote Sensing Satellite

**ESA** European Space Agency

**FBD** Fine Beam Dual Polarization

**FBS** Fine Beam Single Polarization

**Geohazard** Geological Hazard

**GPS** Global Positioning System

**GSES** Glueckauf Sondershausen Entwicklungs und Sicherungsgesellschaft mbH

**GVV** Gesellschaft zur Verwahrung und Verwertung von stillgelegten Bergwerksbetrieben  
mbH

**INFLUINS** Integrated Fluid Dynamics in Sedimentary Basins

**InSAR** SAR Interferometry

**IPTA** Interferometric Point Target Analysis

**JAXA** Japan Aerospace and Exploration Agency

*List of Tables*

**LOS** Line Of Sight

**MLI** Multi Look Image

**PALSAR** Phased Array L-band Synthetic Aperture Radar

**PS** Persistent Scatterer

**PSI** Persistent Scatterer Interferometry

**RAR** Real Aperture Radar

**RMSE** Root-Mean-Square Error

**SAR** Synthetic Aperture Radar

**SLC** Single Look Complex

**SBAS** Small Baseline Subset

**StaMPS** Stanford Method for Persistent Scatterers

**STUN** Spatio-Temporal Unwrapping Network

**TLUG** Thueringer Landesanstalt fuer Umwelt und Geologie (Thuringian Authority of Environment and Geology)

# Chapter 1

## Introduction

### 1.1 Research context

Ground subsidence, originated from human activity including mining and groundwater withdrawal or occurring naturally due to, for example, volcanic activities or earthquakes, is a phenomenon that occurs prevalently on the surface of the Earth. It is a geological hazard (geohazard) which has the potential to pose risk to life and surface structures, as well as to damage the environment. Consequently, the assessment of the risk is an important objective in land-use planning and providing appropriate engineering design for the surface structures [BELL 2002].

In order to assess the risk and reduce the impact of subsidence, the behavior of the phenomenon needs to be understood [BELL 2002]. For describing the behavior, collection of deformation information is required. Conventional ground-based measurements by leveling or Global Positioning Systems (GPS) are well established and frequently applied techniques for the collection of subsidence information. However, monitoring of large areas with dense networks and frequent time intervals is expensive and time-consuming. In contrast, spaceborne radar remote sensing is capable of providing precise measurements of deformation over a large area with moderate to low cost. Furthermore, this technique provides the option for retrieving deformation information by the SAR images acquired in the past [HOOPER et al. 2012], [SAMSONOV et al. 2014].

With the development of the interferometric SAR technique, the displacement occurring in the line-of-sight of the radar can be estimated by interfering two or more SAR images [MASSONNET and FEIGL 1998]. However, changes in imaging geometry and surface scattering properties from one image to another limit the applicability of this method. Furthermore, even if the measurement is possible, the deformation signal is affected by variations in the atmosphere and errors in satellite orbit information. These limitations challenge in particular the detection of slow deformation processes by standard SAR interferometry [HOOPER et al. 2012].

To overcome these shortcomings, techniques for processing multiple acquisitions are

developed by the end of 1990s. One approach of time series analysis involves identifying “persistent scatterers” pixels, whose scattering properties remain stable throughout the monitoring period. Temporal stability of scattering properties enables the computation of reliable deformation estimations in millimeter scale, since the atmospheric contributions as well as the orbit and DEM errors can be estimated and removed [FERRETTI et al. 2001].

Persistent scatterer interferometry is a widely used technique to obtain deformation estimations and is regarded as a powerful tool contributing to the studies dedicated to the initial assessment of the risks posed by the deformation. In this regard, this research utilizes the PSI technique for retrieving the temporal and spatial characteristics of the investigated ground subsidence.

The present work is conducted in the framework of the multi-disciplinary project INFLUINS, whose major objective is to examine the movements and the interactions between shallow and deep fluids in the Thuringian Basin in Germany. To achieve its goals, INFLUINS links diverse fields spanning geology, hydrogeology, mineralogy, geochemistry, geophysics, climatology and remote sensing in an innovative research focus. In INFLUINS the remote sensing data is used to study ground movements occurring in Thuringian Basin, with the main objective of deriving the groundwater related surface dynamics. Additionally, the parts of the basin affected by ground displacements due to subsidence or mining are investigated for the purpose of retrieving general information on surface dynamics, i.e. gaining knowledge on the active processes taking place in the basin. In this regard, the research documented in this thesis addresses the derivation of mining induced subsidence characteristics in Sondershausen by remote sensing techniques.

Ground subsidence affecting the town of Sondershausen in the form of a subsidence trough is induced by the intensive mining activities from 1898 to 1991. During this period, the rate of subsidence has increased gradually reaching to a critical deformation rate accompanied by seismic events [FLISS et al. 2011]. After the termination of salt extraction in 1991, the corresponding part of the mine is backfilled, as a consequence, the subsidence rates are gradually decreasing.

In spite of decreasing subsidence rates in Sondershausen, the demand for monitoring of the subsidence still exists, both for assessing the risk and verifying the effect of backfilling. Furthermore, regular collection of deformation information is required in Germany by the mining authorities [WALTER et al. 2009]. For this reason, the present work investigates the potentials of PSI technique for monitoring the ground subsidence in Sondershausen as an alternative or a complimentary method to the ground measurements.

The effect of subsidence on the surface structures depends on the component of the displacement, which varies along the subsidence profile. In other words, different components of subsidence affect different structures in different ways [BELL 2002]. For instance, the vertical subsidence may seriously damage the drainage system, whereas tilt may



seriously affect tall chimneys or railroads. However, the most damage is generally caused by differential horizontal movements [BELL 2002]. Since the influence of these movements depends on the subsidence profile, it is beneficial to determine the geometry of the subsidence for initial identification of the areas with highest risk. Therefore, this research deals with geometrical modeling of the subsidence by the rates measured at persistent scatterers.

Considering the long history of subsidence in Sondershausen, multiple sets of SAR data from different sensors are utilized. The combination of information from different sources offers promising perspectives for subsidence monitoring. In particular, an extension of the monitoring period and the availability of various spatial resolutions and sensibilities to displacements will allow for a retrieval of more detailed information on the characteristics of the subsidence. For this reason, this research exploits the SAR images of ERS-1/2 (C-band, 1995–2005), Envisat-ASAR (C-band, 2004–2010) and ALOS-PALSAR (L-band, 2007–2010) for 15 years of monitoring of subsidence in Sondershausen.

Promoted by the upcoming SAR data acquisitions from various missions, the need for development of new methodologies to explore the synergy between multi-sensor data grows. Motivated by this growth, the present work proposes a novel methodology for the synergistic usage of the observations from multiple sensors to tackle the common problems of spatial gaps at critical areas in the single sensor PSI results. The approach estimates missing information by deformation map of a different sensor covering a different time span. Thereby, the initially generated geometric model of the subsidence trough is improved.

## 1.2 Thesis outline

The thesis documenting the present study is structured upon the steps of

- introducing the general concept of the investigated phenomenon and the tool to observe it. For this purpose, the background section of Chapter 2 describes the fundamentals of the relevant ground subsidence with its characteristic effects on the surface. Furthermore, an effective tool of Earth observation for monitoring the motion, i.e. persistent scatterer interferometry, and its characteristics are also introduced in this chapter. Following the background information, the state of the art of SAR interferometry in ground subsidence monitoring is described in the later stage of this chapter.
- summarizing the research needs and study objectives. Implications of the developments, described in the state of the art, on the present work are explained in the

## *Chapter 1 Introduction*

context of research needs. Based on the needs, the aims and objectives of the study are also formulated in Chapter 3.

- explaining the research site and dataset characteristics. The phenomenon occurring in the study area is observed by the available data. Consequently, the characteristics of both research site and dataset have implications on the processes of methodology developments and interpretations. Therefore, a brief description of such characteristics is provided in Chapter 4.
- introducing the methodologies utilized to meet the research objectives. The operations including extraction of the information about the phenomenon, validation of the processing results, as well as generation of geometrical models and refinement of an initial model by synergy are described in Chapter 5.
- analyzing the results based on the research objectives. The products of the operations including PSI deformation maps, validation maps and surfaces modeling the subsidence rates are examined and interpreted with regard to the objectives of the study. Thereby, the results and their implications are presented in Chapter 6.
- discussing the implications of the results with regard to the methodology and outcome. The related considerations are provided in Chapter 7.
- drawing conclusions in the framework of the present study and providing an outlook. This part of the documentation, presented in Chapter 8, includes the summary of the context of the thesis, the conclusions relevant to the research objectives and the directions for possible future research.

# Chapter 2

## Background and State Of the Art

This chapter provides a background on the basic aspects of the investigated ground subsidence type and deformation mapping by means of radar remote sensing. Furthermore, the current state of the developments in this field is described. For this purpose, Section 2.1 is dedicated to the general definition and basic characteristics of mining induced ground subsidence and its impact on the surface, furthermore, to the fundamentals of subsidence monitoring and modeling by persistent scatterer interferometry. Section 2.2 presents the state of the art of SAR interferometry in ground subsidence monitoring.

### 2.1 Ground subsidence monitoring and modeling

Ground subsidence can be defined as rapid or gradual sinking of the ground surface with respect to the surrounding terrain or sea level. Natural causes such as earthquakes and volcanoes, as well as anthropogenic causes like withdrawal of groundwater, exploitation of oil and gas, extraction of coal and ores, and excavation of tunnels can result in ground subsidence.

Particularly in densely populated areas, ground subsidence can be responsible for significant damages to houses and urban infrastructure, thereby presenting risk to life. Aiming at reducing the impact of subsidence, the risk should be appropriately estimated with the collection of deformation information by monitoring. Furthermore, the acquired information can be used to model the subsidence geometry so that the mitigation of the risk can be addressed by providing related solutions.

In this study, ground subsidence due to underground mining is addressed. In this regard, this section describes the general characteristics of the ground subsidence induced by mining activities. Following the description of the phenomenon, the technique utilized in the present work, i.e. spaceborne radar remote sensing, for monitoring the ground subsidence is briefly explained. Finally, the employed strategy for modeling based on the estimations obtained by radar remote sensing is introduced.

### **2.1.1 Ground subsidence induced by underground mining**

Mining subsidence is described as the sinking or collapse of the Earth's surface caused by underground mining activity [GE et al. 2007]. During or long after mining, the rocks above the mine working may settle into the carved area because of the overburden pressure of the top and side rock mass layers. Settlements of the roof above the mine opening may vary in magnitude from lowering to complete collapse. The subsidence of the roof strata usually results in movements at the Earth's surface.

The surface above mine workings commonly subsides in the form of a subsidence trough [NSW 2008]. Troughs occur from sagging of overburden into soft rock at the mine floor or the mine roof due to failure of the mine pillars or the punching of the pillars into soft rock. As sketched in Figure 2-1, the resultant form at the surface is a shallow but broad depression, which is usually in circular or elliptical shape [GE et al. 2004], [DUNRUD and OSTERWALD 1980].

#### **2.1.1.1 Factors influencing mine subsidence**

The magnitude, extent as well as timing and duration of subsidence depend on different factors of geological and mining settings [BLM 2009], [BAUER 2008].

Geological factors controlling subsidence characteristics include the structure, lithology, strength of the overlying and underlying strata, topography and fault orientations. Massive, strong strata in the overburden is capable of sagging without failing [NSW 2008], whereas soft overburden tends to fail, suggesting that the characteristics of the strata has an impact on the magnitude and extent of the subsidence. Heavy overburden in the areas of steep topography can result in higher amounts of ground movement than the areas with less overburden. Faults control the transmission of stresses within the rock mass in a way that they can change the stress concentration and directionality. As a result, the spanning and caving behavior of undermined strata will be changed [NSW 2008].

Mining settings shaping the subsidence trough refer to depth, geometry, method and rate of mining. The height and width of the mining opening with respect to the depth of the mining and thickness of the overburden control the maximum subsidence [BLM 2009]. The shape of the subsidence basin gets shallower and wider as the depth of the mine opening increases [KRATZSCH 1997] in [WALTER et al. 2004]. An example of the influence of mining depth is reported in the work of DUNRUD and OSTERWALD [1980] that in the areas with less than 15 m thick overburden in the Sheridan, Wyoming mine field, the depressions are usually square or rectangular. In overburden thicker than this value the corners of the depression become rounded resulting in more circular or elliptical shape. Similarly, the thickness and width of the excavations has a direct impact on the depth of the subsidence trough because as the excavation becomes wider, the sag of the overlying

## 2.1 Ground subsidence monitoring and modeling

strata increases and hence the subsidence trough gets deeper [NSW 2008].

Underground mining methods are generally classified by the type of support used to carry the roof and the overburden. For instance, in room-and-pillar mining, the roof is supported primarily by pillars, which are the parts left between excavated areas and arranged in a regular pattern whereas in longwall mining a long wall of material is extracted [BLM 2009]. The mine geometry determines the configuration of the excavated areas and the supports. For the room-and-pillar method this implies the arrangement of rooms and pillars, including size, shape and distribution, and for longwall it refers to, for example, height and width of the excavation [BLM 2009].

The method of mining influences the extraction amount in a way that in longwall mines the amount is usually higher than room-and-pillar mines, similarly it also affects the degree of subsidence. Longwall mining usually results in more subsidence, partly because of a larger extraction, but the effect is more uniform and anticipated. Room-and-pillar operations, on the other hand, are less predictable in the amount and surface form of the subsidence due to varying room and pillar designs [BAUER 2008].

The characteristics of the subsidence are also influenced by the rate of mining. Even and rapid extractions yield to a smooth subsidence profile whereas more differential motion occurs with an uneven rate [BLM 2009].

### 2.1.1.2 Subsidence parameters

Although subsidence usually refers to the vertical displacement, the actual movement of the ground surface also includes tilt, horizontal displacement, curvature and strain. These components of subsidence are the main causes of surface damage due to mining induced ground displacements, consequently, the estimation of these parameters generally forms the basis of the assessment of the surface effects and their impact on the infrastructure [MSE 2007].

The maximum of the vertical movement, marked by  $S_{max}$  in Figure 2–1, occurs in the center of the subsidence trough for a symmetrical basin. The amplitude of subsidence, the vertical displacement, is given in units of length (millimeter) [MSE 2007].

Tilt is the first derivative of the subsidence profile and it is calculated by the change in rate between two points. Tilt reaches its maximum at the steepest portion of the subsidence profile which occurs at the inflection point, where the curvature changes from convex to concave (green curve in Figure 2–1). It is usually given in length over length (millimeter/meter) [NSW 2008], [PUERTAS 2010].

The horizontal component of the subsidence reaches its maximum at the inflection point, where the tilt is maximum. From the inflection point to the limit and to the point of maximum subsidence, the horizontal displacement declines to zero (orange curve in

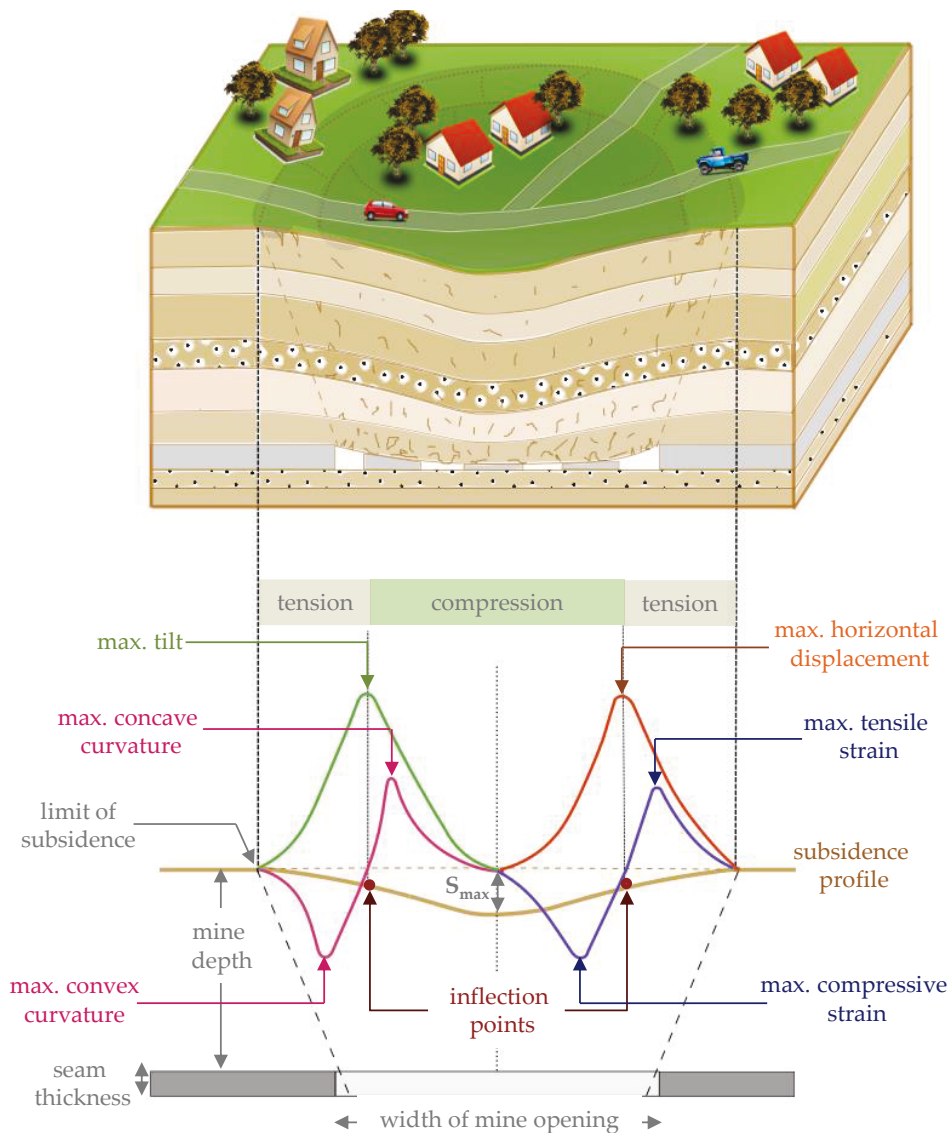


**Figure 2-1:** The upper plot sketches a subsidence trough occurring above an underground mine. The lower plot is a graphical representation of the behavior of subsidence components in flat topography (drawn based on NSW [2008]). The behavior of individual components are depicted only for the half of the subsidence profile.  $S_{max}$  stands for the maximum subsidence.

Figure 2-1). It is usually expressed in units of length (millimeter) [MSE 2007].

The rate of change of tilt, i.e. the second derivative, gives the curvature. From the inflection point to the edge of subsidence trough the curvature is convex, whereas to the bottom of the trough it is concave (magenta curve in Figure 2-1). The unit for curvature is in 1 over length (usually in  $\text{km}^{-1}$ ) [NSW 2008], [MSE 2007].

The amount of horizontal extension or compression on the surface is expressed as strain

## 2.1 Ground subsidence monitoring and modeling

[NSW 2008]. It is derived from the first derivative of horizontal displacement and caused by bending and differential horizontal movements. The maximum strain coincide with the maximum curvature. Towards to the sides of the panel maximum tensile strain occurs whereas the maximum compressive strain happens towards the bottom of the subsidence trough (indigo curve in Figure 2–1). The unit of strain measurement is length over length (millimeter/meter) [MSE 2007].

### 2.1.1.3 Impact of subsidence on the surface

The individual components of subsidence have different effects on surface structures, furthermore, the impact differs depending on the type of structure [WHITTAKER and REDDISH 1989], [BELL 2002]. For example, in general terms the vertical subsidence does not affect the surface structures since it represents a rigid body movement [MSB 2007], however, it is a major aspect in the low lying areas prone to flooding and in the areas with drainage problem [WHITTAKER and REDDISH 1989], [BELL 2002].

Tilt damage is also small, however, it can be of importance to tall buildings, drainage schemes, sewerage networks, highways and rail tracks [WHITTAKER and REDDISH 1989], [BELL 2002]. Horizontal movements in the subsidence trough are overall small and do not cause strong structural damage [MSB 2007].

In general, the differential horizontal movements (strain) and the differential settlement across the surface (curvature) mostly damage the surface structures [MSB 2007], [WHITTAKER and REDDISH 1989]. Furthermore, most buildings experience stronger damage in the tensile strain than compressional, since the building material is usually weaker in tension. In practice, the major damage of subsidence is a result of combination of both strain and curvature [MSB 2007].

Due to the differing impact of the subsidence parameters, reducing the risk of subsidence damage and compensating for the effects on surface structures require design considerations based on the surface movements. Therefore, it is important to determine the trend of different parameters.

### 2.1.2 Monitoring ground subsidence by radar remote sensing

In order to provide a better knowledge of ground subsidence phenomena, and hence, an effective risk management, monitoring techniques by means of data collection are required [RAUCOULES et al. 2007]. Beside risk management, the need for subsidence monitoring includes legislative requirements, subsidence prediction, maximizing the amount of extraction, structural design and environmental monitoring [GE et al. 2004].

The crucial tasks of monitoring include the detection of spatial pattern and temporal evolution of the subsidence as well as an accurate assessment of the magnitude of the

displacements. Techniques based on ground benchmarks such as geodetic leveling and GPS generally provide precise measurements. However, they are limited to the accessibility of the area of interest and high costs of wide-area monitoring [RAUCOULES et al. 2007]. As a result, measurements are taken only at limited locations with low frequency. Furthermore, in case of sudden or unpredicted deformations, ground networks are implemented only after the deformation phenomena [COLESANTI et al. 2005].

Remote sensing techniques, where the observations of surface movements are taken from a certain distance, e.g. at satellite altitude, can be a complimentary method and in certain cases can replace the ground-based measurements [COLESANTI et al. 2005]. In particular with the recent advancements in radar imaging capabilities, e.g. high spatial resolution and frequency of acquisitions, as well as the development of new techniques based on interferometric analysis of radar images, the potential of radar remote sensing for ground subsidence monitoring has been increased [FERRETTI et al. 2005].

In this section, fundamental principles of radar remote sensing techniques for ground deformation monitoring, i.e. synthetic aperture radar interferometry, are explained briefly. Subsequently, the details of deformation mapping by means of persistent scatterer interferometry with its strengths and limitations are discussed.

### **2.1.2.1 Radar imaging and SAR systems**

#### **Radar imaging**

Radar refers to an active sensor system which emits electromagnetic pulses in the radio and microwave range and detects the reflections of these pulses from objects in its line-of-sight (LOS). Based upon the time delay between the transmission and reception of the pulse, the radar system determines the range to the detected object, as the pulse travels at speed of light. Like the distance of the object by the time delay of the backscatter, the physical quantities of the object such as size or surface roughness can be inferred by backscatter intensity [HANSSEN 2001].

Sharing the same principles, different forms of radar systems exist providing different types of information. One specific class of radar system is called imaging radar. Rather than the role of traditional radar, used for detecting the position and the speed of an object, a imaging radar aims to generate a two dimensional map of the electromagnetic scattering of a scene. Since radar imaging is an active remote sensing system, data can be acquired at day and night. Furthermore, due to the specific wavelength of radar (in the range 1 cm to 1 m), cloud cover can be penetrated [FERRETTI et al. 2007].

Unlike optical systems that obtain information as a function of look direction, a radar image principally acquires information as a function of distance from the object [WOODHOUSE 2006]. Since the information of look direction is missing, i.e. poor angular resolving



## 2.1 Ground subsidence monitoring and modeling

power, the echos from two objects with same distance to the instrument but on opposite sides of nadir can not be distinguished. Therefore, the strategy of constructing an image with radar differs from that of optical sensors [WOODHOUSE 2006].

First part of the approach for radar imaging is to exploit the radar's distance detection abilities to compensate for the poor angular resolving power. This is achieved by pointing the radar sideways [WOODHOUSE 2006] rather than orthogonal to the surface like the optical systems. The second part of the approach is to use the motion of the instrument to scan the ground along the flight path to construct 2D radar images subsequently.

Radar imaging was originally developed in the 1950s, leading to first airborne system called Real Aperture Radar (RAR). However, the resolution of a radar image depends on the length of the antenna such that the longer the antenna, the better the resolution [FERRETTI et al. 2007]. For this reason achieving a reasonable along-track (azimuth) resolution at spacecraft altitudes with RAR requires very long antennas. An approach to compensate for this requirement is Synthetic Aperture Radar (SAR). Rather than depending on the resolution determined by the actual antenna as in the case of real aperture systems, synthetic apertures depend upon signal processing to achieve much finer resolution in the along-track direction than that attainable with the real antenna. This way high resolutions at satellite altitude can be achieved. The details of SAR systems and imaging characteristics are explained in the following sections.

### **SAR systems**

The key factor that is utilized in SAR is to synthesize a much longer antenna by making use of forward motion of the spacecraft. Due to this motion, the objects are viewed multiple times. The echoes returning from objects which are in front, are Doppler shifted to higher frequencies and the ones behind are shifted to lower frequencies so that the echo can be located in the beam. Using this information, a fine resolution image is assembled from multiple echoes of the same object at different sensor positions [WOODHOUSE 2006]. The geometry of a SAR system is shown in Figure 2-2. On this representation, the key geometric variables are identified. On the side view, the synthetic aperture, used for enlarging the aperture by processing, is marked.

### **SAR images**

A digital SAR image, acquired by the geometry depicted in Figure 2-2, is composed of pixels, each of which are associated with an area of the Earth's surface. The fundamental dimensions of a SAR image are slant range and azimuth, in other words, every pixel has a time delay and a flight path distance dimension (see Figure 2-2). Each pixel represents the backscatter echo of all the scatterers within a resolution cell. The recorded response of the microwave signal of a particular area on the ground gives a complex number that

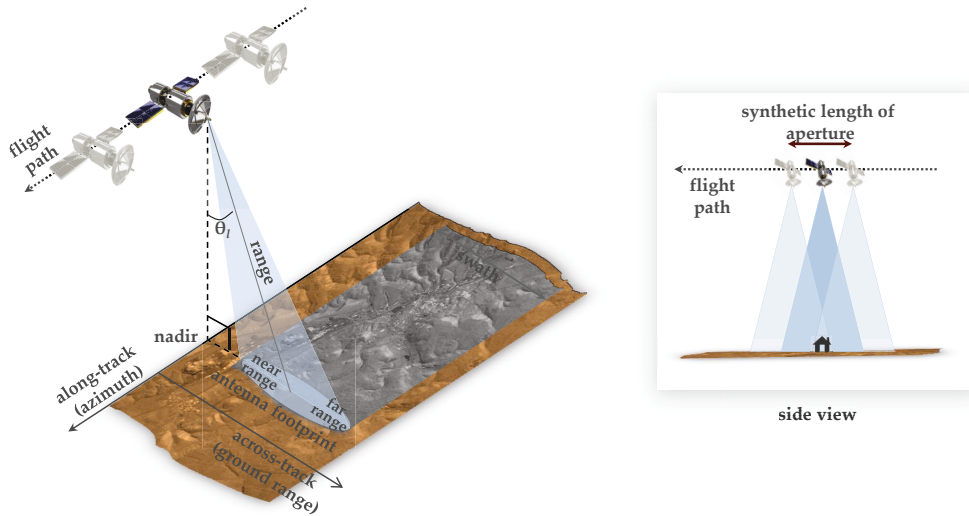


**Figure 2-2:** Imaging geometry of SAR systems. The antenna looks oblique to the ground with a look angle,  $\theta_l$ , scanning an area with width of swath while moving in azimuth direction. The multiple echos of an object recorded during satellite pass through synthetic aperture, marked on the side view, are used to assemble a high resolution image.

carries amplitude and phase information. The real part represents the amplitude being the backscatter intensity of the echo. The imaginary part of the complex number is the phase, which is the shift angle between the phase of the pulse sent and the echo, and relates to the object distance.

On one image the phase from one pixel to another looks random due to contributions from different scatterers in the resolution cell. On the other hand, range difference estimated by taking more images of the same area from different sensor positions cancels out the phase contribution introduced by individual scatterers. Furthermore, the relative path length can be geometrically related to the terrain height since the positions of the sensors are known. The technique exploiting the information supplied by such measurements is known as SAR interferometry.

### 2.1.2.2 Sensing of topography: SAR interferometry

The derivation of the information about relative distances from the spacecraft to the objects in a fraction of the sensor's wavelength by SAR interferometry (InSAR) allows determination of terrain heights, thereby, is used for topographical mapping. For interferometry, a second SAR image of the same area from a slightly different viewing angle is interfered with the first image. This interference is used to generate a SAR interferogram which is computed by pixel-by-pixel cross-multiplication of the first image by the complex conjugate

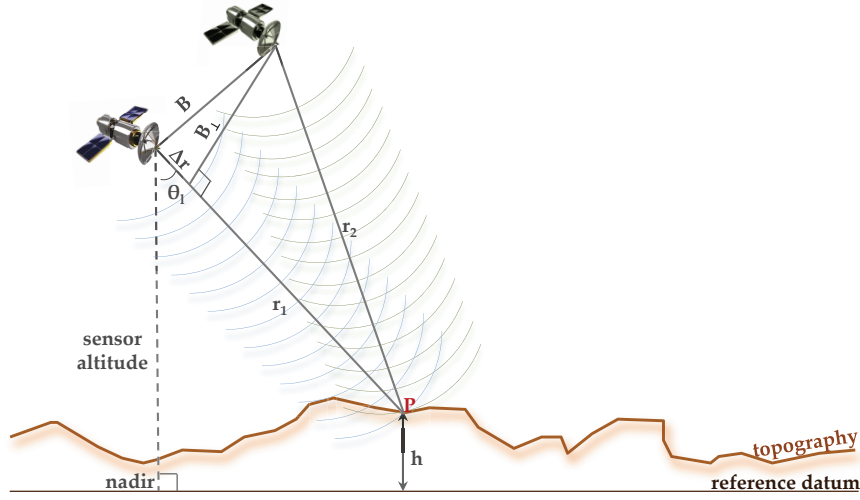


**Figure 2-3:** Imaging geometry of SAR interferometry. The flight paths of the sensors are perpendicular to the plane of the paper.  $r_1$  and  $r_2$  are the range of the sensors.  $\Delta r$  stands for the range difference between  $r_1$  and  $r_2$ .  $B$  is the baseline separation of the sensors with perpendicular component  $B_{\perp}$ .  $\theta_1$  represents the look angle, and  $h$  is the height of the target.

gate of the second one [HANSEN 2001]. Thus, the amplitude of the resulting interferogram is the amplitude of the first image multiplied by the second one, whereas its phase, the so-called interferometric phase, is the phase difference between two images [FERRETTI et al. 2007]. Equation 2.1 shows the complex conjugate multiplication of two SAR images.

$$S_1 * S_2^* = \rho_1 \rho_2 \cdot e^{i(\phi_1 - \phi_2)} \quad (2.1)$$

where  $S_1$  is the first image, and  $S_2^*$  is the complex conjugate of the second image,  $\rho_1$  and  $\rho_2$  are the amplitudes,  $\phi_1$  and  $\phi_2$  are the phase of the images. Ignoring the decorrelation effects and phase contributions from other sources, the difference in phase ( $\phi_1 - \phi_2$ ), i.e. interferometric phase, depends only on the change in path length. If  $\Delta\phi$  is the interferometric phase,  $\lambda$  is the transmitted wavelength and  $\Delta r$  is the range difference then,

$$\Delta\phi_i = \frac{4\pi}{\lambda} \Delta r \quad (2.2)$$

If there is no deformation, the range difference  $\Delta r$  depends only on the geometry depicted in Figure 2-3. The interferometric phase then can be written as,

$$\Delta\phi_i \approx \frac{4\pi}{\lambda} \frac{B_{\perp} \Delta h}{\sin\theta_1} \quad (2.3)$$

where  $B_{\perp}$  is the perpendicular baseline,  $\theta_1$  is look angle and  $\Delta h$  is the topographic height

difference. With this relation InSAR provides a means to estimate terrain topography. However, in addition to the topographic phase, the interferometric phase also includes a phase contribution due to Earth's curvature which causes a periodic fringe pattern on the interferograms in range direction. Therefore, Equation 2.3 is extended to

$$\begin{aligned}\Delta\phi_i &= \Delta\phi_{topo} + \Delta\phi_{flat} \\ &\approx \frac{4\pi B_{\perp}\Delta h}{\lambda r \sin\theta_l} + \frac{4\pi B_{\perp}\Delta r}{\lambda r \tan\theta_l}\end{aligned}\quad (2.4)$$

where  $\Delta\phi_{topo}$  denotes the interferometric phase caused by topography,  $\Delta\phi_{flat}$  is the so-called flat-earth phase. Since the aim of InSAR processing is to obtain topographic phase, the flat-earth term is computed by the perpendicular baseline from precise orbit data and an elliptical or spherical model for the Earth's surface and subtracted from the interferometric phase.

However, the flattened interferogram provides an ambiguous measurement of the relative terrain altitude because the interferometric phase is wrapped, i.e. it can only be measured as modulo  $2\pi$ ,

$$\phi = \phi_{InSAR} + N * 2\pi \quad (2.5)$$

where N is the ambiguous number of cycles. In order to compute the absolute phase differences ( $\phi$ ), i.e. terrain heights, the interferogram fringes have to be unwrapped. The phase unwrapping algorithms try to estimate the ambiguity number N for each pixel, and add this integer number to the interferometric fringes to estimate the terrain heights as shown in Equation 2.5.

### 2.1.2.3 Sensing of displacement: differential SAR interferometry

Some of the point scatterers might change their relative position between two SAR acquisitions due to, for example, a landslide, subsidence or an earthquake. This change in path length introduces an additive phase term in the interferometric phase equation, which is independent of the baseline [FERRETTI et al. 2007] (the third term in Equation 2.6 where  $\Delta r_{def}$  stands for the relative scatterer displacement on LOS). This implies that the interferometric phase contains the phase contribution from topographic height, the flat-earth-effect and the displacement as shown by Equation 2.6.

$$\begin{aligned}\Delta\phi_i &= \Delta\phi_{topo} + \Delta\phi_{flat} + \Delta\phi_{def} \\ &\approx \frac{4\pi B_{\perp}\Delta h}{\lambda r \sin\theta_l} + \frac{4\pi B_{\perp}\Delta r}{\lambda r \tan\theta_l} + \frac{4\pi}{\lambda}\Delta r_{def}\end{aligned}\quad (2.6)$$

The topographical phase,  $\Delta\phi_{topo}$ , can be estimated by a DEM of the area and subtracted

from the interferometric phase. Similarly, with interferogram flattening, the second term,  $\Delta\phi_{flat}$ , can be removed, so that the amount of displacement can be measured. This procedure of deriving surface movements is called Differential SAR Interferometry (DInSAR). Since the differential phase does not depend on the perpendicular baseline but depends only on the wavelength and the amount of change (see Equation 2.6), the sensitivity of SAR interferometry to terrain motion is significantly higher than to the topography [ROSEN et al. 2000]. Thus, with this method it is possible to generate large scale deformation maps with centimeter to millimeter accuracy.

### 2.1.2.4 Decorrelations and limitations associated with DInSAR

Despite the advantages of DInSAR technique for surface deformation measurement, various limitations are also inherent. So far it is assumed that there is only one dominant scatterer in a pixel which is stable between two acquisitions. However, usually a pixel consists of many different scatterers each of which may change during this period, introducing phase noise. Furthermore, changing weather conditions cause different path delays in the signal. Those influences are not considered in Equation 2.6, however, additional phase terms stemming from decorrelation and noise factors should be included in the interferometric phase equation.

Change in backscatter properties with time decorrelates the measurements significantly, leading to loss of useful phase information. Furthermore, variations in target backscattering as a function of the incidence angle of the signal introduces decorrelation [PRATI et al. 2010]. The phase decorrelation effects due to such temporal and geometrical sources are described as the most limiting factors of differential SAR interferometry [PRATI et al. 2010].

Temporal decorrelation usually stems from change in the backscatter coefficient or dielectric characteristics between two acquisitions due to variations in the moisture content, changes in state of the vegetation in different seasons, vegetation growth or erosion. This implies that the decorrelation occurs when the backscatter differs from one image to another due to changes in the scatterer position as well as the scatterer characteristics [MASSONNET and FEIGL 1998]. The time difference between two acquisitions is known as the temporal baseline. The period of decorrelation, i.e. maximum temporal separation, can be months to years for arid regions but it can also be hours to days for vegetated surfaces and it depends on the characteristics of the ground surface as well as the wavelength of the sensor [MASSONNET and FEIGL 1998].

The change in position of scatterers with respect to each other between satellite passes is common for vegetated areas [HOOPER et al. 2007]. For instance, random movement of leaves implies a phase change in a pixel leading to temporal incoherence. Similarly, the dynamics of agricultural areas, considering ploughing, crop growth and harvesting cycle,

contribute to the incoherence between two acquisitions. Therefore, temporal decorrelation degrades the usage of differential SAR interferometry in vegetated areas significantly.

In addition to land cover types, such as vegetation or urban areas, the wavelength of the radar is also an important factor defining the degree of temporal decorrelation. For example, if the radar wavelength is larger than the plant components, e.g. leaves, branches and stems, the signal penetrates through the vegetation and is backscattered from the ground surface. In this case, the temporal decorrelation is less pronounced since there is less interaction with the dynamic scatterer components.

Geometrical decorrelation occurs with different viewing angles since the relative locations of the scatterers depend on the viewing position. Two sources of geometrical decorrelation can be addressed. The variation in baseline separation causes a variation in phase between the corresponding pixels of the image pair. This kind of geometrical decorrelation increases as the baseline separation between two acquisitions becomes larger, leading to a maximum baseline separation between two sensor locations, thus, it limits the amount of usable images for InSAR analysis [FERRETTI et al. 2001]. Interferogram generation is only possible for the baseline values below this critical value that depends on the radar wavelength, sensor-target distance, range resolution, incidence angle and topography.

The second source of geometrical decorrelation is known as the Doppler centroid decorrelation, which is equivalent to the baseline decorrelation in azimuth and it is caused by the changes in squint angle, the angle with which the sensor looks backward or forward. Since the satellite transmitting the radar signal is in motion, the return signal reflects a change in frequency relative to the transmitted signal, known as Doppler effect. Therefore, changes in squint angle, altitude or velocity of the satellite implies a variation in frequency shift along the LOS. The estimate of the center frequency in this spectrum is called Doppler centroid and the Doppler baseline corresponds to the Doppler centroid difference of two SAR image pairs in hertz (Hz). An increase in Doppler baseline results in decrease in the common bandwidth and hence, degradation of the correlation between the images [ROSICH et al. 2000]. Similar to baseline decorrelation, there is a critical Doppler baseline value, above which no common frequency in the bandwidth is found between two image pairs, therefore, a total decorrelation occurs [ROSICH et al. 2000]. Although the impact of geometrical decorrelation effects can be minimized by filtering, no interferometric information can be retrieved above the critical values. This limits the number of usable interferogram pairs, thereby, reduces the temporal resolution of the monitoring with SAR data.

Although radar waves can penetrate clouds, they are not entirely unaffected by them. Similarly, change in atmospheric conditions between the SAR image acquisitions can cause an increase or decrease in the measured path length. Phase shift due to atmosphere can be

## 2.1 Ground subsidence monitoring and modeling

homogenous (ionospheric path delay) or heterogeneous (tropospheric path delay) depending on the atmospheric layers. The ionospheric delay is caused by the variations in the total electron content, which depends on the time of day, geographical latitude, sun activity and radar wavelength. The tropospheric influence is characterized by heterogeneous phase shifts, which is related to the physical parameters, e.g. water content of the air, affecting the speed of the signal [FERRETTI et al. 2007].

As shown in Equation 2.6, the estimation of flat-earth-phase depends on the baseline between two acquisitions. The accurate determination of the baseline relies on the precise orbital information. Therefore, errors in the baseline estimation causes errors in the flat-earth-phase and introduce an additional phase component in the interferometric phase equation.

Similarly, any inaccuracies in the DEM used for the simulation of the topographical phase cause errors in the deformation measurement. Furthermore, there is also an additional phase term stemming from thermal noise caused by the radar system noise and from coregistration noise by inaccuracies in the coregistration of the images.

Considering all these decorrelation effects and error sources, the differential interferogram phase,  $\Delta\phi_i$ , can be written as a sum of five phase terms:

$$\Delta\phi_i = \Delta\phi_{def} + \Delta\phi_{atm} + \Delta\phi_{orb} + \Delta\phi_{DEM} + \Delta\phi_n \quad (2.7)$$

where  $\Delta\phi_{def}$  is the phase change due to deformation in LOS,  $\Delta\phi_{atm}$  is the phase difference due to differential atmospheric delay between two acquisitions,  $\Delta\phi_{orb}$  is the residual phase due to orbit inaccuracies,  $\Delta\phi_{DEM}$  stands for the residual DEM errors and baseline decorrelation, and  $\Delta\phi_n$  is the phase noise.

Additional limitations of differential SAR interferometry are related to spatial gradient of the deformation, image pixel limitations and surface characteristics [MASSONNET and FEIGL 1998]. The maximum detectable deformation gradient is one fringe per pixel or the dimensionless ratio of the pixel size to the wavelength [MASSONNET and FEIGL 1998], [ZHOU et al. 2009]. If the relative displacement between two neighboring pixels exceeds this limit, the displacement is not detectable by InSAR. The limiting value depends on the sensor since the phase difference in a wrapped interferogram is between 0 to  $2\pi$ , i.e. maximum phase difference between two neighboring pixels is  $2\pi$ , and this corresponds to one fringe,  $\lambda/2$ . For a C-band sensor with the wavelength of 5.6 cm and 10 meter pixel size the displacement can not exceed 2.8 cm for 10 meters, whereas for L-band sensor with wavelength of 23.62 cm the limit is 11.5 cm per pixel. This relation also translates to the maximum detectable deformation rate of one fringe per time difference between two acquisitions [ZHOU et al. 2009]. With the temporal baseline of  $N$  days, the deformation rate should not exceed the value  $\lambda/2N$  [ZHOU et al. 2009].

A further limit is related to the size of the pixel. Estimation of the phase change on a pixel is unfeasible since it can include unpredictable noise [MASSONNET and FEIGL 1998]. Therefore, successful interpretation depends on the agreement of several neighboring pixels, consequently, it is not possible to recognize a small scale (smaller than 10 pixel) displacement by conventional InSAR [MASSONNET and FEIGL 1998].

Surface characteristics, such as roughness, affect the sensitivity to baseline decorrelation. With increasing topographic relief the sensitivity also increases, therefore, rough topography in mountains areas can restrict the useability of an interferogram due to decorrelation [MASSONNET and FEIGL 1998].

### **Reducing the impact of decorrelation effects**

Although decorrelation effects and phase artifacts are restricting the useability of InSAR depending on surface characteristics, and weather conditions, their impact can be partially minimized by careful selection of the radar dataset.

In order to reduce the influence of atmospheric artifacts, the selection should consider the weather conditions at the time of acquisitions, i.e. the images with comparable weather conditions should be used for interferometry. Similarly, seasons can be taken into account to exclude high temporal decorrelation for instance in the growing season.

Considering the spatial gradient of the deformation, the selection of temporal baseline can also be optimized in order to eliminate the ambiguities stemming from the deformation gradient. In order to minimize the impact of temporal decorrelation, a careful selection of the wavelength, i.e. the sensor, is also important. The signal transmitted from a short wavelength sensor (X-band) interacts with the top of the tree canopies. On the other hand, the signal from C-band sensor partially penetrates the vegetation and is also scattered by leaves, stems and branches, whereas longer wavelengths (L-band) can penetrate the canopies so that the signal can be backscattered from the ground surface [BAMLER and HARTL 1998]. Consequently, the impact of vegetation on the temporal decorrelation can be minimized by using longer wavelength of L-band sensors [RAUCOULES et al. 2007], [MASSONNET and FEIGL 1998].

Also the incidence angle determines the scattering response of the radar signal. The range increases with incidence angle, hence in most cases the backscattered power decreases [BAMLER and HARTL 1998]. For interferometry, the incidence angle should be chosen to balance the lay-over and shadow areas [BAMLER and HARTL 1998].

Despite the possibility to reduce decorrelation effects and their impact by the best possible selection of datasets, limitations associated with DInSAR are still prominent in many cases. In order to address those limitations of conventional DInSAR, advanced DInSAR techniques based on time series analysis are developed [HOOPER et al. 2012]. The time series algorithms classified into two broad categories, being Small Baseline



## 2.1 Ground subsidence monitoring and modeling

Subset (SBAS) [BERARDINO et al. 2002] and Persistent Scatterer (PS) [FERRETTI et al. 2001] approaches.

The SBAS approach aims to minimize the baseline decorrelation and the inaccuracies in the DEM by employing only the appropriate combination of differential interferograms characterized by a small baseline separation.

The PS technique relies on the selection of pixels demonstrating stable behavior, i.e. least affected by decorrelation effects, and generates the interferograms with respect to a common master image. All combinations of interferograms between the master and every other image are employed regardless of the baseline values. However, only the coherent pixels (persistent scatterer pixels) are used for further analysis. In this study, the PS technique is utilized in order to estimate the deformation due to mining activity, therefore, the approach is explained in detail in the following section.

### 2.1.2.5 Persistent scatterer interferometry

Temporal and geometrical decorrelation often prevents conventional differential SAR interferometry from being an operational tool for deformation monitoring, moreover, atmospheric disturbances degrades the accuracy of estimations [FERRETTI et al. 2001]. Furthermore, the measurement of slow motion and derivation of its temporal evolution requires a time series analysis, i.e. an advanced interferometric processing [BERARDINO et al. 2002].

In order to address the problems caused by decorrelation and atmospheric delay, the technique of identification and exploitation of pixels that are coherent over long time intervals is introduced by FERRETTI et al. [2001]. With the development of the persistent scatterer interferometry technique the applicability of SAR interferometry has significantly extended [VAN LEIJEN et al. 2005].

The phase of a pixel is the coherent of sum all the individual backscatterers in the resolution cell on the ground. If these scatterers move with respect to each other from one acquisition to another, which is commonly the case for vegetation, the phase of the corresponding pixel will vary randomly [HOOPER et al. 2007] as depicted in Figure 2–4 for distributed targets. On the other hand, if the pixel is dominated by a stable scatterer, brighter than the others, the interference from background scatterers will be reduced, yielding in a stable phase measurement (as shown in Figure 2–4 for persistent scatterer pixel), and hence enabling the extraction of the underlying deformational signal [HOOPER et al. 2007], [FERRETTI et al. 2001]. Persistent scatterers are stable natural reflectors and physically associated with trunk of a tree or a large rock in vegetated areas [HOOPER et al. 2007], or found mostly on the urban structures like buildings, roads, train rails etc.

In PSI analysis, a time series of images is used to generate differential interferograms for

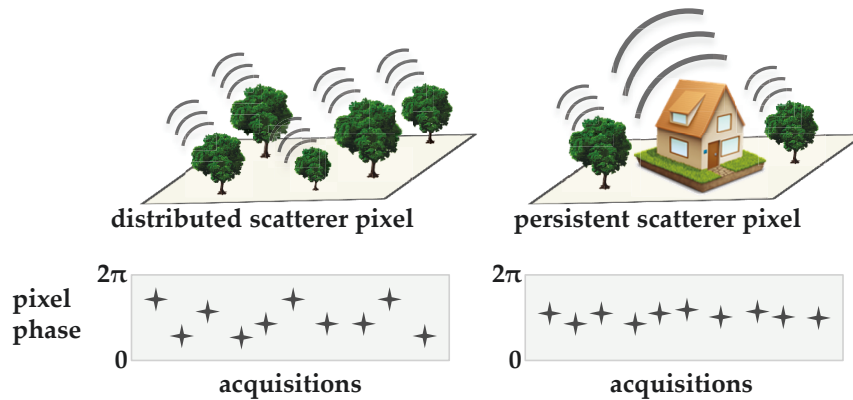


**Figure 2-4:** Sketch of scatterer mechanisms for distributed and persistent scatterer pixels. The upper drawings represent the scatterers contributing to the phase of a pixel, and the lower ones show the phase values for each acquisition. The persistent scatterer pixel exhibit more stable phase values, i.e. smaller phase variation, through the monitoring time compared to the distributed targets. The image is drawn based on HOOPER et al. [2012].

each available acquisition with respect to a common master, even if the pair is characterized by a baseline larger than the critical value [FERRETTI et al. 2001], [BERARDINO et al. 2002]. This has the advantage that all the available data can be successfully exploited for interferometric application [FERRETTI et al. 2001]. Since the PSI processing relies on the coherent pixels, the algorithm first searches for the pixels that stay stable for the entire stack of interferograms. Several methods are developed for the identification of persistent scatterers, e.g. FERRETTI et al. [2001], WERNER et al. [2003], KAMPES [2006], HOOPER et al. [2007]. The procedures for selection of initial PS pixels usually follows a statistical analysis in which the pixels with high signal-to-noise ratio are identified by analyzing the amplitude variation pixel-by-pixel throughout the interferogram stack. Furthermore, the phase stability of the pixel is examined with regard to the neighboring pixels and included in the selection criteria [PRATI et al. 2010], [FERRETTI et al. 2001].

The different phase terms from atmosphere, topography and displacement in Equation 2.7 can be isolated by exploiting their different behavior in spatial and temporal dimension [PRATI et al. 2010], [WERNER et al. 2003]. For instance, the linear component of displacement and the topographic phase associated with DEM errors show a linear dependence to the phase change of the pixel through the time series and can be estimated by utilizing a linear model [WERNER et al. 2003]. The atmospheric phase contribution is low-pass in the spatial dimension, i.e. correlated in space, but uncorrelated from pass to pass, therefore, this phase term can be estimated and eliminated by applying spatio-temporal filtering [PRATI et al. 2010], [WERNER et al. 2003].

With the PS technique, sub-meter DEM accuracy and millimetric ground deformation

## 2.1 Ground subsidence monitoring and modeling

estimation can be achieved, since the atmospheric effect is removed [FERRETTI et al. 2001]. In addition to its precision and reliability, the advantages of PS interferometry over the conventional DInSAR processing include estimation of deformation even at the areas where no fringe can be observed on individual interferograms, exploitation of all the available data even with large baselines, estimation of slow displacements, as well as determination of small scale motions of a building or a bridge [PRATI et al. 2010], [FERRETTI et al. 2001].

The absolute precision of PSI deformation estimates is difficult to assess, for instance, the comparison with leveling data is not always guaranteed that the same object is observed both by leveling and by PSI [ADAM et al. 2009]. The accuracy of the PSI technique depends on several factors including the sensor, the number of images, time of acquisitions, the distance from the reference point and the coherence of the persistent scatterers [HOOPER et al. 2012]. With PSI, a centimeter to millimeter accuracy can be achieved for deformation estimations, and even in the case where deformation is linear in time, accuracy can be better than 1 mm/year [ADAM et al. 2009], ([HOOPER et al. 2012]). Due to the achievable precision, persistent scatterer interferometry is regarded as a powerful tool for deformation measurement [PRATI et al. 2010], [KETELAAR 2009], [RAUCOULES et al. 2007], however, various limitations and requirements associated with this technique are also described [CROSETTO et al. 2010].

One of the limitations is related to the density of persistent scatterers. As a prerequisite of sufficient spatial sampling to exploit spatial correlation and isolate orbital and atmospheric phase contributions, a minimum PS density 3-4 PS/km<sup>2</sup> is required [RAUCOULES et al. 2007]. This requirement is usually fulfilled in urban areas, however, in vegetated and forested regions a sufficient density of PS is not reached frequently [CROSETTO et al. 2010]. This applies especially to C-band and X-band data. Since the L-band signal can penetrate the vegetation, usage of this wavelength can provide sufficient density of PS even in natural areas. Being a necessary condition for PSI, PS spatial sampling has to be properly considered for assessing the PSI feasibility [CROSETTO et al. 2010].

Similarly, the temporal sampling of the PS dataset is an important factor for the reliability of PSI analysis. The distribution of the acquisitions in time should be as uniform as possible for a higher precision [FERRETTI et al. 2001]. Moreover, due to statistical analysis employed in PSI processing, a large number of the images, ideally more than 30, is required.

Another limitation is associated with the observable deformation magnitude and aliasing [CROSETTO et al. 2010]. Due to the wrapped phase observations, the capacity of PSI for measuring fast movements is restricted. The critical limit of phase gradient, i.e. maximum rate, in PSI estimation depends on the spatial pattern of the deformation, on its PS sampling density, on the wavelength and on the temporal SAR sampling [CROSETTO et al. 2010].

The linear model assumption used in PSI analysis can have a negative influence for areas characterized by non-linear deformation. Especially in the main deformational areas showing significantly non-linear motion, the final PSI maps may lack PSs, due to the fact that the observed PS phases do not fit to the linear phase model [CROSETTO et al. 2010]. In such cases, the linear model assumption can be a critical limitation, because PSI may be unable to provide estimations over the most interesting area with large deformation rate [CROSETTO et al. 2010].

### 2.1.3 Modeling ground subsidence by radar remote sensing observations

Ground subsidence models are simplified representations of the surface movements and can be used for acknowledging the essential aspects of subsidence, as well as for predicting its behavior. In the understanding and anticipating of ground subsidence, different types of models from diverse perspectives can be utilized.

Depending on the objectives, the input and output of modeling may vary. In geology, a model can represent the tectonic interactions and processes triggered by subsidence. In subsidence engineering, a model may focus on the calculation of the impact of forces, generating the geometry to ascertain the effect of subsidence on the underground mine, the buildings, the infrastructures and to provide mining improvements. In remote sensing, the temporal and spatial evolution of subsidence can be modeled for initial assessment of potentially hazardous areas.

Since the estimations derived by PSI analysis form a set of spatial data, composed of points with geographic location and vertical values, the concept of descriptive modeling in spatial data handling described in FALCIDIENO et al. [1992] forms the framework of ground subsidence modeling in this study. In their work, descriptive modeling is proposed to extent the role of spatial data in the understanding of a natural phenomena by extraction of the implicit information available in the initial set of data. A typical flow of operations of descriptive modeling includes the collection of a set of estimations and the derivation of a geometrical model. At the final stage the geometric models can be further interpreted to generate secondary models [FALCIDIENO et al. 1992].

Geometric models are derived by the generation of relationships between individual observations. By using continuity and coherence as two characteristics of spatial data, the values in between observations can be synthesized [FALCIDIENO et al. 1992]. In the case of ground subsidence, the aim of a geometrical model is to generate a continuous surface of the deformation by considering the tendency for nearby locations to influence each other, since the subsidence trough is a continuous surface observed by PSI estimation in point locations. In order to produce a geometrical model from PSI point estimations, i.e. predicting the values at unobserved locations, interpolation techniques, especially the

ones designed for spatial relationships, can be utilized as in the work of YASEEN et al. [2013], HUNG et al. [2011], KIRCHER et al. [2003]. With a geometrical model, specific spatial questions can be answered [FALCIDIENO et al. 1992]. For instance, “what is the amount or rate of deformation in a particular location where no observation is available?”.

In order to derive the characteristics of subsidence, a single set of SAR data can be used or different sources of information, e.g. multiple sets of SAR images from different sensors, can be combined. Such multi-sensor integrations can extend the temporal coverage of the ground displacement monitoring by InSAR to a longer period as demonstrated in the work of NITTI et al. [2010] and WALTER et al. [2009]. Furthermore, LAN et al. [2013], NITTI et al. [2010] and WALTER et al. [2009] report an increase in spatial sampling of subsidence by using different wavelengths. The studies applying integration of information stemming from different datasets suggest that the model of the subsidence based on only one dataset can be improved by the additional sets of observations.

The geometric model of the subsidence can further be used for the derivation of interpreted models such as risk zoning. In case of mining subsidence modeling with PSI observations, the interpreted model may indicate the risk zones depending on the subsidence components, e.g. strain, curvature and tilt. With the availability of a subsidence profile (a geometric model), it is possible to extract the subsidence components, since they are derived from the profile as already explained in Section 2.1.1.2. These interpretations may allow the reduction of the impact of subsidence by assessing the type of damage and providing associated improvements for the buildings and infrastructures. However, deriving an interpreted model is not in the scope of this thesis. The present study aims to derive an initial model describing the subsidence, which can be further used for generation of interpreted models.

## 2.2 State of the art

With the availability of vast SAR data from various missions, SAR interferometry has been used extensively to delineate the areas affected by ground deformations as well as to estimate the magnitude of the displacement. Numerous studies in the literature utilize SAR interferometry for mapping ground surface displacements. The phenomena explored by this technique range from natural causes like earthquakes (YASEEN et al. [2013], MASSONNET et al. [1993]) and volcanoes (SAMSONOV and D’OREYE [2012], FROGER et al. [2007], HOOPER et al. [2007], HOOPER [2006], MASSONNET et al. [1995]) to anthropogenic causes including groundwater withdrawal (CIGNA et al. [2012], HELENO et al. [2011], HUNG et al. [2011], LIU et al. [2011], OSMANOGLU et al. [2011], NG and GE [2007]), oil and gas extraction (KETEELAR [2009]), and mining (ABDIKAN et al. [2013], SAMSONOV et al. [2013], NITTI et al. [2010], NG et al. [2010], WEGMÜLLER et al. [2010], GUÉGUEN et al. [2009], PERSKI

et al. [2009], WALTER et al. [2009], JUNG et al. [2007], GE et al. [2007], WEGMÜLLER et al. [2007a], WEGMÜLLER et al. [2007b], COLESANTI et al. [2005], WALTER et al. [2004], KIRCHER et al. [2003], RAUCOULES et al. [2003]).

Rich SAR data archives providing deformation information since 1991 contribute to the increasing applications of SAR interferometry for mapping ground deformations. The SAR data required for interferometry is available from numerous of spaceborne SAR sensors including X-band COSMO-SkyMed and TerraSAR-X sensors, C-band ERS-1/2, Envisat-ASAR, RADARSAT-1/2 sensors and L-band ALOS-PALSAR and JERS-1 sensors. Due to their different characteristics, such as wavelength, spatial and temporal resolution and incidence angle, SAR data from different sensors provide information with different sensitivities and perspectives to the geohazard.

The exploration of SAR data through years led to the development of various methods and approaches for observing the deformation, for example, in time series. Based on the pixels persistent through the time series, PSI technique has become a proven technology for the analysis of ground deformations. The PSI method was first introduced by the authors FERRETTI et al. [2001] with the aim of overcoming the limitation of conventional SAR interferometry, such as temporal and geometrical decorrelation and atmospheric artifacts. Following this advancement, several modified techniques are also developed, enhancing the application of PSI, such as Interferometric Point Target Analysis (IPTA) [WERNER et al. 2003], Spatio-Temporal Unwrapping Network (STUN) [KAMPES 2006] and Stanford Method for Persistent Scatterers (StaMPS) [HOOPER et al. 2007]. To sum up, with the improvements in recent years PSI approach is developed into a fully operational tool providing high precision, wide area monitoring and unique ability to offer retroactive analysis of geohazard behavior [HOOPER et al. 2012], [FERRETTI et al. 2005].

Due to achievable precision with PSI analysis, the method is used in several studies for the detection of ground subsidence and it is demonstrated that PSI is capable of providing precise estimations of deformation for a variety of study sites with different characteristics. Furthermore, several advantages of using PSI for monitoring of ground deformation are reported by many authors. For instance, the deformation hazards due to mining in Roncourt, France occurring between 1995 and 2000 is monitored by ERS-1/2 in the work of COLESANTI et al. [2005], where collapse precursor signs have been clearly detected by the PSI time series analysis when no leveling data was recorded. This implies that SAR interferometry is the only source of information about the dynamics of the deformation before the major collapse itself.

Considering the capability of PSI for subsidence monitoring, WEGMÜLLER et al. [2007a] present several IPTA analysis with C-band sensors (ERS and ASAR) on mine related surface deformation with an aim to achieve market awareness and acceptance of SAR based land surface deformation monitoring. The studies include, among others, monitoring of surface

movements for open-pit mining, above underground gas caverns, solution mining site and active and abandoned lignite mining sites.

Depending on the availability of the data and the settings of the study area, SAR data from different sensors are exploited by different studies. In particular, based on the rich archives of ERS-1/2 and ASAR data, an immense experience on ground subsidence monitoring with C-band (5,6 cm wavelength) interferometry is collected by numerous applications including RASPINI et al. [2014], SADEGHI et al. [2013], CIGNA et al. [2012], TEATINI et al. [2012], HUNG et al. [2011], NG et al. [2011], OSMANOGLU et al. [2011], ZHANG et al. [2011], WEGMÜLLER et al. [2010], NITTI et al. [2010], GUÉGUEN et al. [2009], PERSKI et al. [2009], WALTER et al. [2009], ZHAO et al. [2009], NG and GE [2007], RAUCOULES et al. [2007], WEGMÜLLER et al. [2007a], WEGMÜLLER et al. [2006], COLESANTI et al. [2005] and WALTER et al. [2004]. In Figure 2–5, SAR dataset used for each study can be investigated. However, limitations of C-band data in vegetated areas due to temporal decorrelation is also reported. Furthermore, the investigations has shown that the use of C-band is problematic in the areas of high phase gradient [WEGMÜLLER et al. 2006].

In order to overcome the temporal decorrelation effect in vegetated areas, several studies exploit L-band data. For instance, NITTI et al. [2010] has applied PSI analysis to Wieliczka Salt Mine area, Poland by using longer wavelength of L-band PALSAR data. The work aims to extend the previous C-band analysis especially for the rural areas, neighboring the mine but lacking PS in C-band. Similarly, WEGMÜLLER et al. [2007b] presents several L-band studies for monitoring of mining induced deformation and reports that in vegetated areas the PSI results are enhanced in comparison to C-band monitoring. Other examples can be found in the work of ABDIKAN et al. [2013] and JUNG et al. [2007], who have exploited L-band data for the investigation of mining induced ground subsidence. With the available PALSAR data ABDIKAN et al. [2013] has identified the mining related subsidence in rural and densely vegetated area located in Zonguldak Province of Turkey. Authors note that the estimations derived from the previous C-band analysis have been improved with denser PS points by the usage of L-band data. On the other hand, JUNG et al. [2007] has employed JERS-1 data in order to estimate the ground subsidence in Gaeun coal mining area in Korea.

The difficulties stemming from high gradient deformations can also be overcome by the usage of a longer wavelength. For instance, WEGMÜLLER et al. [2007b] has applied L-band PALSAR data to various mining and land slide areas with high deformation rates. On the other hand, shorter wavelength can also be employed successfully as in the work of WALTER et al. [2009], who has exploited the potential of TerraSAR-X for monitoring of high gradient surface deformations above an active and an abandoned mine, where the previous C-band data showed limitations. It is reported that the higher spatial resolution and shorter revisit time of the TerraSAR-X sensor lead to easier phase unwrapping with the

possibility to measure high deformation rate. Similarly, LIU et al. [2011] uses TerraSAR-X images in order to estimate the ground subsidence in the urban area of Tianjin, China. The authors report that high resolution TerraSAR-X images can dramatically increase the PS density especially in the build-up areas, furthermore, the estimations are quite sensitive to the displacements due to its shorter wavelength. The high resolution TerraSAR-X data is also used in the work of LUO et al. [2014] and AO et al. [2015], in order to estimate the ground subsidence in the urban areas of Tianjin suburbs and Nansha district in China, respectively.

In this regard, the studies indicate that the different limitations associated with PSI can be compensated by selection of an appropriate dataset. In addition to the selection of a suitable dataset, the importance of the adaptation of the PSI methodology to the specific conditions of study site is also implied by the studies. For instance, the mapping of subsidence with high rate at the Prosper-Haniel mine in Ruhr region, Germany, is successfully addressed in WALTER et al. [2004] by integrating subsidence model to the PSI analysis. Similarly, the ground motion with relatively a fast and non-linear subsidence rate is estimated by PSI analysis of TerraSAR-X images in the work of WEGMÜLLER et al. [2010]. The authors suggest that the availability of appropriate data and adaptation of the PSI methodology are the key factors in the study of fast and non-uniform deformations. In their work, it is reported that the high resolution and short revisit time of these acquisitions provide a higher spatial sampling of high gradient subsidence and less deformation phase per period, assisting phase unwrapping. Furthermore, the PSI methodology adapted to the study site provided the non-linear characteristics of the observed mine subsidence. The methodology is essentially a PS approach but the interferograms with small temporal baselines are generated with multiple masters to aid in phase-unwrapping in the case of high deformation rates ( $>50$  cm/year) [HOOPER et al. 2012], [WEGMÜLLER et al. 2010].

Not only the data selection but also the combination of information from different sensors enhances the revisiting frequency and spatial sampling of the displacement, hence offers very promising perspectives for interferometric monitoring of ground deformations. In particular, with the combination of data from different sensors with various spatial resolutions and sensitivities to the displacement, a more accurate and detailed determination of the displacement characteristics can be achieved [FROGER et al. 2007]. Therefore, several studies utilize multi-sensor data. For example, NITTI et al. [2010] extends the previous C-band analysis, by exploiting L-band PALSAR data to increase the spatial sampling of the mine subsidence. Another example of combining C- and L- band data can be found in the work of NG et al. [2011], who has investigated the long term ground subsidence in Beijing, China by the ASAR and PALSAR images. The authors suggest that usage of these two dataset increases the spatial sampling and the detection of high gradient subsidence.

A multi-sensor dataset composed of TerraSAR-X, Envisat-ASAR and ALOS-PALSAR



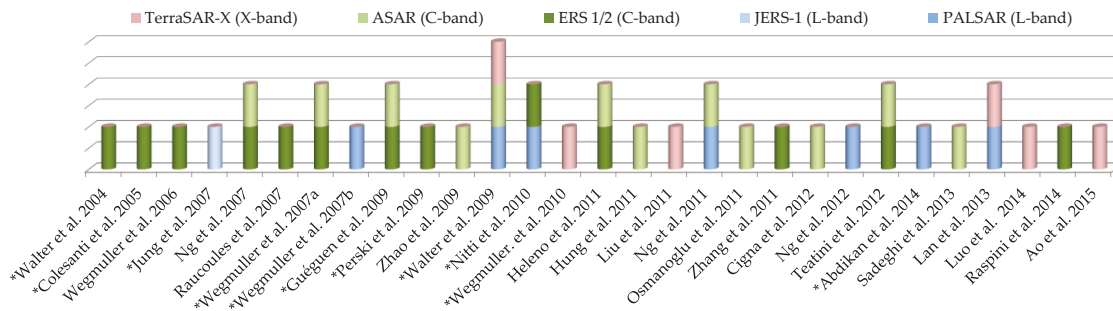


**Figure 2-5:** A selection of studies utilizing PSI for the investigation of ground subsidence phenomena. The bars in the graph stand for the SAR data used for each application. Asterisk (\*) is used to mark the studies investigating mining induced ground subsidence.

is exploited in the work of WALTER et al. [2009]. Furthermore, DInSAR and PSI analysis depending on the availability of the SAR data are utilized for the determination of high gradient surface deformations above an active and an abandoned mine. In other words, results from different datasets and techniques are integrated for a more precise description of the observed deformations.

Another example of integration of multi-sensor PSI results is presented in LAN et al. [2013]. In this work, the PSI analysis of TerraSAR-X and ALOS-PALSAR are carried out for the estimation of ground subsidence in Tianjin Binhai New Area, China. The authors report that the integration of PSI subsidence models from these two sensors has a significant contribution for solving the problems related to common spatial and temporal gaps of single sensor models.

In addition to the SAR data from already existing sensors, the forthcoming SAR missions, ensuring data continuity, contribute to an increase in PSI applications for deformation monitoring. With the developing technology, noise and other error sources will be addressed by the new generation missions [HOOPER et al. 2012]. For instance, the temporal decorrelation noise will be reduced by more frequent acquisitions. Additionally, with the improvements in the accuracy of precise orbits, as well as elevation models, residual geometrical errors will also be reduced [HOOPER et al. 2012].

One of the most promising forthcoming mission is the Sentinel-1 satellites from European Space Agency (ESA). Based on a constellation of two satellites, the Sentinel-1 mission is developed for continuation of the C-band SAR data flow provided by its predecessor ERS and Envisat. The system has been designed to reduce the limitations of InSAR applications by guaranteeing a revisit cycle of six days and a small orbital tube [SALVI et al. 2012]. Contrary to the new X-band sensors Cosmo-SkyMed and TerraSAR-X, having also a short revisit time from 4 to 11 days, however, with limited coverage for high costs, Sentinel-1 will provide global and freely accessible observations providing present and

past ground motion information for any target [RUCCI et al. 2012]. With the high frequency of observations and the regularity of data acquisitions more accurate estimation of ground deformations will be possible for both conventional and multi-temporal InSAR techniques. Furthermore, due to lower impact of temporal decorrelation, hence more effective filtering for atmospheric phase components, a higher spatial density of measurement points is also expected by Sentinel-1 data [SALVI et al. 2012].

The launch of ALOS-2 by the Japan Aerospace and Exploration Agency (JAXA), equipped with L-band SAR sensor PALSAR-2, assures the continuity of the L-band SAR archive created by ALOS-PALSAR [ROSENQVIST et al. 2014]. Similar to Sentinel-1, small orbital tube and a high revisiting frequency of 14 days is used for ALOS-2 in order to accommodate short interferometric baselines and minimize the acquisitions access time [ROSENQVIST et al. 2014].

Continued advances in methodologies and growing collection of SAR data by new generation sensors open new possibilities for sensing of geohazards. Different sensibilities of sensors to the ground deformation, atmosphere and vegetation can be explored by multi-sensor observations. Moreover, the deformation information from different sensors can be integrated, for example, to increase the spatial and temporal sampling of the phenomenon. There is a versatile potential in combining information from different sources. Therefore, especially with the forthcoming satellites, there is a need to develop methods for synergistic usage of sensors to improve the interpretation of ground deformation characteristics. As a consequence of this improvement, the confidence of hazard assessment also increases [LAN et al. 2013].

# Chapter 3

## Research Needs and Study Objectives

Based on the insights acquired from the current state of the art in the field of radar remote sensing for deformation monitoring and from the review of SAR data archives and future acquisitions, in this chapter the research needs are summarized to formulate the main aims and objectives of the present study.

The need for geohazard observation can clearly be seen in the form of assessing the risk posed by the phenomenon. SAR interferometry techniques are described in the state of the art as a powerful tool for monitoring geohazards by providing precise descriptions of the displacements and valuable information for risk assessments. Furthermore, in the current state, the immense knowledge acquired and the availability of vast SAR data archives promote further progresses in this field of analysis. Therefore, this research aims, first to evaluate persistent scatterer interferometry for the specific application of Sondershausen mine subsidence.

For the purpose of describing the behavior of deformation in more detail, collection of data from various sources and integration of the acquired information through different datasets is also encouraged in the current state of the art. In this regard, this research secondly aims to explore different sources of information with a multi-sensor approach as well as to derive synergistic information implicit in the multi-sensor dataset.

Following these aims the first main objective is to evaluate the application of PSI technique for ground subsidence monitoring, and hence to assess the spatial and temporal behavior of the subsidence. This also addresses the question “can PSI technique be employed to study the subsidence phenomenon in Sondershausen?”. This question is tackled by

- evaluating reliability and precision of PSI estimations in comparison to the available ground data
- investigating the strengths and limitations of PSI for this specific application
- exploiting a multi-sensor dataset for extending the monitoring period

- investigating the influence of the dataset, hence sensor characteristics on the application of PSI analysis

The second main objective is to extract the implicit information available in the multi-sensor estimations of the PSI analysis. This corresponds to the modeling concept in the thesis. There are two main aspects.

The extension of the information from point to surface, in other words derivation of continuous estimations (geometric models) by using the spatial neighborhood constraints, is the first aspect. The aim here is to provide a tool to answer the question “what is the temporal evolution of the rate of subsidence at any point on the surface?”. Since addressing this question provides estimations also at unobserved locations, the interpretation of subsidence characteristics can be improved, which in turn enhances the understanding of its effect on the surface structures.

With the aim of compensating for a specific limitation of monitoring, the second aspect is the investigation of synergistic potential of a multi-sensor dataset. Considering the specific constellation of dataset used here, it is aimed to propose a method to increase the spatial density of PS estimations at critical areas with undersampling in a certain part of the monitoring period. This correlates to “model refinement” in the modeling concept of the thesis.

# Chapter 4

## Research Site and Dataset Characteristics

This chapter is devoted to the description of the research area and the data used for the analysis. The first part of the chapter (Section 4.1) introduces the geographical and geological settings of the area and provides brief information on the mining activities in the study site and on the geohazard due to the mining.

For the analysis of subsidence, SAR data from multiple sensors are employed. Furthermore, in order to verify the SAR interferometry estimations and to assist the processing of SAR images, leveling data, weather observations and DEM of the study site are also collected. Consequently, the second part of the chapter (Section 4.2) briefly describes the available SAR and supplementary datasets.

### 4.1 Glückauf potash mine field in Sondershausen

The Glückauf potash mine in Sondershausen, being the oldest and deepest operational potash mine in the world, is situated in north Thuringia, Germany. Currently the mine is partly transformed to an adventure mine, i.e. opened for touristic mine experience, and also used for extraction of rock salt to some extent.

The research area is located in the city center of Sondershausen. The SAR scenes also cover its villages Großfurra and Berka as shown in Figure 4–1. The area is situated in low mountain range between the Hainleite in the south and the Windleite in the north and is mainly surrounded by mixed forests and agricultural fields.

#### 4.1.1 Geological setting of the area

The Glückauf mine is situated in the north margin of the Thuringian Basin, a depression in the central and northwestern part of Thuringia, Germany. The basin is bordered by the Harz mountains in the north, by the Thuringian Forest in the south and by the Thuringian slate belt in the east.

The depression is filled with sedimentary rocks of Zechstein and Germanic Trias with almost horizontal bedding [SEIDEL 2003]. The largest deposits are of Triassic age being the

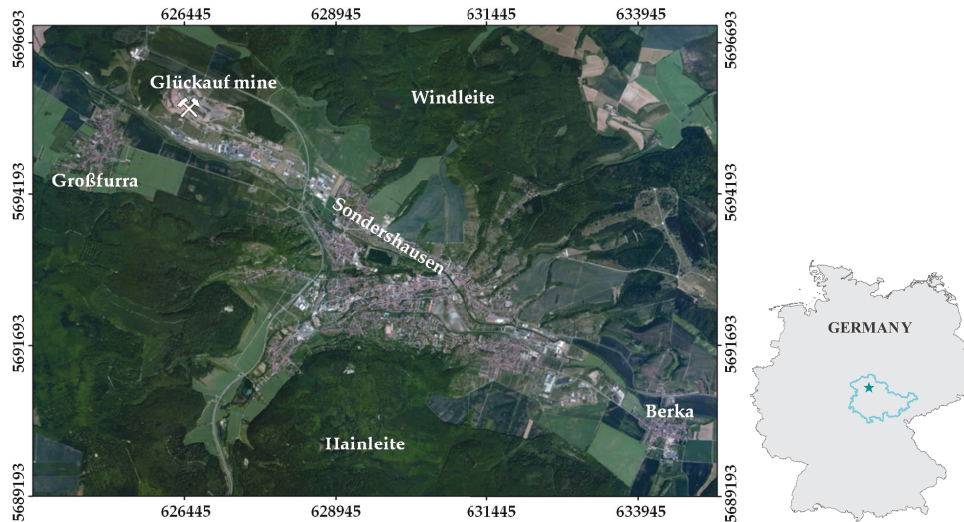


**Figure 4–1:** Research site: Glückauf potash mine field in Sondershausen. The area marked by the blue line on the map of Germany represents the border of the Free State of Thuringia, and by star shows the location of Sondershausen (image source: Google Maps).

Buntsandstein, Muschelkalk and Keuper, a characteristic sequence of rock strata forming the Germanic Trias Group. Below this sequence lie the gypsum and salt layers of Zechstein deposited during middle to late Permian [SEIDEL 2003].

In Tertiary, the present day basin geometry is developed as the African and European tectonic plates collided with one another. The Thuringian basin forms a regional syncline, Thuringian Syncline, whose recent structural configuration is characterized by several NW-SE-trending fault zones [MALZ et al. 2014]. Sondershausen is situated in the south of northwest end of Kyffhäuser-Crimmitschau-fault zone where the layers are uplifted and the upper layers are eroded to the Buntsandstein.

Under these sandstone layers, the Permian salt, i.e. the Zechstein cycle, is accumulated. This sequence consists of huge white and gray layers of Leinesteinsalz and Staßfurtsteinsalz, and in between strata of bright and dark red potassium salt [HOPPE 1959]. The geological columnar section can be found in Figure A–1 for detailed inspection of the stratigraphic sequence at the study site.

#### 4.1.2 The Glückauf mine

Since 1898 mainly potassium salt in the form of Carnallite, Sylvinit and rock salt from the Zechstein sequence are produced from the Glückauf mine of Sondershausen [FLISS et al. 2011]. The room and pillar method is used for the mining, with the central part of the mine field covering an area of  $6 \times 10 \text{ km}^2$ , partially beneath the settlements of the town of Sondershausen with a population around 25.000 [FLISS et al. 2011].

Until the termination of production in 1991, a total amount of 110 million tons of salt (with a maximum annual production of 2.5 million tons) were extracted from depths varying between 600 m to 1000 m beneath the ground surface [TLUG 2005]. Through decades of intensive mining the ground surface was subjected to subsidence, consequently around 1991 critical deformation and instabilities occurred in a mine field located directly beneath the city of Sondershausen. The subsidence rates measured at the ground surface reached up to 25 cm/year and were accompanied by seismic events with magnitudes up to 1.8 in Richter local magnitude scale [FLISS et al. 2011].

From 1991 to 1997 the corresponding section of the mine was stabilized by backfilling of the cavities with rock salt that was excavated for that purpose from a different part of the mine. Following the start of backfilling activities the subsidence rates constantly decreased and by 1997, the number and magnitude of seismic events are also gradually reduced, so that presently only very weak activity is recorded [FLISS et al. 2011].

The mine was reopened for touristic visits in 1996 and since then it is further backfilled with industrial material [MARX et al. 2005]. In 2006 halite production from Staßfurtsteinsalz layers is started in certain parts of the Glückauf mine.

## 4.2 Dataset

### 4.2.1 SAR image datasets

In order to derive the spatio-temporal characteristics of the ground surface displacement in Sondershausen, SAR data from ERS-1/2, Envisat-ASAR and ALOS-PALSAR sensors were collected. The Single Look Complex (SLC) images were provided by ESA in the framework of a CAT-1 proposal. Table 4–1 shows the details of the acquisition parameters for those three sensors.

**Table 4–1:** Acquisition parameters of the SAR datasets. The columns marked by Num provides the number of images in each stack and  $\theta_i$  gives the incidence angles at the mid-range.

Sensor	Track	Frame	Start	End	Num	$\theta_i$	Orbit
ERS-1/2	480	2565	08.04.1995	23.10.2005	74	23°	Descending
ASAR	480	2565	11.04.2004	12.09.2010	21	23°	Descending
PALSAR	639	1020	02.03.2007	26.07.2010	15	38°	Ascending

The plot of distribution of the scenes in temporal and baseline plane, i.e. baseline graphs, can be found in Figure 4–2. For three set of SAR data, the graphs show the distribution of images in time depending on the perpendicular baseline values. Additionally, for ERS stack a graph of Doppler baseline is provided, because of the large Doppler centroid deviations that ERS scenes exhibit after 2000. The details of this point are explained in the following section.

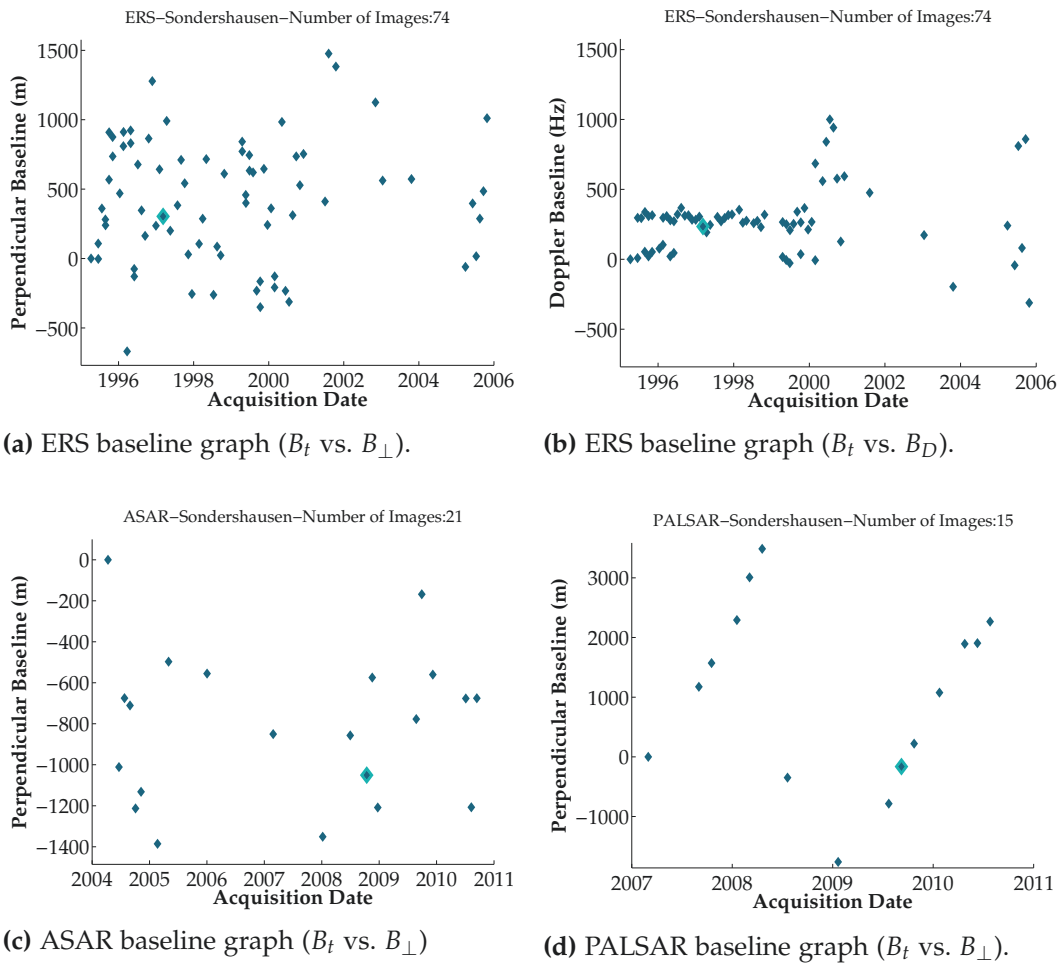


**Figure 4-2:** Baseline graphs of the ERS, ASAR and PALSAR stacks. The Graphs (a), (c) and (d) show the distribution of SAR scenes in temporal baseline ( $B_t$ ) versus perpendicular baseline ( $B_{\perp}$ ) plane and (b) temporal baseline versus Doppler baseline ( $B_D$ ) plane. The images marked by light blue frame represent the selected master images.

The period of monitoring based on the available SAR data covers the years between 1995 and 2010. During this time the Glückauf mine was subjected to backfilling activities to stabilize the displacement, corresponding to the period of gradual decrease of subsidence rate in the deformation history of the study area.

#### 4.2.1.1 The ERS stack

As the baseline graphs in Figure 4-2 indicate, the period from 1995 to 2005 is monitored by the SLCs acquired with the sensors ERS-1 and ERS-2. The ERS sensors operate in C-band, corresponding a wavelength of 5.66 cm. The satellites revisit the study area every 35 days.

All the available ERS-1/2 data until 2000 is included in the analysis. However, the ERS-2



mission suffered from failures of the onboard gyroscopes occurring in early 2000. This affected the Doppler values of SAR images [MIRANDA et al. 2003]. In Figure 4–2 it can be seen clearly that the Doppler values of the acquisitions after 2000 show large variations. The differences in Doppler values before the gyro failure are around few hundred Hz at maximum, whereas after 2000 they reach to 1000 Hz. This high deviation makes the interferometry analysis difficult, because deviations in Doppler values cause decorrelation and with the value being above the critical baseline (1380 Hz for ERS), no information can be extracted from the interferogram.

In order to achieve that the entire period from 1995 to 2010 is covered without any gap, the ERS-2 data between 2000 to 2005 (till start of ASAR acquisitions) is also collected and analyzed for usability in interferometry. The images whose Doppler value differ from the master image more than the critical value are excluded from interferometric analysis. Therefore, only few radar scenes could be used for this period, yielding large gaps between data acquisitions. From 1995 to 2000 the time difference between successive acquisitions are usually around 1 day (due to tandem constellation of ERS-1 and ERS-2), 35 days (one cycle) or 70 days (two cycles). However after 2000, the difference for some scenes reaches up to 525 days (15 cycles) (see Figure 4–2-a). Despite the sparse distribution of acquisitions after 2000, with 74 images the ERS stack has a potential for the derivation of deformation estimations for the period spanning from 1995 to 2005.

#### 4.2.1.2 The ASAR stack

The next period from 2004 to 2010 is investigated by 21 ASAR acquisitions. Similar to the ERS sensors, ASAR operates in C-band, with 35 days revisit time.

The distribution of the scenes is relatively good at the first year of the acquisition period of ASAR with 1 to 3 cycle differences (35 to 105 days), however, between 2006 to 2009 the difference between consecutive recordings reaches up to 12 cycles (see Figure 4–2-c).

#### 4.2.1.3 The PALSAR stack

In addition to ASAR, the years from 2007 to 2010 are covered by 15 PALSAR scenes. PALSAR operates with a longer wavelength of 23.62 cm, with 46 days of revisit time. The L-band dataset from PALSAR is composed of single (FBS) and dual (FBD) polarization modes. The FBD data has only half of the range bandwidth of FBS, nevertheless with oversampling of FBD they can be combined for interferometry [WERNER et al. 2007].

The differences of the acquisition times vary from 46 days (1 cycle) to 184 days (4 cycles), which can be seen in Figure 4–2-d. Having only 15 images in this dataset, it is expected that the accuracy of PSI processing will be affected to some degree, since it is a statistical based approach. The details of the processing are discussed in Section 5.2.1.4.

### **4.2.2 Supplementary datasets**

In addition to SAR images, supplementary datasets including a DEM of the area, weather and surveying measurements are used in the analysis.

- DEM: a LIDAR DEM with 5m resolution, provided by Thuringian Authority of Environment and Geology (TLUG).  
Used for : Coregistration and PSI processing
- Weather data: Time series of meteorological parameters of each selected station, covering the period 1995–2011. The data is provided by German Meteorological Service (DWD)  
Used for : Master selection
- Surveying data: Time series of height change and map coordinates of 137 surveying points. The measurements are taken annually with leveling network providing 1 mm height accuracy. The time series covers the entire period of monitoring with SAR data from 1995 to 2011.

The surveying data is provided by the Glückauf mine management companies GSES mbH and GVV mbH. The surveying network covers only the central part of Sondershausen (see Figure 5–3 in the next chapter for the location of surveying benchmarks).

Used for : validation of PSI deformation maps and models.

# Chapter 5

## Methodology

Dedicated to the methodology, this chapter describes the strategy of data processing in detail following the flow chart presented in Figure 5–1.

In the first part (Section 5.1) the procedure of supplementary data processing is explained. The following section (Section 5.2) describes the operations used for ground subsidence monitoring, starting with the details of SAR processing strategy from SLC data to the end product of PSI processing (Section 5.2.1).

Following the objective of validation, the PSI deformation maps are compared to the ones derived from available surveying data. However, direct comparison is not applicable before translating LOS deformation rates into the vertical component. Furthermore, removal of unreliable estimations from the results is required in particular for the PALSAR output. The details of these steps are explained in the post-processing section (Section 5.2.2) following the PSI analysis of SAR data. After post-processing, the methodologies used for the validation of the PSI results are presented under validation strategies (Section 5.2.3).

The final stage of the research consists of descriptive modeling. For this purpose, the validated PSI estimations are interpolated to generate the geometric models of the subsidence rates. Subsequently, the single-sensor model is refined by synergistic usage of multi-sensor datasets. The method of modeling (Section 5.3) including the generation of geometric models (Section 5.3.1) and refinement of the initial model (Section 5.3.2) is described in detail in the final part of this chapter.

### 5.1 Supplementary data processing

In order to assist and validate the PSI analysis, time series of atmospheric parameters measured at several weather stations and precise ground measurements of displacement parameters are collected in addition to the SAR data. In this section, the details of processing strategy for both, weather and surveying data are explained. The information related to the DEM processing, i.e. generating DEM heights in SAR geometry, is provided in Section 5.2.1.3.

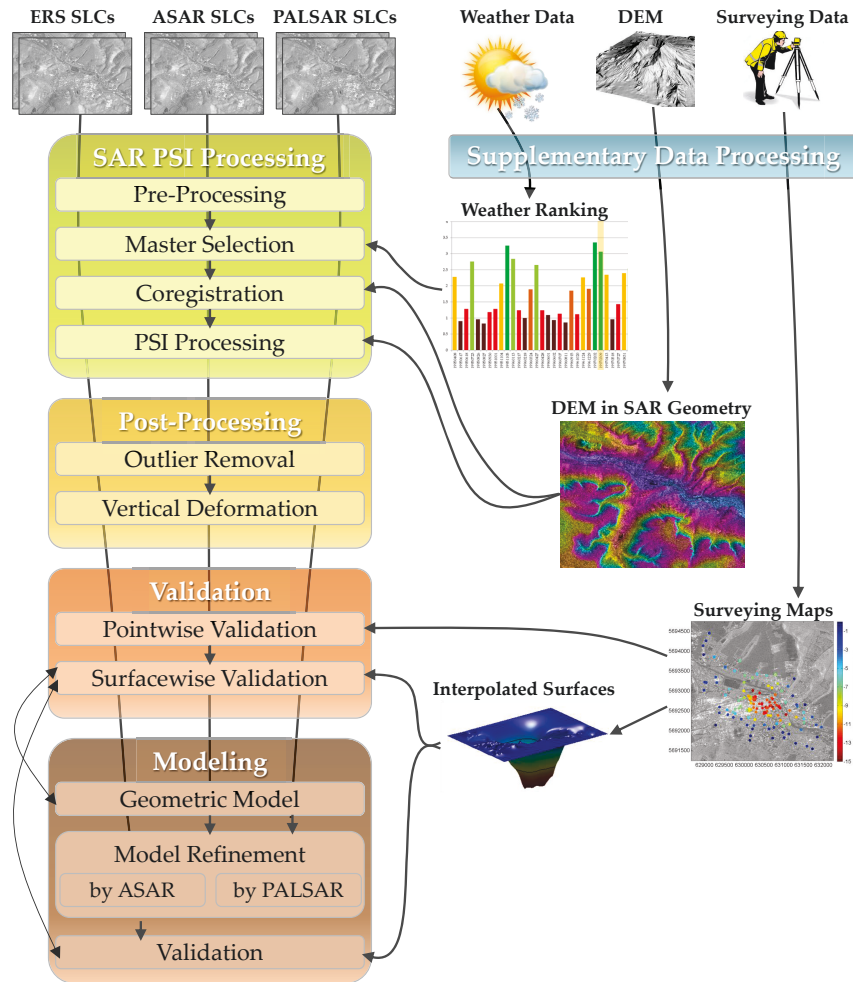


Figure 5–1: Flow chart of the methodology.

### 5.1.1 Weather data processing

The weather data is used for selecting the master scene and also assisting the interpretation of atmospheric influences on the interferograms during PSI processing.

One factor to consider for minimizing the atmospheric artifacts in a stack of interferograms is the influence of weather conditions on the master scene. Since the differential interferograms are generated between the master image and all the slave images during PSI analysis, the image with least atmospheric artifacts should be selected as the reference scene to minimize the atmospheric influence. To achieve this, the weather condition for each acquisition is investigated by structuring and processing of the initial weather data, i.e. by generating weather parameter maps for each acquisition. Furthermore, a scoring system is used to assess the quality of the images based on the weather parameters [KUEHL et al. 2013].

## 5.1 Supplementary data processing

For this purpose, at first, a time series of meteorological parameters from selected stations are downloaded from the DWD database (one file with daily measurements per station). Estimating the weather situation at the time of the SAR image acquisition requires choosing the right set of data, which eventually depends on the availability and dynamics of the parameters [KUEHL et al. 2013]. Among the parameters provided in the time series, atmospheric pressure, air temperature, relative and absolute humidity, cloud coverage, snow height and precipitation are chosen as relevant indicators. The details of the selection criteria are explained in Section 5.2.1.2 dedicated to the master scene selection strategy.

The values of those selected parameters are given in the time series as daily mean, being sufficient for some parameters such as snow coverage, and temperature to estimate the condition at the time of acquisition. However, some other parameters like cloud coverage and precipitation should be recorded as close as possible to the time of collecting SAR scenes for reliable estimation, since these parameters can be very dynamic during the course of a day [KUEHL et al. 2013].

After selecting the relevant weather stations and parameters, new files per date with the values from all the stations are generated by a Java script (one file per acquisition date with values from all the stations). Those files are then used to generate maps for each parameter by interpolating the station values. The weather parameter maps are exploited for the interpretation of atmospheric influences on each acquisition. An example of such maps for the ERS master scene is provided in Figure A-2.

For the calculation of the scores, interpolated values above the study area are averaged. Additional consideration is made here for atmospheric pressure, since this value depends on the station height. Therefore, the values from different stations are first reduced to mean sea level for the sake of unified estimation of air pressure [KUEHL et al. 2013]. The mean of each parameter, as well as minimum and maximum values are used to assign a grade ranging from 0-bad to 1-good to that parameter. To scale the values within this range, a function, selected depending on the characteristics of the weather parameter as linear or non-linear, is fitted to the mean, minimum and maximum values of each parameter [KUEHL et al. 2013].

At this stage the direct or inverse contribution of the parameters to the total score is also considered, the details of which are provided also in Section 5.2.1.2. Following the estimation of a single score for each parameter in the set, the last step is to sum those values for an overall score.

An example of weather scoring result calculated by a MATLAB script can be found in Figure 5-4. In this figure, the upper right plot, titled as weather ranking, shows the scores computed for each acquisition in the ERS stack. The color of the bars (as well as the height) is related to the assigned score. Consequently, the green bars indicate the scenes with relatively good weather conditions, suggesting a candidate list for the master scene.

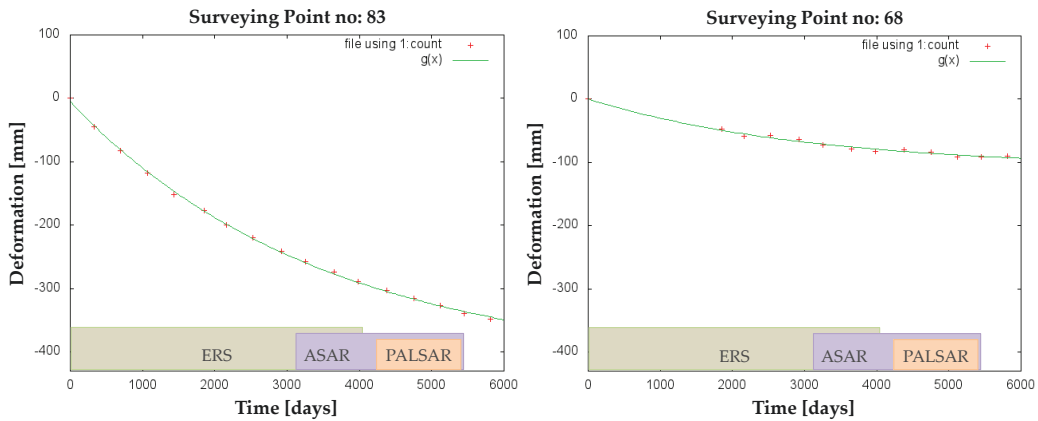


**Figure 5-2:** Surveying measurements on two selected points. Red dots represents the annual ground measurements and green line stands for the fitted function. The starting and ending dates at the graphs correspond to 1995 and 2011, respectively. The left point has measurements every year with a high deformation rate, whereas the measurements in the right one starts at year 2000 (around 2000. day on the graph). The location of point 83 is marked by black square and point 68 is by black circle around the point in Figure 5-3.

### 5.1.2 Surveying data processing

Significant effort is made to evaluate the accuracy of PSI results from different sensors by comparing them with the leveling measurements.

The height measurements at Sondershausen were performed annually by high-precision leveling techniques with point height accuracy of about 1 mm per measurement. In total, 137 surveying points were used for monitoring. The data includes the point map coordinates and the height measurements in millimeter for each point. Most of the leveling points cover the period of 1995 to 2011, however, measurement at some points starts after 1995. Moreover, some of them have gaps for some years. Therefore, for direct comparison of surveying measurements with PSI results, a function is fitted to the time series of measurements for each surveying benchmark.

Because of the non-linear nature of the subsidence observed, an exponential model is used for the fitting. The functional model,  $g(t)$  is written with vertical scale  $a$ , horizontal scale  $c$ , vertical shift  $v$ , starting time  $t_0$  and end time  $t_1$  as,

$$g(t) = a \times \exp\left(-\frac{t_1 - t_0}{c}\right) + v \quad (5.1)$$

With this fitting, the missing values can be predicted, enabling the extraction of the deformation rate of every point for any time frame between 1995 and 2011. Two examples of surveying point measurements and the function fitted to those observations can be found in Figure 5-2.

## 5.1 Supplementary data processing

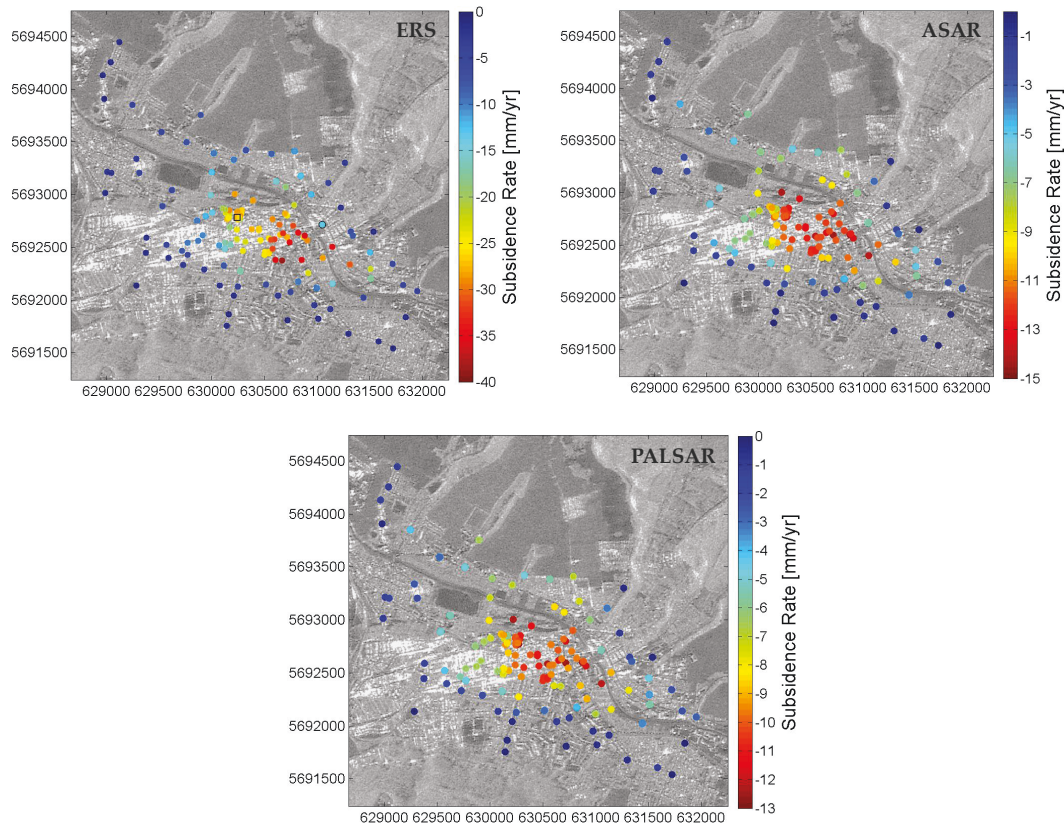


**Figure 5-3:** Linear deformation rates in mm/year derived by surveying data processing for the ERS (1995–2010), ASAR (2004–2010) and PALSAR (2007–2010) stacks. The points are plotted on a PALSAR MLI image. The black square and circle frames on the ERS output mark the points 83 and 68 in Figure 5-2, respectively.

After fitting, the displacement rate  $d_r$  of a surveying point for the desired period is estimated by

$$d_r = \frac{g(t_1) - g(t_0)}{t_1 - t_0} \quad (5.2)$$

where  $g(t)$  is the function fitted to the surveying measurements,  $t_0$  and  $t_1$  denote for start and end of the period of monitoring by SAR data. Note that by this equation linear rates are calculated because PSI results provide only the linear displacement rates. For each point and stack linear subsidence rates are calculated with this procedure by the script written in MATLAB. The results are shown in Figure 5-3, where the color assigned to each point represents the rate calculated by the surveying data processing.

## 5.2 Monitoring

### 5.2.1 PSI analysis of SAR data

In this section, the details of SAR data analysis are presented. The spaceborne radar data is collected as SLC from data providing facilities. Therefore, the analysis starts with preparation of SLCs for PS interferometry including steps like precise orbit determination and radiometric calibration. Since PSI demands accurate coregistration based on a reference scene, the details of master image selection is explained in this section. After coregistration, the stack of SAR scenes is ready for PSI analysis. The strategy applied here for the PSI processing is also described at the final stage of SAR data processing.

#### 5.2.1.1 Pre-Processing

Pre-processing of SLCs for interferometric analysis consists of refinement of the orbital state vectors, radiometric calibration, oversampling and multi-looking. The processing is performed by the functions in the ISP package of GAMMA Remote Sensing Software.

Typically, the orbital data provided by the processing facilities are not fully accurate for precise interferometric analysis. The inaccuracies in orbit information cause baseline errors which reflect to phase measurement as phase noise [HANSSEN 2004]. Therefore, the manipulation of orbital state vectors is included in the processing strategy to improve the accuracy of the position and the velocity information contained in the metadata accompanying the SAR SLC. State vector data for some sensors like ERS-1/2 and ASAR can be updated by external sources, whereas, some sensors, including PALSAR, require no update. In this study, DELFT orbits provided by DEOS are preferred for the generation of precise orbits. In case of absence of a DELFT orbit file of a certain image, PRC (provided by DLR), and DORIS (by ESA) files are used for the ERS and ASAR stacks, respectively.

The signal received by the antenna is not limited to the interaction between the transmitted signal and the target on the surface, but also accounts for other factors such as range spreading loss and antenna gain. These factors introduce fluctuations in the radiometric values throughout the stack, which renders the usability of those values for generation of a point target (persistence scatterer) list for PSI processing. Since the selection of point targets is based on detecting low intensity variability, it requires accurate radiometric calibration. With the consideration of sensor specifications, the ERS, ASAR and PALSAR stacks are successfully calibrated for further processing.

For PALSAR FBD scenes an oversampling factor of 2 is applied additionally in order to compensate for the bandwidth differences of FBS and FBD data. By this way, the same sample spacing as the FBS can be achieved and interferograms between FBS and FBD can be generated [WERNER et al. 2007].



In the pre-processing step, multi-look images are also generated by the multi-looking factors selected for each sensor in such a way that the finest possible resolution with square pixels is achieved. This is done for ERS and ASAR by factor 1\*5 (range, azimuth), resulting square pixels with 20 m resolution and for PALSAR, factor of 1\*3 is used, which gives 10 m resolution. The multi-look images (MLI) are used to assist SLC processing in a variety of processing steps and for visual representations.

### 5.2.1.2 Master scene selection

Coregistration of SLCs in a common geometry requires a reference geometry such that all the remaining data are resampled accordingly. Furthermore, PSI processing uses a master scene in order to estimate the displacement rates in reference to that acquisition. Thereby, a reference acquisition should be selected before proceeding to the next steps.

The strategy to optimize the selection of a master scene relies on certain criteria, which can be categorized in two groups. The first set of parameters consists of perpendicular, temporal and Doppler baseline values of the scenes in the stack. The configuration of baseline values affects the impact of decorrelation in the interferogram. The magnitude of impact defines the useability of an interferogram by inverse proportionality, i.e. the bigger the impact, the less information to be extracted. Therefore, higher correlation is sought in the search of a master scene.

In order to find the image with the highest correlation, an image near to centroid of 3D baseline space is usually taken, either by visual or numerical analysis. For a large stack like ERS, with 74 images, visual analysis is overwhelming. Therefore, a numerical ranking of each image according to baseline values is calculated. A point, representing an image in the 3D baseline space, is ranked by the sum of distances to every other points. For this calculation, Equation 5.3 proposed by HOOPER et al. [2007] is used, which computes the sum of the coherence value for each image. According to their model, total coherence is described as multiplication of different coherence terms ( $\rho$ ) that are depending on Doppler, perpendicular and temporal baselines and thermal noise as shown in Equation 5.3.

$$\begin{aligned} \rho_{\text{total}} &= \rho_{\text{Doppler}} \cdot \rho_{\text{perpendicular}} \cdot \rho_{\text{temporal}} \cdot \rho_{\text{thermal}} \\ &\approx \left[1 - f \frac{B_D}{B_D^c}\right] \cdot \left[1 - f \frac{B_{\perp}}{B_{\perp}^c}\right] \cdot \left[1 - f \frac{B_t}{B_t^c}\right] \cdot \rho_{\text{thermal}} \end{aligned} \quad (5.3)$$

where,

$$f(x) = \begin{cases} x & \text{for } x \leq 1, \\ 1 & \text{for } x > 1 \end{cases}$$

the subscript  $c$  indicates the critical parameter values beyond which the interferogram

exhibits almost complete decorrelation [HOOPER et al. 2007]. Neglecting the thermal noise term (no available information), and using critical values of relevant sensor, e.g.  $B_i^c = 5$  years,  $B_{\perp}^c = 1100$  m,  $B_D^c = 1380$  Hz for ERS, the sum of total coherence is computed and used in ranking of each image in the stack.

The second group of parameters includes weather, season, snow conditions and cloud cover. All these parameters directly or indirectly affect either the impact of temporal decorrelation or the noise in the phase of an image. In order to select the master, supposed to be least affected by any of these parameters, those conditions are evaluated for each image.

Weather conditions as well as the presence of clouds and their characteristics have an impact on changes in the refractive index of the medium, and consequently, on the quality of the phase measurements. For that reason, weather data are collected for the entire period of monitoring and relevant parameters are analyzed for the selection of a master scene.

Atmospheric artifacts are mainly correlated to the water vapor content along with atmospheric pressure and temperature. Good weather conditions for low atmospheric distortions can be characterized as low precipitation, low humidity, no cloud cover and with a stable high pressure field over the area [ZEBKER et al. 1997]. The weather ranking strategy is developed according to these correlations between atmospheric artifacts and weather parameters.

Similarly, the nature of clouds has an influence on the distortions. Clouds are divided into two general categories as stratus and cumulus clouds. The water content in the stratus clouds is usually low compared to cumulus [DING et al. 2008], thus, stratus clouds are generally preferred over cumulus in the selection of a master scene. However, the distribution of clouds should also be taken into consideration. Uneven distribution of stratus clouds can cause differential change in path length over the image, thus, it can be more difficult to isolate the atmospheric influence compared to cumulus clouds with even distribution.

The weather data includes the percentage of cloud cover during day, which provides an overview about the cloud coverage. However, if these values are not close to zero or hundred percentage it can be misleading to assume a certain distribution of clouds in time and space. Therefore, in order to understand the cloud cover and type of cloud at the time of acquisition better, optical weather satellite images (e.g. EUMETSAT, NOAA and MODIS) are also taken into consideration. In this case the challenge is to find images at the time of SAR acquisition. This challenge is valid especially for the ERS and PALSAR stacks. On the other hand, there is a chance to find simultaneous acquisition of radar by ASAR and optical images by MERIS (an optical sensor on board of Envisat), which allows for a good estimate of cloud conditions at the time of recording.

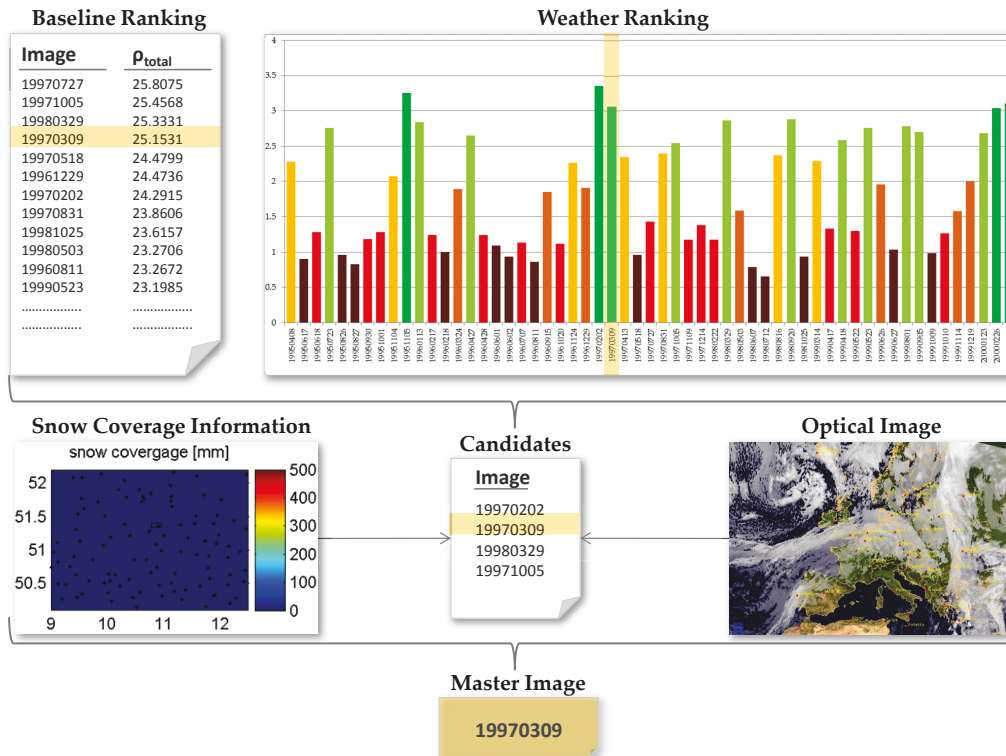


**Figure 5-4:** Master Scene Selection Strategy. An example from the ERS stack. Since no optical image is found for the selected date, a random image is used for the representation.

Season and snow conditions are also relevant to the master scene selection. Temporal decorrelation is usually lower in winter scenes (in the absence of snow) than in summer scenes. Therefore, a winter scene without snow is preferred over summer scenes. Snow cover can be assessed by the weather data time series from nearby weather stations and also by optical images, if available.

A review of the master scene selection strategy based on these criteria is provided in Figure 5-4. Accordingly, in the first step, the baseline ranking is calculated by Equation 5.3. Alongside, a score is assigned to each image calculated from weather parameters. Based on these two scores, a list of candidates is generated. In the next step, the snow information and, if available, optical images are analyzed for the candidates to eliminate the ones with snow and cloud coverage. At the final stage, one scene out of the candidate list is selected as the master. Applying same strategy to different stacks, the images acquired in 09.03.1997 by ERS, 12.10.2008 by ASAR and 07.09.2009 by PALSAR are selected as the reference scenes. The acquisitions are marked by a light blue frame on the baseline graphs in Figure 4-2.

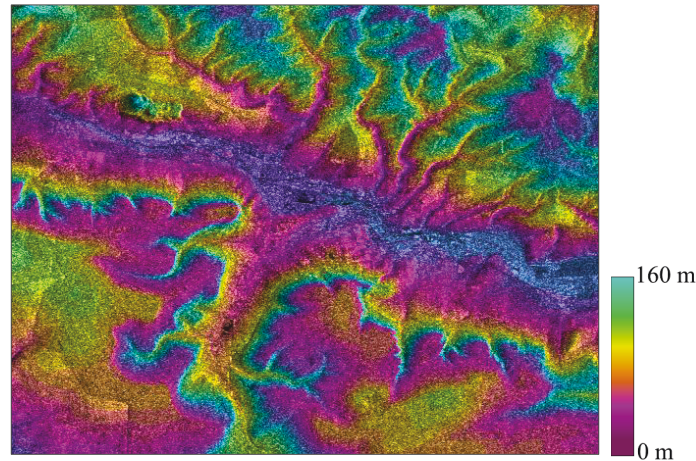


**Figure 5–5:** Topographic height values from DEM in SAR geometry with the color cycle of 160 m, overlaying ERS MLI image.

### 5.2.1.3 Coregistration

PSI processing combines a set of SLC images, thus, requires coregistration of all the scenes to a common reference at sub-pixel accuracy in order to prevent reduction of interferometric correlation. Coregistration includes computing of offsets in range and azimuth directions between two images (slave and master), and resampling of the slave to match with the master image. The approach used in this study to calculate offsets exploits the lookup-table linking the geometries of two SLCs based on a DEM of the area. This has the advantage that offsets due to topography are also considered in the estimations.

The lookup-table approach is also applied for transforming the DEM from map geometry to SAR geometry. The height values in SAR geometry are then used for both, coregistration and PSI processing. Topographic height values in SAR geometry can be seen in Figure 5–5.

Both, DEM processing and coregistration are implemented with the Diff/Geo and ISP packages of the GAMMA software. The coregistration of the ERS, ASAR and PALSAR stacks are successfully performed by this approach using the respective master image as reference geometry for each stack. The quality of registration is assessed by the estimated standard deviation of the offsets in range and azimuth and satisfies the condition of sub-pixel accuracy by values being mostly better than 0.1 pixels.

### 5.2.1.4 PSI processing

The Interferometric Point Target Analysis (IPTA) software package developed by GAMMA Remote Sensing is used for the PSI analysis. The phase model used for IPTA is the same as in conventional interferometry, i.e. the unwrapped interferometric phase is expressed as sum of different phase terms as explained with Equation 2.7. However, the interferograms

are only interpreted for the selected point targets. Therefore, based on the registered SLCs, first of all, a candidate list of persistent scatterers is determined. Two criteria are considered in the selection, yielding two sets of PS candidates for every PSI analysis.

The generation of the first set relies on low temporal variability of the backscattering coefficient. By definition, point targets are the resolution elements where a single coherent scatterer dominates the echo [FERRETTI et al. 2001], [HOOPER et al. 2007]. As a consequence, significantly lower temporal variability than distributed targets is observed for point targets, and hence they do not show speckle behavior [WERNER et al. 2003]. This characteristic is used to derive the first candidate list for each sensor. However, precise determination of this characteristic depends on the number of images in the stack. For small stacks the selection can be unreliable for statistical reasons.

Alternatively, a second set is selected based on spectral characteristics of the point targets. Different than distributed targets the persistent scatterers show high backscattering and low spectral phase diversity [FERRETTI et al. 2001] [WERNER et al. 2003]. This is determined spatially for individual SLCs and therefore, it might work better with small stacks depending on the thresholds.

The quality of the candidate PS list depends on the number of SLCs, the quality of processing and the thresholds applied. Considering the first criterion, reliability of the candidate list increases with the growing number of SLCs. In case of ERS, with 74 images, the stack is large enough to produce a reliable candidate list. However, as it covers a long period (10 years) the number of candidates might be reduced, if some point targets are not available for the whole period. With regard to the number and distribution, the candidates of ASAR stack are consistent with the ones found in the ERS time series. For both of these stacks, the two lists of candidates are merged to one for a final list. On the other side, based on the first criteria the selection of PALSAR candidates is unreliable, because, the size of the stack is very small. Therefore, only the list based on spectral characteristics of the points targets, is used as a final set of candidates.

Due to larger wavelength of PALSAR, the signal can penetrate through tree canopies, moreover, the spatial resolution of PALSAR is finer. Therefore, the number of candidates can be significantly larger than for C-band sensors. However, the impact of the small number of images and the thresholds used for the PS candidate search also influences the outcome. In the final PS candidate list 2795, 3119 and 12842 points are registered for ERS, ASAR and PALSAR, respectively.

In the next step, for the candidate points the SLC values are extracted and initial estimates of the interferometric baselines are calculated from the available orbital data. In this study, a single master approach is used, meaning that the interferograms are generated between master and slave images. If the stack includes  $N$  number of scenes,  $N-1$  interferograms are generated. The extraction of point SLC data is followed by the calculation of  $N-1$

differential interferograms by simulation and subtraction of the unwrapped interferometric phase based on the DEM and initial baselines.

The stack of differential interferograms is analyzed in the following steps. This is done by examining the baseline and time dependence of the spatial difference in the differential phase for pairs of points [WERNER et al. 2003]. In order to reduce the influence of atmospheric signals and orbital inaccuracies, thereby, to estimate displacement parameters and DEM errors, spatial and temporal phase differences are calculated in a phase regression analysis. Therefore, a spatial and temporal reference are required for the phase regression.

The selection procedure of a reference scene (temporal) is explained in detail in Section 5.2.1.2. The strategy of selecting a reference point (spatial) relies on the criteria that the point should be a high quality point, lying in the stable area (showing no displacement) but not far from the main area of interest. Based on these criteria, a location for a reference point is determined for each stack (see Figure 6–1 in Chapter 6).

With the selection of a reference point, a two dimensional phase regression analysis is done with the dimensions being the perpendicular and temporal baseline of the interferometric pairs and by considering that the interferometric phase model indicates:

- a linear dependence of the topographic phase on the perpendicular baseline component with the slope indicating relative height corrections,
- a linear dependence of the deformation rates on the temporal baseline component with the slope indicating relative deformation rate corrections [WERNER et al. 2003].

The results of the phase regression analysis are the height corrections, linear deformation rates, point quality measures (phase standard deviation from regression fit), residual phases and unwrapped interferometric phase. At this point, the residual phase contains an atmospheric phase component, non-linear deformation and error terms. Different phase terms are distinguished based on their different temporal and spatial dependencies. Baseline errors are low-pass in the spatial dimension but uncorrelated between pairs. Similarly, the atmospheric phase term is low-pass in spatial dimension but it is uncorrelated between different images. The non-linear component is generally low-pass in both spatial and temporal dimension. Finally, the phase noise is random in both dimensions [WERNER et al. 2003]. For differentiation of the different phase terms temporal and spatial filters are applied. Repeating several times in an iterative process, these terms are estimated and removed from the phase model resulting in the extraction of deformation rates for each PS point, which has a higher quality measure than the thresholds applied. The number of point targets in the final deformation rates list amounts to 1465, 1527, and 7237 for the ERS, ASAR and PALSAR stacks, respectively.

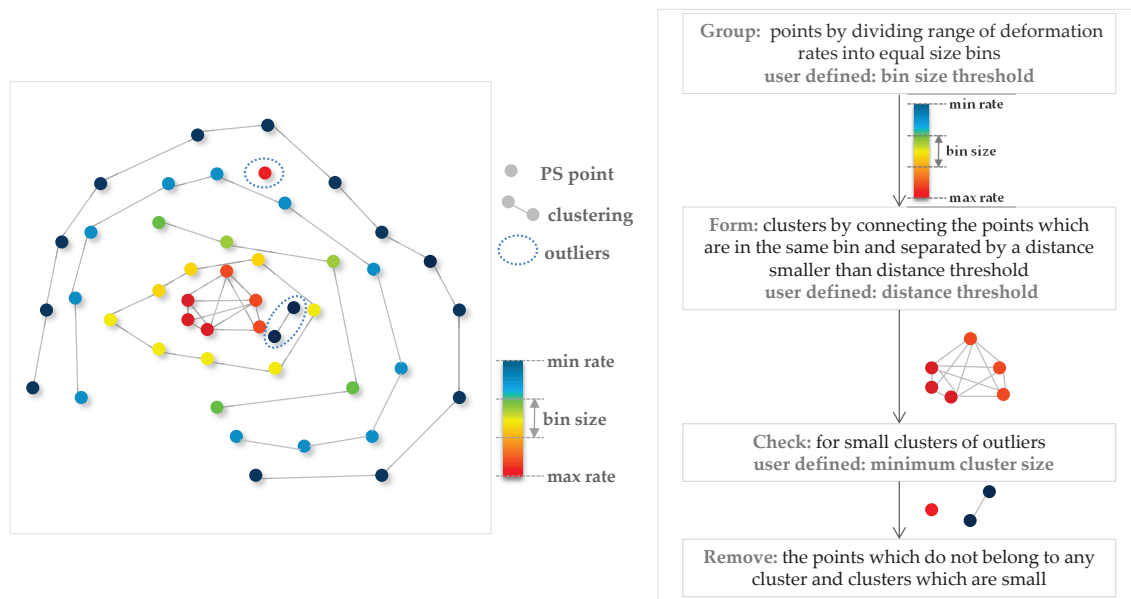


Figure 5-6: Principle and flow chart of the outlier removal processing.

## 5.2.2 Post-Processing

Post-processing implies the operations required before the validation of the PSI results. This includes removal of inconsistent estimations and derivation of vertical displacement rates. The details of these steps are explained in the following sections.

### 5.2.2.1 Removal of outliers and isolated points

An outlier can be defined as a PS point which has a significantly different estimation of displacement in comparison to the surrounding points. Figure 5-6 includes a sketch of outliers on a deformational surface in a map view. As depicted in this figure, the measurements at outliers are inconsistent with the surrounding ones, therefore, developing a strategy for filtering out the imprecise estimations is required.

Different strategies can be implemented for the removal of outliers, depending on the settings in the study area and available input information. An example strategy is explained in KETELAAR [2009], where the PS points grouped into cells by quadtree decomposition. The points deviating more than a threshold from the mean of all the points in the cell are removed.

Sharing the principle of the alternative explained, i.e. clustering the points, a slightly different strategy is implemented in this work. The approach clusters the points, by connecting the ones having similar values and being close to each other, other than grouping them into cells. This has an advantage that the clustering of points into homogenous areas is not restricted to square shape cells, however it can lead to removal of isolated

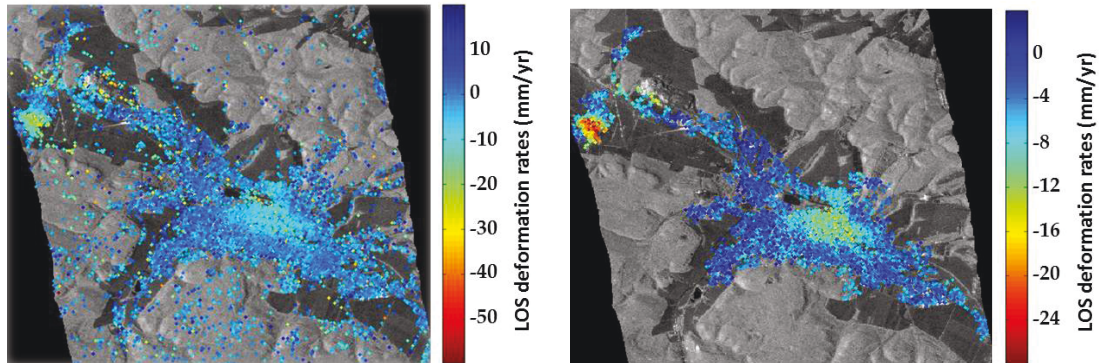


**Figure 5-7:** Deformation maps of PALSAR PSI processing before and after the removal of outliers and isolated points. The left map includes 7237 points and after the removal process (right map) the number corresponds to 6295.

measurements that are far from any major cluster and too small to form a new cluster.

For clustering, the first step is the sorting of points into equal size bins depending on deformation rate values. One parameter is defined to control the bin size, hence the number of clusters. Further consideration made concerning the clustering methodology is the spatial distribution of points. Therefore, a threshold to limit the maximum distance for connecting points is also introduced. After linking the PS points that are close enough to each other in the sense of spatial neighborhood and of deformation rate, the ones which are not connected to any cluster are labeled as outliers. One final threshold as minimum cluster size is used additionally in order to prevent the inclusion of small clusters of outliers in the final version of the deformation maps. The implementation of this approach is summarized in Figure 5-6.

In particular, the PALSAR deformation map is degraded by the presence of unreliable estimations. The reason for that is mainly associated to the low number of images in the stack and low sensitivity of the PALSAR measurements to the observed phenomenon. Time series observation of deformation by 15 images results in lower quality in the selection of PS candidates and less reliable statistics in the estimation of displacement rates and hence, wrong estimations are likely. Furthermore, due to the relatively large wavelength of the sensor (23.62 cm), and small deformation rates (maximum 1 cm per year), the measurements are less sensitive compared to C-band sensors.

As it can be seen in Figure 5-7, the deformation rates of PALSAR before outlier removal ranges between +20 mm/year and -60 mm/year. For instance, the high positive values present in the PALSAR results are not expected, furthermore, they are not observed in the output of C-band sensors. Therefore, the script written in MATLAB for removing the inconsistent estimations is run for this stack. With the bin size threshold of 17 mm/year, the range is divided into 5 groups. A maximum distance threshold of 100 m was efficient



for connecting the points to clusters but excluding the outliers distributed over the image without any neighboring point from the same group. Additionally, by defining a minimum cluster size of 8 points, the small clusters of outliers, as well as the isolated points distributed especially in the vegetated areas are removed. With this processing 242 points in the urban areas and 943 points in the vegetated terrain, where the measurements are sparse and often inconsistent, are removed leaving 6295 points for the final list of PALSAR processing. Due to the high number of isolated points distributed mainly in the vegetational area around the urban settlements, i.e. outside of main deformation area, the number of removed points adds up to a large number. During this processing, some reliable isolated measurements in the vegetated terrain might have been removed which contributes to the large number of eliminated points. Since those points are outside of the main area of interest, the result in Figure 5–7 is accepted as the final version of the PALSAR PSI map. For the cases that the isolated points should be preserved, the minimum cluster size can be set to 1 or the algorithm can be applied separately to the high and low density areas with different thresholds.

#### 5.2.2.2 Derivation of vertical displacement rates

SAR interferometry measures the phase change in the LOS, in other words, estimated deformation rates are the projection of real 3D deformation on the radar's sight. Decomposition of InSAR LOS measurements into vertical, easting and northing components is only possible by the combination of InSAR measurements from different imaging geometries, e.g. ascending and descending orbits. However, in this study only one imaging geometry is available for each sensor, i.e. decomposition is not possible. The available leveling data, on the other hand, provides only the vertical component of the deformation. Therefore, validation of PSI measurements by surveying data requires deriving vertical component of the LOS displacement.

Underground mining subsidence is characterized predominately by vertical motion with much smaller horizontal displacement [PENG 1986]. Therefore, for the purpose of this study the horizontal component is assumed to be negligible similar to the work of YERRO et al. [2014], RAUCOULES et al. [2013], NG et al. [2010], PERSKI et al. [2009] and WALTER et al. [2004]. Under this assumption, the vertical components ( $d_v$ ) is derived from LOS rates ( $d_{LOS}$ ) by knowing the incidence angle ( $\phi_i$ ) with the equation,

$$d_v = d_{LOS} / \cos\phi_i \quad (5.4)$$

Based on this equation, the vertical displacement rate of each point is calculated and a new map of PS displacement rates is generated for every sensor. The histograms generated for LOS and vertical rates can be seen in Figure A–3.

### 5.2.3 Validation strategies

The verification of PS displacement rates with ground measurements can be performed in different ways. One alternative is to compare the point value at a surveying benchmark (or a PS location). The pointwise method uses spatial neighborhood constraints to calculate the differences. Thereby, it provides an overview of how well the deformation regimes are represented by the PS estimations.

Another alternative is to compare interpolated surfaces of PS and surveying point measurements. The differences can be investigated as a continuous surface by the surfacewise method, which provides further insight into the correlation of those datasets.

Similar to the work flow used in KETELAAR [2009] and KIRCHER et al. [2003], both, pointwise and surfacewise validation strategies are implemented and used for interpretation of the differences between PS and surveying. In the following sections, the details of these implementations are provided.

#### 5.2.3.1 Pointwise comparison

The challenge of pointwise comparison is that the neighboring PS and leveling points may not represent the same deformation regime due to their spatial separation [KETELAAR 2009]. If the neighboring points are not located in the same gradient, the differences can be large. In this study, an approach based on an adaptive search radius is developed for the selection of neighboring PS points to address this challenge.

The algorithm implemented in this work for pointwise comparison calculates the differences between the surveying benchmark and the mean of the neighboring PS measurements, which are located inside the area defined by a search radius. As an output, a pointwise difference map, showing the differences at surveying benchmark locations, is generated for the interpretations.

Alternative approaches like a fixed search radius or a fixed number of neighboring PS are also evaluated. However, due to different gradients and non-uniform distributions of points these methods are not as efficient as the adaptive approach to handle different situations, e.g. as depicted in Figure 5–8 around benchmark A, B and C.

Figure 5–8 also summarizes the work flow of the algorithm. As a first step, PS points in the vicinity of a surveying benchmark are located, where the initial search radius is defined by the user. Next, the mean and standard deviation of those points are computed. Depending on the standard deviation threshold, the mean of those points are either compared directly or the search radius is changed. Three cases are considered,

- no point is found in the initial search radius (benchmark A),
- standard deviation of the PS points in the initial search radius is smaller than the

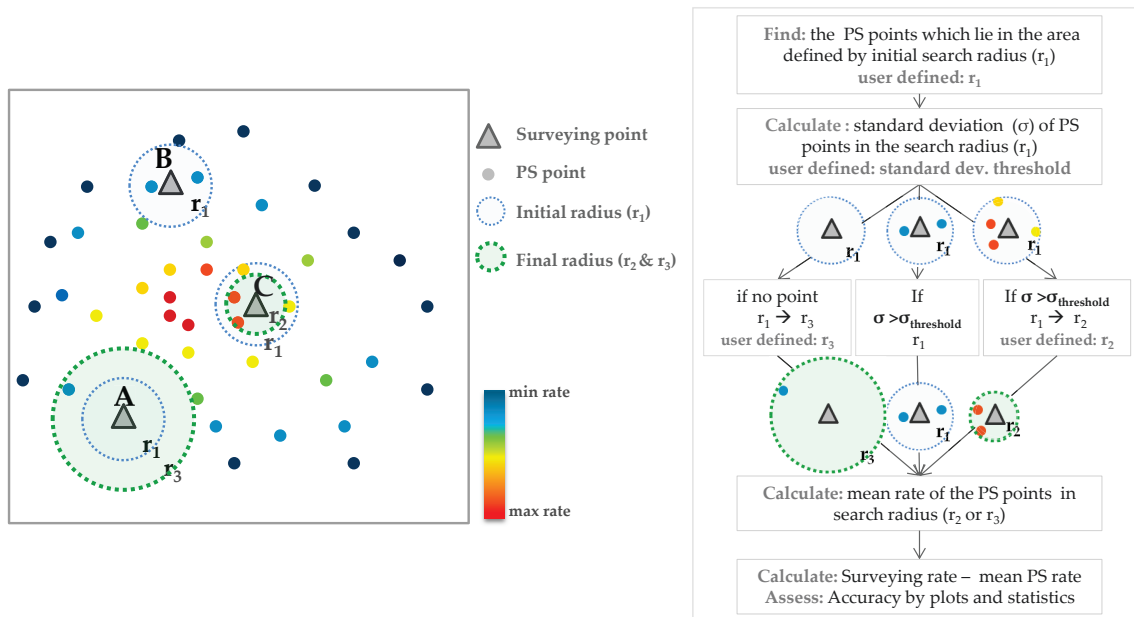


Figure 5–8: Principle and flow chart of pointwise validation.

threshold (benchmark B),

- standard deviation of the PS points in the initial search radius is bigger than the threshold (benchmark C).

In order to cope with the first case, a second radius which is larger than the initial one is used for the PS search. The PS points found in the final search radius are then used to calculate the mean and standard deviation. For the points lying in the same deformation regime, the standard deviation should be low. Therefore, if the deviation is higher than the threshold, the benchmark gets no value on the difference map.

The second case requires no further change in the search radius since the PS measurements represent the same gradient. Consequently, the mean PS value is directly calculated and subtracted from the surveying measurement.

The third case treated in the algorithm in a way that a second radius, smaller than the initial one, is used for PS search. Similarly, the standard deviation is checked and if the condition is satisfied, the difference is calculated or the benchmark gets no comparison. At the final stage, the degree of error between the surveying and mean PS values is evaluated statistically by the normalized RMSE.

### 5.2.3.2 Surfacewise comparison

Since pointwise comparison is affected by the point density differences between PSI and surveying dataset, the PSI results are additionally evaluated based on the differences

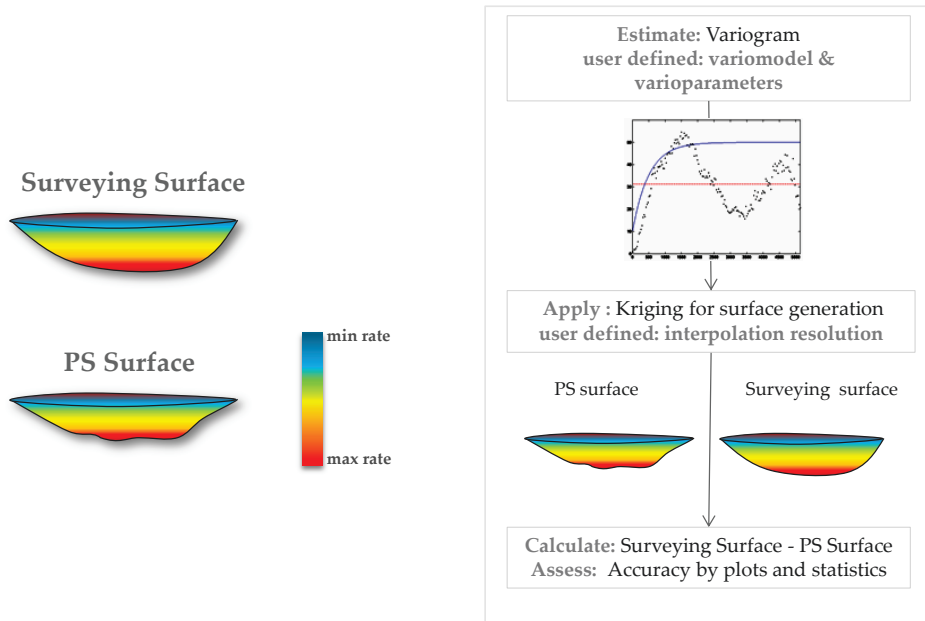


**Figure 5-9:** Principle and flow chart of surfacewise validation.

between the surfaces of those point datasets.

The quality of the surfaces depends on many factors, including the number and distribution of points as well as the algorithm and parameters used for the interpolation. Therefore, the challenge in this method does not lie in finding the neighboring PS, like pointwise comparison, but in generating the best representations of the real surfaces.

As depicted and summarized in Figure 5-9, after the generation of surfaces (see Section 5.3) the surfacewise difference maps are produced by simple subtraction of the two surfaces. Similar to the pointwise, the degree of error is estimated with the normalized RMSE.

### 5.3 Modeling

The PSI displacement maps provide subsidence information only at the location of persistent scatterers, however, in real world the subsidence trough is a continuous surface. Consequently, surface representations improve the understanding of the deformation behavior gained by the point measurements. In order to generate the surface models from PSI maps, the displacement values at arbitrary positions are estimated.

The accuracy of the surfaces derived by interpolation mainly depends on the point density and distribution. In particular, the areas with high gradients require a sufficient number of points so that the interpolation algorithms can estimate the surface gradient effectively. However, due to different factors, spatial gaps are often present in PSI maps.

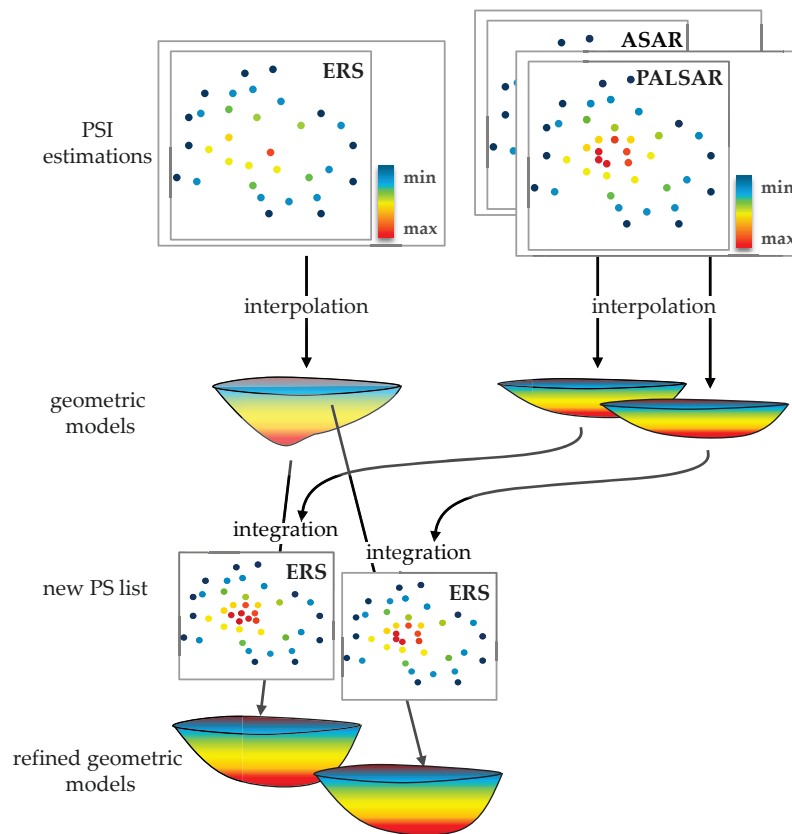


**Figure 5–10:** Flow chart of modeling. The point estimation at PS locations are interpolated to generate geometric models. The initial geometric model of ERS dataset is then refined by synergy with ASAR and PALSAR providing two alternatives for the final geometric model of the ERS stack.

The problem of spatial undersampling is addressed by the methodology used for model refinement. The flow of operations for modeling is outlined in Figure 5–10 and the details are provided in the following sections.

### 5.3.1 Generation of geometric models from PSI estimations

With the objective of providing subsidence values at unobserved locations in the subsidence trough, geometric models for every stack are generated by a spatial interpolation of the point values.

In order to make predictions at unobserved locations, kriging interpolation is used. The basic idea of kriging is to predict the value at a given point by computing a weighted average of the observed values in the neighborhood. Most of the alternatives for kriging assign weights according to functions that give decreasing weights with increasing spatial distance. Kriging, on the other hand, assigns weights according to data-driven weighting

function [ISAACS and SRIVASTAVA 1989].

In many cases, like fairly dense and uniformly distributed data points, kriging will give very similar results to other interpolation methods, however, in general it has several advantages considering the accuracy and lack of bias of the resulting surface [ISAACS and SRIVASTAVA 1989]. For that reason, kriging is selected as interpolation method among others for the generation of surfaces from PSI points similar to the work of HUNG et al. [2011] and YASEEN et al. [2013]. Specifically, in this study the observations are interpolated onto a regular grid by ordinary point kriging, which is implemented based on the description provided in TRAUTH [2010].

Kriging measures distances and directions between all possible pairs of sample points and uses these values to compute variability and probability. The method uses a variogram to express the spatial variation and it minimizes the error of predicted values, which are estimated by the spatial distribution of those values. The variogram is approximated by a model function, i.e. an exponential function in this study since it provides more realistic solutions. Accordingly, three parameters (nugget, sill and range) are used to describe the model function for kriging. Examples of variograms can be found in Figure A-4. On these variograms, the model function is represented by the blue line drawn based on the parameters printed on the graphs.

### 5.3.2 Model refinement: synergy of PSI estimations

The insufficient sampling of critical areas, which is a common limitation of the PSI technique, is addressed by the methodology developed for the synergistic usage of PS estimations from different sensors. The objective of the model refinement proposed here is to increase the spatial sampling at the main deformational area for the period 1995–2005 (the ERS stack), by using the implicit information available in the other datasets.

The center of the subsidence trough in ERS PSI map is intended to be filled with the points that are available in the ASAR and PALSAR maps (the reference maps). However, direct transference of the points from the reference to the ERS map is not applicable since they represent different temporal regimes of subsidence, i.e. the depth of the geometric model is not constant for the ERS, ASAR and PALSAR stacks. In the years from 1995 to 2005 the rates are much higher than the following period, therefore, the point values from the reference stack must be scaled before the integration into the ERS based PSI map.

In case of Sondershausen, the PSI deformation maps indicate a constant pattern of the subsidence with varying depths due to changes in the subsidence rates in time. This behavior is also validated by surveying deformation maps (see Chapter 6 for details), implying that the geometry of the subsidence bowl is not distorted during the monitoring period. Therefore, the strategy to integrate PSI results for model refinement is based on

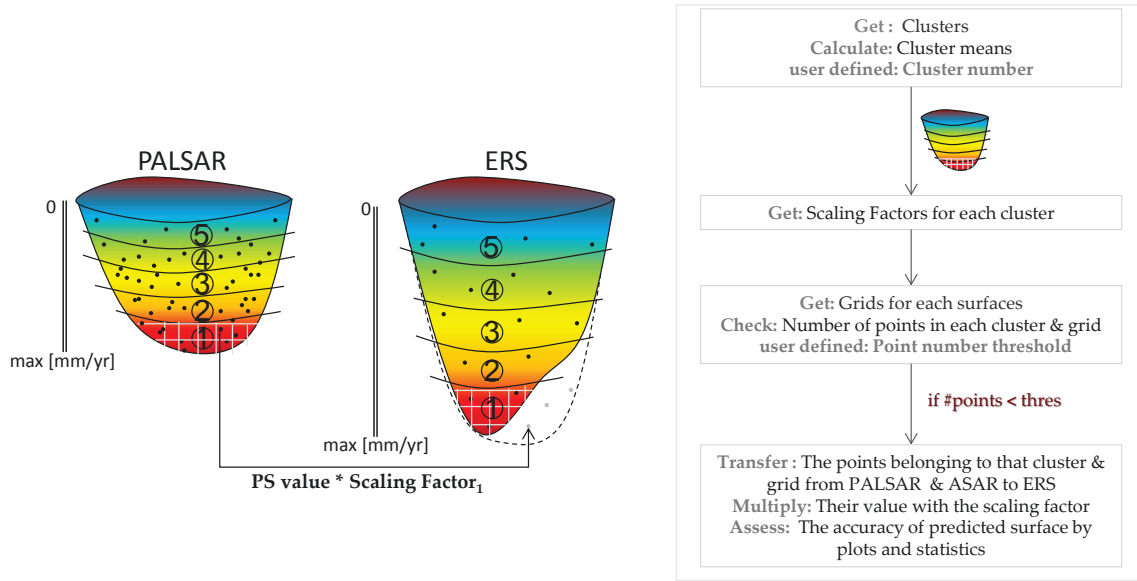


**Figure 5–11:** Principle and flow chart of model refinement. The parallel lines on the surfaces represent the cluster boundaries, in this example 5 clusters are defined. The points stand for the PS points from which the surfaces are generated. The thin light gray lines at the bottom represent the grids for the first cluster. The dash line is the expected shape of ERS surface and also represents the area defined as gap, in other words, the surface aimed to be predicted after the integration.

the assumption that the spatial pattern of the subsidence bowl is not changing for the entire period of PSI monitoring.

Under this assumption, the scale factors are derived by the ratio of the geometric models. In the strategy summarized in Figure 5–11, instead of one global factor, local scale factors are calculated by clustering, in order to account for the variations in surface tangent slopes, i.e. different gradients on the surface. For the calculation of the scale factors, each geometric model are divided into equal number of clusters defined by the user, as shown in the sketch presented in Figure 5–11. With the calculation of cluster means for each cluster of the surfaces, the scale factors assigned to every cluster are computed by,

$$S_k = \frac{\bar{C}_{k-ERS}}{\bar{C}_{k-Ref}} \quad k = (1, \dots, n) \quad (5.5)$$

where  $S$  is the scale factor of the cluster  $k$ ,  $n$  indicates the total number of clusters,  $\bar{C}_{k-ERS}$  represents the cluster mean of the ERS surface and  $\bar{C}_{k-Ref}$  is the cluster mean of the reference surface. After obtaining the scale factors, the value of PS point ( $i$ ) in the reference surface ( $Pt_{i-Ref}$ ) is scaled with the factor of corresponding cluster ( $k$ ) to derive

the point value for ERS ( $Pt_{i-ERS}$ ) with Equation 5.6,

$$Pt_{i-ERS} = Pt_{i-Ref} * S_k \quad (5.6)$$

For the search of points to be transferred from the reference to the ERS map, the surfaces are additionally divided into grids so that a local investigation can be made. Aiming at keeping the originality of the ERS surface as much as possible by filling only the gap, grid-wise search of points is used to control the inclusion of unnecessary points. Following this objective, the number of ERS points is calculated for each grid and cluster. If the number is smaller than the user defined threshold, PS points found in the reference stack are transferred to the ERS point list with the values being multiplied by the scale factor belonging to that cluster (Equation 5.6).

One important point to consider at this stage is that the multiplication of a value means also the multiplication of the uncertainty. In particular, the accuracy of PALSAR estimates are low, mainly due to the small number of SAR scenes in the stack and low sensibility of the measurements due to long wavelength. If every point from PALSAR is included in the transfer list for the new map of ERS PS points, the filled area looks noisy. In order to cope with that, a filtering is applied and the points fail to satisfy the condition are not included in the new ERS map. The upper and lower thresholds for filtering are set to the numbers calculated by multiplication of scale factor with the cluster minimum and maximum of the reference stack. In this case the points which have larger distance to the interpolated surface are filtered out.

Assessing the accuracy of the new ERS surfaces relies on the procedure explained in the validation strategies in Section 5.2.3. To sum up, the validation strategy interprets the difference maps and evaluates the degree of error statistically by computing the normalized RMSE.



# Chapter 6

## Results

Dedicated to the study results, this chapter presents the resulting maps and models of the observed ground subsidence. The gradual surface deformation process induced by mining activities in Sondershausen is investigated by interferometric SAR data analysis. Utilizing the PSI technique, the subsidence is estimated at persistent scatterer locations. The PSI deformation maps (Section 6.1) generated by this way are validated in reference to the ground measurements with the help of validation maps (Section 6.2). The point estimations of the PSI results are then interpolated to model the subsidence trough as a continuous surface (Section 6.3). Finally, a critical area in the geometrical model with insufficient estimations is refined by the synergy of different sensors (Section 6.4).

### 6.1 The PSI deformation maps

The output of the PSI analysis is a dataset consisting of PS point coordinates, point heights, displacement values for each acquisition in reference to the master scene and the model parameters for each PS. In PSI processing a linear subsidence model is used as explained in Section 5.2.1.4. Therefore, the model parameters indicate linear deformation rates. The results of PSI analysis are processed further to remove outliers and derive the vertical component of the deformation rates. The vertical rates assigned to each PS after post-processing are taken as the basis of the subsidence monitoring, as well as the modeling in the further steps.

The deformation maps generated from the ERS, ASAR and PALSAR stacks are presented in Figure 6–1, with the color of the points indicating the vertical subsidence rates in millimeter per year. In order to assist the interpretation of the PSI results, depending on point value distributions, the histograms are additionally provided in Figure A–3. Following the first main objective of the study explained in Chapter 3, the implications of the monitoring results by PSI are summarized for two aspects.

One is the analysis of the results based on the point density and distribution to assess the efficiency of the PSI analysis with regard to the spatial sampling of the subsidence trough.

As indicated by the maps in Figure 6–1, the PSs are located mainly in the urban area. There are only few points on the vegetated terrain mainly because of temporal decorrelation and partly due to removal of the isolated points. To conclude, information that PSI captured in rural regions is insufficient for subsidence monitoring in the vegetated areas.

In contrast, urban areas are mapped with a dense network of 1465 ERS, 1527 ASAR and 6295 PALSAR points covering approximately 20 km<sup>2</sup> including the settlements of Sondershausen and the village Großfurra. However, it should also be considered that the distribution of points is not uniform. For instance, few points are available at the center of the subsidence bowl in Sondershausen due to a lack of urban structures, in particular on the ERS and ASAR deformation maps (see Figure 6–1).

In addition to the absence of man-made structures, the long-term monitoring period of ERS stack and the non-linear component of the subsidence contribute to the poor sampling of fast moving areas. The non-linear component of the subsidence is particularly large in the period of ERS acquisitions, since the deformation rates are much higher compared to the monitoring period of ASAR and PALSAR. Furthermore, the temporal coverage is much longer. Therefore, the limitation of PSI stemming from a linear model assumption (as explained in Section 2.1.2.5) is more prominent in the ERS map. Furthermore, the quality of the scenes, concerning the Doppler values, as well as the sparse distribution of acquisitions in temporal dimension after the gyro-failure in 2000 (see Section 4.2.1) are the other factors affecting the performance of PSI analysis for this stack.

The contribution of such factors to the loss of information is smaller in the ASAR dataset, hence, the point density is higher especially in the high gradient area. Several points are found sparsely distributed at the center of the subsidence, where there is a lack of PS in the ERS estimations. However, the density of points in this region is still low mainly because of absence of urban structures as mentioned.

On the other hand, there are notably more estimations in the PALSAR result providing finer spatial sampling of the subsidence. As a consequence of its longer wavelength and higher resolution, finding more PS in the PALSAR result was expected. However, the small size of the PALSAR stack can also contribute to the large number of PS points. Low number of acquisitions affect the statistical measure of the point quality, therefore, the inclusion of low quality points is more likely. The confidence interval of the PALSAR measurements is lowered further by the fact that the sensitivity to the observed subsidence is low. This is due to its high wavelength/deformation rate ratio (approximately 23 cm/1 cm). Although the subsidence is mapped with a high density, the deformation maps are degraded by these factors resulting in a noisy appearance.

Another aspect relies on the PS values and its implications about the spatio-temporal characteristics of the subsidence. Two main regions of deformation are identified in all three PSI maps. The larger subsiding area is situated in the city center of Sondershausen

## 6.1 The PSI deformation maps

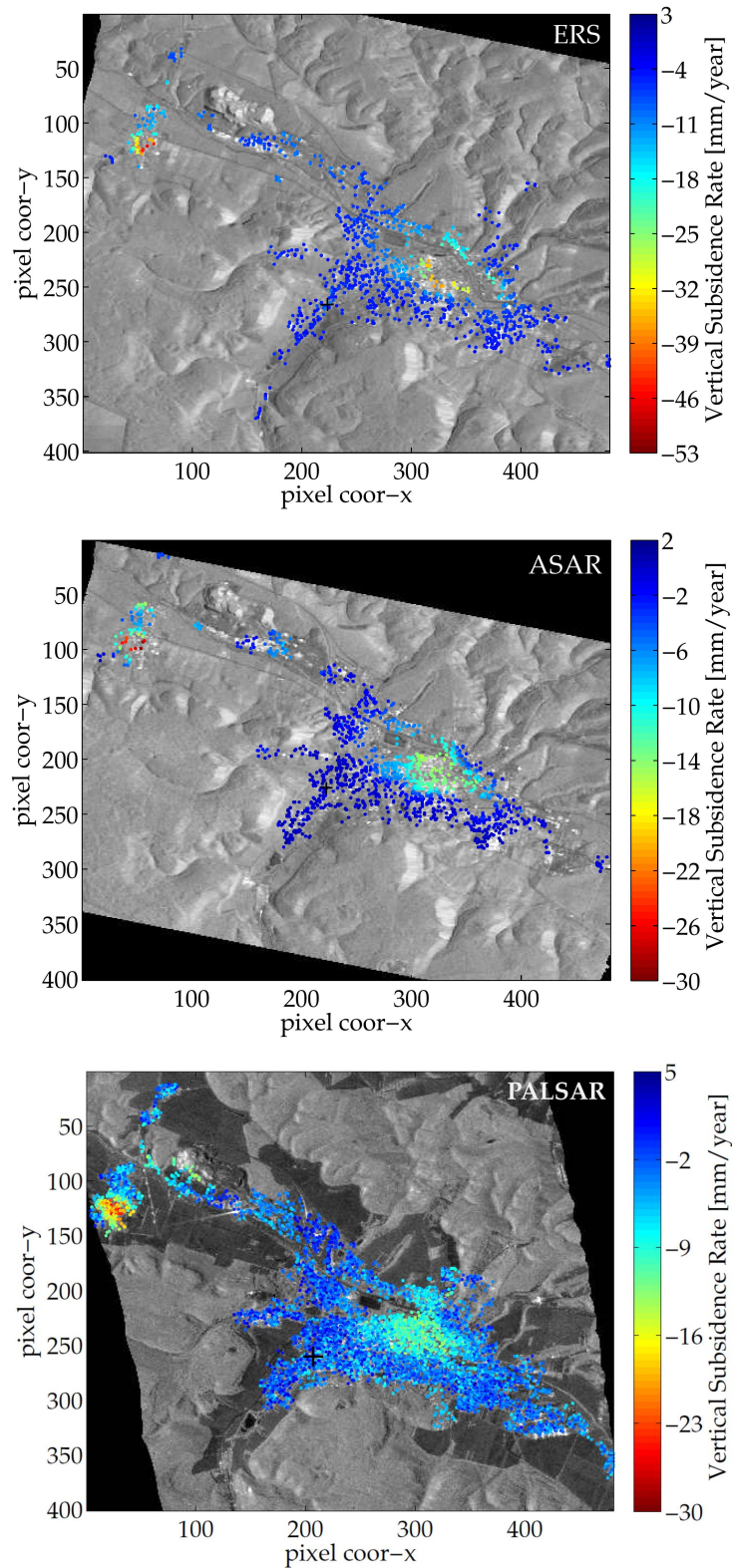


**Figure 6-1:** PSI deformation maps derived from the ERS (1995-2005), ASAR (2004-2010) and PALSAR (2007-2010) stacks. The PS points are plotted on the geocoded master image of the respective stack. The color of the points indicates the rate of vertical displacement in mm/year. The plus sign shows the location of the reference point.

and the smaller site is located in Großfurra. The spatial patterns of subsidence occurring in these sites are clearly represented in each PSI output. Furthermore, the patterns are consistent with each other. This implies that there is no major change considering the shape of the subsidence bowls. As explained in Section 2.1.1, the subsidence trough is usually of circular or elliptical shape for deep lying mining openings. Confirming this, the PSI estimations of subsidence in the Glückauf mine field also indicate an elliptical pattern.

In addition to the spatial behavior, the temporal evolution of the subsidence can also be assessed by combining the information from different time spans, i.e. from different sensors. The ERS estimations suggest that during 1995 to 2005, the rate of displacement is approximately 35 mm/year in Sondershausen and 50 mm/year in Großfurra. Following this period, during ASAR acquisitions from 2004 to 2010, the estimated rates indicate around 14 mm/year and 30 mm/year of maximum subsidence in those areas. Providing additional information from 2007 to 2010, the rates measured by the PALSAR stack are around 13 mm/year at the fast moving areas in Sondershausen, and around 30 mm/year in Großfurra. To sum up, the subsidence rates are decreasing in both locations confirming the effect of mine backfilling on the subsidence. Furthermore, the change in subsidence rate indicates a non-linear trend of the observed phenomenon.

As shown in the histograms presented in Figure A-3, there are some subsidence values with few millimeter above zero. The deviation of the values is mostly related to the accuracy of the point measurements, which depends on the quality of selected PS candidates and the statistical estimations made during PSI analysis. In order to confirm that the estimations do not indicate any uplifting area, these points are further analyzed spatially. Since the positive values are distributed around the non-deformational area, i.e. no grouping of points in certain regions, no uplift is detected.

## 6.2 Validation of the PSI deformation maps

### 6.2.1 Pointwise validation

For the verification of PS displacement rates, pointwise difference maps are plotted and presented in the upper row of Figure 6-2.

On these plots the contours derived from corresponding surveying surfaces are also drawn so that differences can be interpreted depending on their location in the subsidence trough. The second row of graphs in the same figure plot the surveying rates versus the mean PS rates with the color of the points indicating number of PS points used for the calculation of the mean. Furthermore, the relative distribution of surveying and PS points, as well as the number of PSs used for averaging at the surveying benchmarks can be investigated by the graphs presented in Figure A-5.

Additionally, the thresholds used for the comparison are printed on the difference maps in Figure 6–2. The required parameters for pointwise validation, i.e. search radii and standard deviation, are chosen based on certain considerations. One aim is to maximize the number of points receiving a value on the pointwise difference maps. Another aim is to minimize the differences by adjusting the radii and standard deviation. Using bigger search distances can cause larger differences, because as the radii increases, the possibility to include PS points which are not located at the same displacement regime also increases. Therefore, in order to avoid including PS points from different regimes a standard deviation threshold is applied as printed on the difference maps. Based on these considerations, in the search of ASAR and PALSAR points, 200 m for initial search, 250 m for maximum and 120 m for minimum are used. These values can be lower for PALSAR because of its high point density. Therefore, for PALSAR initial, maximum and minimum radius are selected as 120 m, 180 m and 80 m, respectively.

The upper left graph in Figure 6–2 shows the differences between surveying and PS measurements at leveling benchmarks for the acquisition period of the ERS stack. Five points (in black) at the center of subsidence trough have no comparison value, since no PS point is found inside the search radius (see Figure A–5 for relative distribution of the PS and surveying points). The RMSE for the rest of the points is calculated as 0.159. The residual variances in the stable and relatively stable areas are very low, i.e. around zero. On the other hand, in areas with high deformation rates (inside the contour -21) locally high variance is observed. This can also be seen in the corresponding scatter plot. The fast moving points are more scattered around the 1:1 line and up to 15 mm/year deviation can be observed.

Two main regions of under- and overestimation by PSI are observed on the ERS difference map corresponding to the east-northeast and west-southwest of the contour -28, respectively. The first region marked by the yellow points in the plot indicates a difference of -15 mm/year. Since the mean PS rate is subtracted from the surveying rate to calculate the difference, the minus sign indicates that the PS measurements underestimate the rate of subsidence in this area. On the other hand, in the second region values are between +5 and +10 mm/year, suggesting an overestimation of displacement by PSI analysis. For lower subsidence rates the values are very close to each other, furthermore, the number of PS used for averaging is much higher (see the scatter plot in Figure 6–2). However, as the rates increase, the deviations also increase. The reason for these high deviations is mainly associated to the low point density in those regions. Therefore, large search radii are used, which contributes to the large residuals.

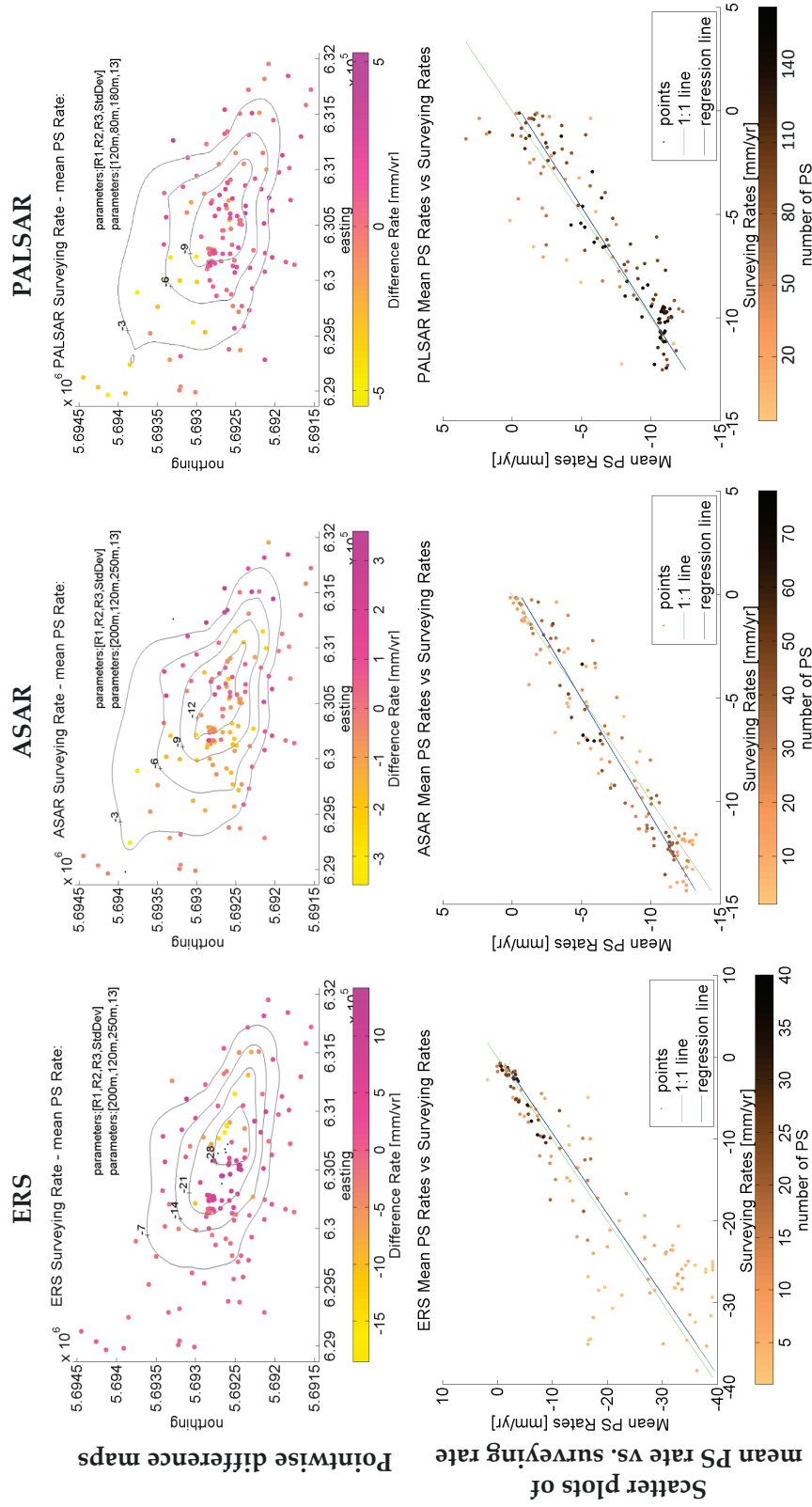


**Figure 6-2:** Pointwise validation of the PSI results. The upper row of graphs are the difference maps of the ERS (1995-2005), ASAR (2004-2010) and PALSAR (2007-2010) stacks, showing the differences in mm/year between the surveying rates and mean PS rates at surveying benchmark locations. The search radii and standard deviation thresholds are plotted on the upper-right corner of each graph. Black color is assigned to the points without a comparison value. The contour lines stem from the corresponding surveying surfaces. The lower row of the graphs are the scatter plots of surveying point values and mean PS rates on which the 1:1 line (green line) and regression line (blue line) are also drawn in order to investigate the tendencies stemming from these two datasets.

The ASAR difference map suggests that the maximum difference is around 3 mm/year. Only two points at the outer regions have no comparison due to absence of PS in the vicinity (see Figure A-5). The RMSE calculated for the rest of the points is 0.095, indicating a lower deviation compared to the ERS stack. This is related to the higher point density of ASAR in the fast moving areas, furthermore, to lower subsidence rates compared to the preceding years.

For PALSAR the differences mostly range between 2-3 mm/year. There are few points with higher differences (yellow points at the northwest part of the subsidence bowl in the validation map in Figure 6-2) with an underestimation of about 5 mm/year. This is mainly caused by the low density of PS points in the close range representing the same regime (see Figure A-5 for relative distribution). In the scatter plot of PALSAR points, it can be clearly seen that the benchmarks with low number of neighboring PS estimations show larger differences. Due to such deviations as well as the fluctuations in the PALSAR estimations, the RMSE is 0.156.

In spite of the local differences, the overall pointwise validation indicates that the PS estimations are consistent with the surveying measurements. The comparisons suggest that fast moving areas are monitored with higher accuracy by ASAR and PALSAR compared to ERS mainly due to higher point densities of the recent stacks.

### 6.2.2 Surfacewise validation

Surfacewise validation is performed based on the surface difference maps derived from pixelwise subtraction of the PS surfaces from the respective surveying surfaces (see Figure 6-4 for interpolated surfaces). The surface difference maps of the ERS, ASAR and PALSAR stacks are presented in Figure 6-3.

The difference map of ERS in Figure 6-3 shows a very similar pattern to the corresponding pointwise map. A RMSE of 0.061 is calculated for the difference, suggesting a good correlation between these two surfaces. However, locally the areas with large differences are also present similar to the pointwise comparison. In the southwest part of the central area between the contours -14 and -28, the PS surface is deeper than the surveying surface between 10-15 mm/year. In contrast, in the northeast part between these contours, the PS surface is higher (underestimation by PSI) around 5 mm/year.

The surface difference map of ASAR is also very similar to the pointwise map in a way that the areas with deviations (under- and overestimation with PSI) coincide. Moreover, the range of differences around -2 to +3 mm/year also matches to the pointwise estimations. The RMSE estimated for this validation is 0.055.

Similar to ERS and ASAR, the regions of under- and overestimation observed in the PALSAR surface map is consistent with the pointwise map, with a maximum of 3 mm/year

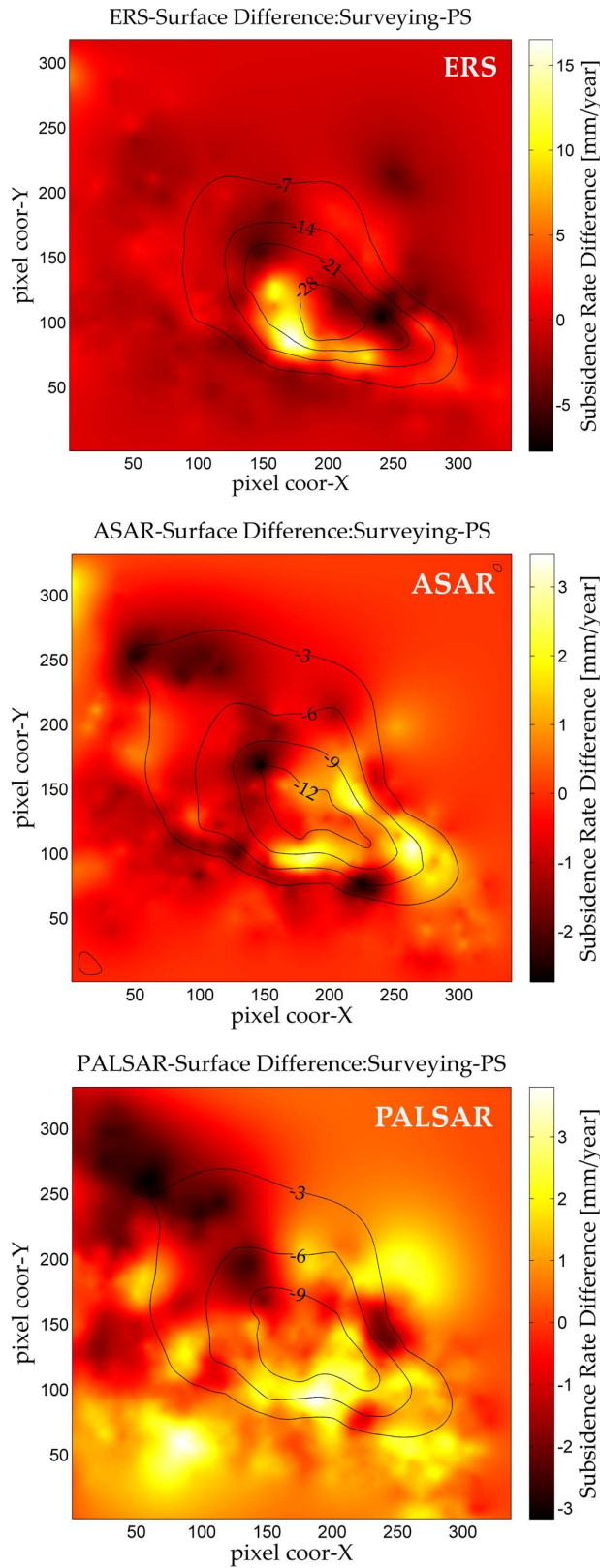


**Figure 6-3:** Surfacewise validation of the PSI results. The graphs show the difference maps of the ERS, ASAR and PALSAR stacks derived from subtraction of the PS surfaces from the surveying surfaces. The contour lines stem from the corresponding surveying surfaces.



over- and underestimation. Although the magnitude of maximum deviations is smaller compared to ERS, a higher RMSE of 0.112, is calculated. One reason for this is that the PALSAR PS surface is rougher compared to other surfaces because of the deviations in the estimations. Furthermore, due to a lack of PSs, the interpolation algorithm has underestimated the northwest part of the surface (dark red-black region in the difference map), which degrades the correlation between PS and surveying surfaces.

Table 6–1 summarizes the validation results. The degree of error for surfacewise validation is lower compared to pointwise for every stack. The number of difference observations is much higher for surfacewise map than pointwise (number of pixels versus number of surveying benchmarks), therefore, the RMSE is less affected by the large deviations occurring in small areas. In addition, with the surfacewise approach only the corresponding pixels are compared, minimizing the impact of search radius, hence, the differences are lower. For instance, the maximum deviation in the PALSAR pointwise map is reduced from 5 to 3 mm/year in surfacewise comparison as shown in Table 6–1. Similarly, the underestimation of up to 15 mm/year indicated by the ERS pointwise map is decreased to maximum of 5 mm/year.

**Table 6–1:** The table provides the summary of the validation estimates for the PSI deformation maps. Minus sign of maximum difference value represents the underestimated areas and plus sign stands for an overestimation by PSI.

	ERS	ASAR	PALSAR
Pointwise RMSE	0.159	0.095	0.156
Surfacewise RMSE	0.061	0.055	0.112
Pointwise max. difference (mm/yr)	-15/+10	-3/+3	-5/+5
Surfacewise max. difference (mm/yr)	-5/+15	-2/+3	-3/+3

However, the difference in the overestimated area by ERS increases from 10 to 15 mm/year. The reason is that the interpolation algorithm overestimates the maximum depth during generation of the surface due to a lack of information in the vicinity, which gives an appearance of the deep narrow depression in the 3D representation in Figure 6–4.

The overall validation suggest that millimeter scale subsidence rates are estimated with high accuracy by the PSI analysis, supporting the reliability of the PSI estimations. However, the accuracy at a high gradient area in the ERS map is degraded significantly. The comparisons at point locations and as surface differences confirm that the undersampling of a high gradient area in the ERS map contributes largely to this deviation.

### 6.3 The geometric models

Referring to the second objective of the study explained in Chapter 3, the continuous spatial information is derived by interpolation of PS point values. In order to verify the geometric

models, the linear rates computed by surveying data processing are used to generate the reference surfaces. Note that only the subsidence area located in Sondershausen is used for modeling since there is no available ground data in Großfurra for the purpose of comparison. Furthermore, the linear subsidence rates are used to represent the geometry of the subsidence trough.

For kriging interpolation, the parameters are optimized for the generation of a smooth surface with a minimum deviation from the original point values. The variograms generated for each surface are presented in Figure A-4, on which the chosen variogram model parameters and the model derived from those variables are plotted. For an exponential model fit, the nugget is used in order to avoid vertical jumps caused by sampling errors and short scale variability. The parameters sill (defines where the model curve becomes horizontal and constant) and range (the zone of influence) affect the smoothness of the interpolated surface such that the higher the values, the smoother the surface. Therefore, in the selection of sill and range values, this relation is taken into consideration. After the generation of variograms, kriging is performed with a final resolution of 10 m, so that there is only one point per cell, i.e. avoiding averaging of point values falling into same cell.

The resultant geometric models are presented in Figure 6-4. The first column of plots in this figure provides the surfaces for each stack and in the second column the corresponding surveying surfaces (see Figure 5-3 for surveying point values) are presented. The third and fourth columns show those surfaces in three dimensions.

The validation of the PS models in reference to the surveying surface and the details of differences are already discussed in parallel to the surfacewise validation of PSI results in Section 6.2.2. Therefore, in this section only the geometrical characteristics of the models are discussed.

The PSI models are evaluated in comparison to the surveying surfaces based on the depth and spatial pattern of the subsidence bowl. In these models, the depth describes the subsidence rates, which is the averaging of the real subsidence values over the total number of years. Therefore, it is directly linked to the dimensions of real subsidence bowl in millimeters. For the ASAR and PALSAR stacks, the maximum depth is consistent with the corresponding surveying model with less than 2 mm/year difference, implying a good estimation of the maximum subsidence by the PSI models. However, with 6 mm/year the difference is larger in ERS because the quality of the surface is degraded by the absence of PS points, thereby, the interpolation algorithm overestimates the maximum values.

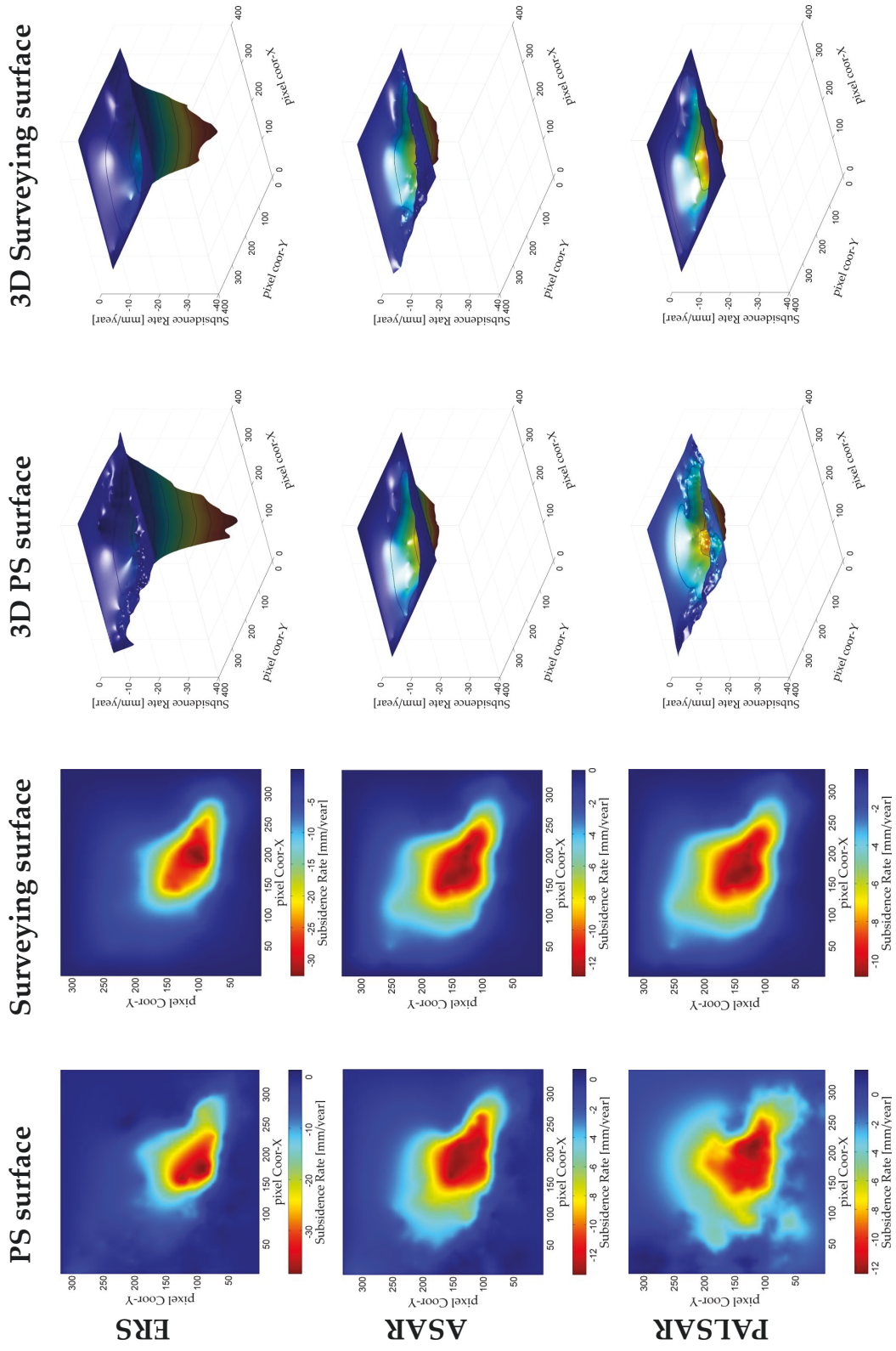


Figure 6-4: The geometric models derived from PS and surveying points in 2D and 3D.

In all the PS and surveying surfaces in Figure 6–4 a common spatial pattern (the southeast-northwest extending elliptical bowl) is clearly represented. However, there are also minor differences. For instance, the location of maximum values in the ERS model, i.e. the deepest part of the bowl, differs slightly from the related surveying model. Moreover, due to a lack of PS points at the center of main deformational area, the width of the bowl is narrower compared to the surveying surface.

The ASAR surfaces have a better agreement on the location of the deepest regions and the width of the bowl. In the PALSAR case, the deepest part of the PS model coincides with the surveying surface, however, the pattern is slightly different. Moreover, the difference in surface roughness is prominent in the PALSAR model because of the high PS density and deviations between estimations of the PALSAR stack. In spite of the noisy appearance of the PALSAR surface, the general outline of the subsidence bowl is also well represented by the PALSAR model.

## 6.4 The refined model

The primary output of the model refinement is a new ERS PS list with point coordinates and linear subsidence rates of original and transferred ERS points. Dividing the original PS surfaces into 10 clusters, and performing the algorithm explained in Section 5.3.2, 83 ASAR and 97 PALSAR points are added separately to the original ERS point list, yielding two new maps for the period of 1995 to 2005. The resultant maps are presented in the left column in Figure 6–5. The scale factors are calculated around 2.8 for ASAR and 3.1 for PALSAR. Considering the fact that subsidence rates decrease by time due to backfilling, a slightly higher scale factor for PALSAR can be expected.

The variables of the integration algorithm are grid size, point number threshold and number of clusters. The grid size has to be selected considering the area to be treated. In this application a grid size of 12\*12 pixels (120\*120 m) was effective to fill the region of interest. Point number threshold was set to 1, meaning that points are transferred if there is no original point available for the selected cluster and grid. This way only the grids being empty are filled, so that the originality of the ERS surface can be preserved. The number of clusters has an impact on the scale factors as well as the filtering, since the factors and the thresholds for filtering are derived from cluster mean, minimum and maximum.

Referring to the objective of integration, the region inside the -21 contour line is successfully filled, furthermore, both solutions are in good agreement considering the spatial pattern and the rate of subsidence. Although several PALSAR PS points are filtered out, a sufficient number of points with good distribution is transferred to the new map.

Finer clustering is preferable considering the fact that especially high gradient areas

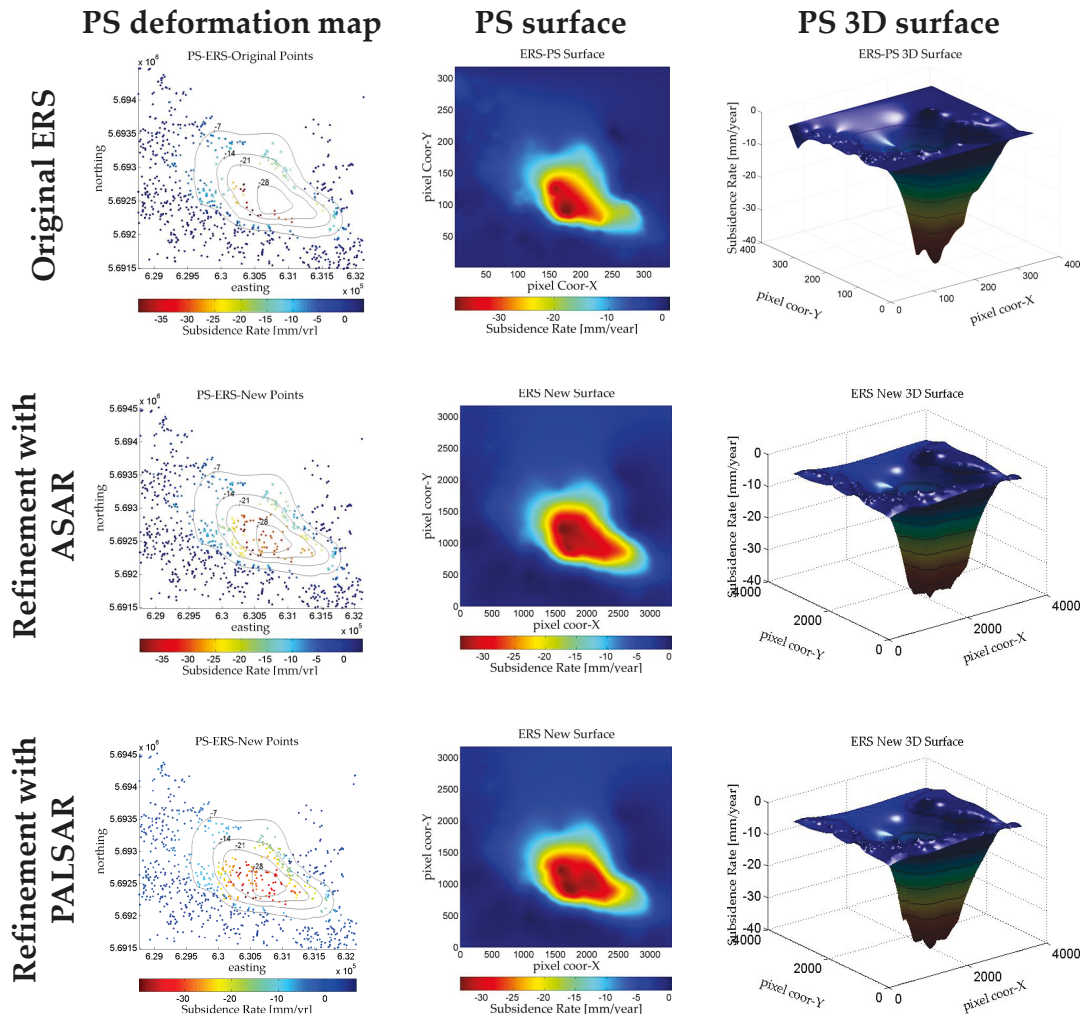


Figure 6-5: ERS original and new deformation maps and models after refinement with ASAR and PALSAR points.

require local treatment. Otherwise the points from different regimes are averaged out. Therefore, cluster number of 10 is selected for the final results in this application. For the purpose of comparison, the results derived by 3 clusters are also presented in Figure A-6 and A-7. The main difference between 10 and 3 cluster solutions appears in the PALSAR integration in such a way that the point values show higher deviations, i.e. a relatively noisy appearance, because the thresholds are less restricting in the filtering due to the larger interval of values in the cluster.

The refined models of ERS generated by interpolation of a new point list are also presented in Figure 6-5. Both of the refined models indicate a decline in the maximum rate, from 39 mm/year to around 34 mm/year, i.e. approximately 5 mm/year decrease in the difference between the PS and surveying surface. Moreover, the width of the bowls is

larger providing a better representation of the geometry.

The results of the integration are validated by the same procedures applied to the original PSI results. The pointwise difference maps are generated for a smaller search radius compared to validation before integration, because many more points are now found at the center of the subsidence bowl. Thereby, search radii of 100, 200 and 220 m were used for the search of PS points around a benchmark.

In Figure 6–6 and 6–7 the pointwise difference maps for the refined ERS models are presented. Both figures suggest that the range of differences is significantly reduced. Before refinement up to -15 mm/year difference is observed, whereas after, the maximum absolute difference is smaller than 8 mm/year for both solutions. Confirming that, the scatter plots in Figure 6–6 and 6–7 also show less deviations from the 1:1 line.

The improvement gained by the refinement is also reflected to the RMSE calculations. The degree of error for original ERS is calculated as 0.159, whereas after refinement, the value is decreased to 0.095 and 0.108 with the synergy of ASAR and PALSAR, respectively.

The surface difference maps are also generated in order to verify the new surfaces derived from the new point lists. The results presented in Figure 6–6 and 6–7 confirm the improvement indicated by pointwise validation, i.e. the differences between surfaces are also reduced. For instance, the underestimated area in the original difference map, i.e. the black region in the northeast of contour -28, shows no more significant deviation. Being consistent with the pointwise validation, the difference in the region southwest of contour -28 in the original difference map (the overestimated area marked by yellow) is also reduced. Consequently, the RMSE for the surface model are also decreased from 0.061 to 0.054 for ASAR and to 0.055 for PALSAR integration.

**Table 6–2:** The table provides the summary of the validation estimates for the PSI models including the original and refined models by ERS-ASAR and ERS-PALSAR synergy. Under- and overestimated areas by PSI are represented by minus and plus signs, respectively.

	ERS original	ERS-ASAR	ERS-PALSAR
Pointwise RMSE	0.159	0.095	0.108
Surfacewise RMSE	0.061	0.054	0.055
Pointwise max. difference (mm/yr)	-15/+10	-8/+8	-8/+8
Surfacewise max. difference (mm/yr)	-5/+15	-1/+10	-2/+10

The improvement is also visible in Table 6–2 that the higher correlations and lower deviations are achieved by the model refinement. However, up to 8-10 mm/year of overestimation still persist. Due to the improvement gained by the integration the area of maximum deviation is smaller as well as the magnitude. Nevertheless, the success attained in the underestimated area is not valid for the overestimated region. Since few original PS points are already present where the deviation is at maximum, this area is not treated by the refinement process due to the objective of preserving the originality of the model. This

indicates that the accuracy of those PS estimations is low, i.e. overestimation of the rate by PSI statistics.

As the RMSE imply the refinement with ASAR gives a better estimation of the missing information. Although PALSAR has a higher point density, the improvement by PALSAR refinement is smaller due to the lower accuracy of PALSAR estimations.

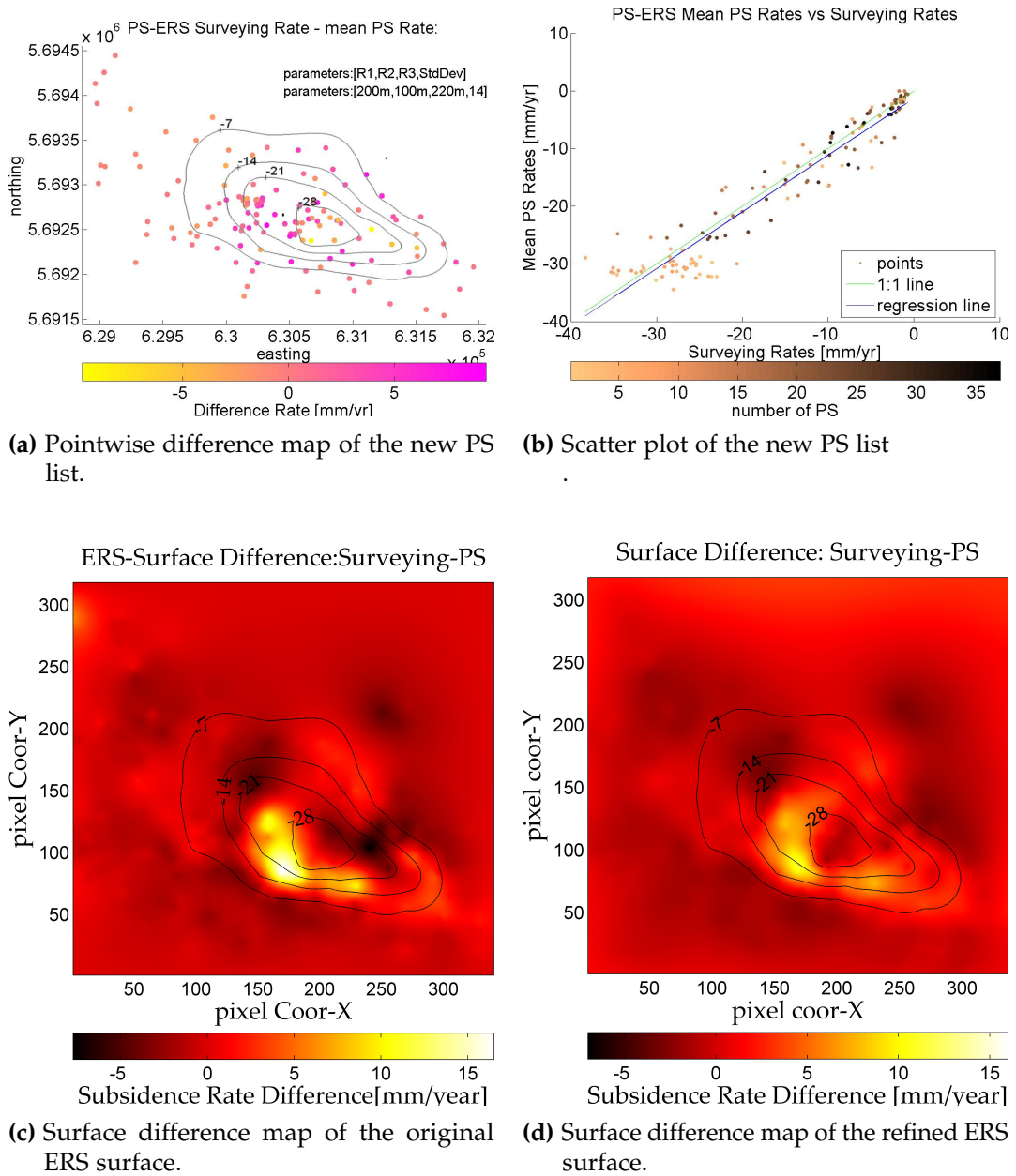
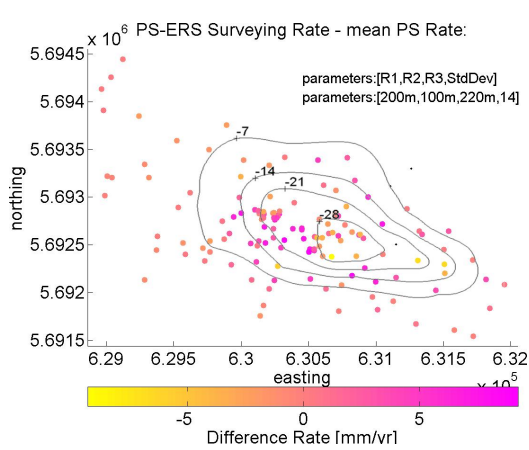
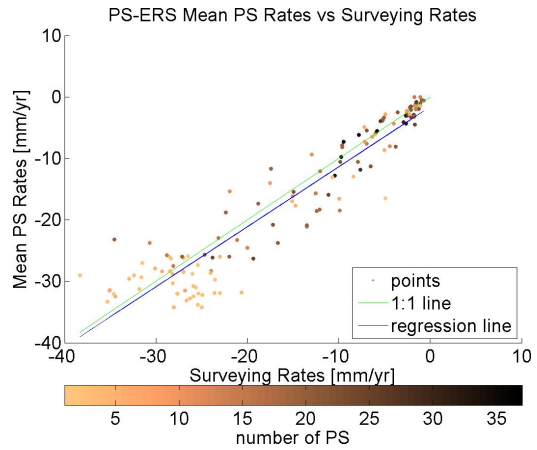


Figure 6-6: Validation of the refinement by ASAR.

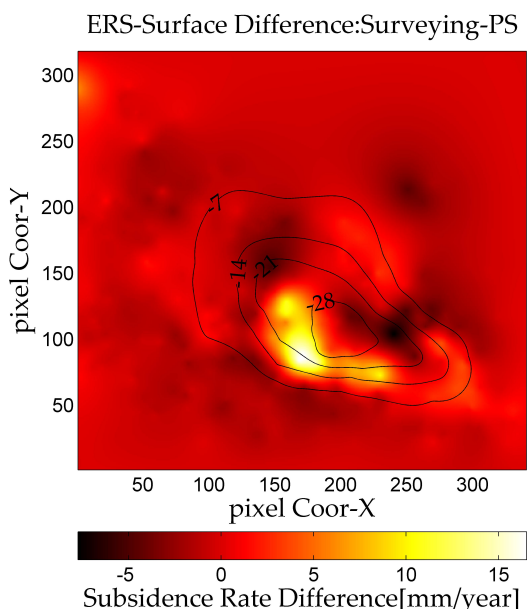




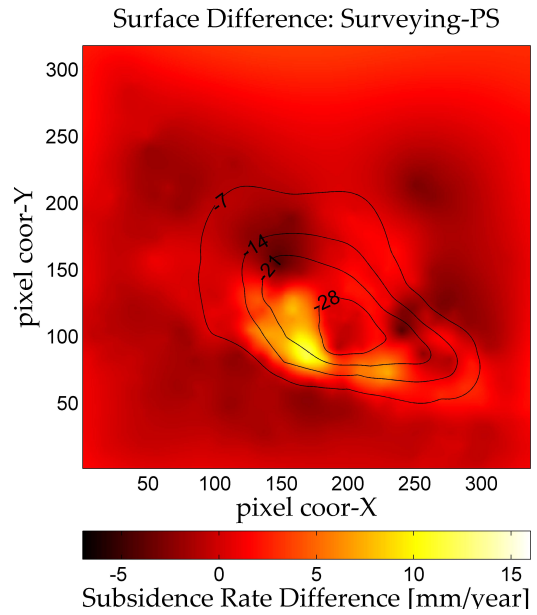
(a) Pointwise difference Rate map of the new PS list.



(b) Scatter plot of the new PS list



(c) Surface difference map of the original ERS surface.



(d) Surface difference map of the refined ERS surface.

Figure 6-7: Validation of the refinement by PALSAR.



# Chapter 7

## Discussion

Understanding the dynamics of ground deformation entails the collection of observations at the Earth's surface. In this research, radar remote sensing technique is utilized for the investigation of the subsidence phenomenon affecting the settlements of Sondershausen. A synoptic view of ground deformation with centimeter to millimeter vertical precision can be achieved by spaceborne radar interferometry [COLESANTI et al. 2005]. Furthermore, the interpretations of the characteristics of the deformation can be improved by the extraction of information implicit in the PSI result. Based on these insights, in the present work the PSI measurements are modeled to derive a geometric representation of the subsidence trough. However, the common problem of spatial gaps in the PSI results degrades the precision of the geometric model. In order to tackle this problem, this study investigates the potentials of synergy between multi-sensor data and estimates the missing information by a novel methodology. In this chapter the potential improvements and capabilities of the methodology, as well as the implications of the study results are discussed. For this purpose, Section 7.1 provides remarks on the processing strategy, which includes the aspects of premises and transferability of the methodology. Secondly, Section 7.2 interprets the study results in reference to the study objectives.

### 7.1 Remarks on the methodology

The applicability of PSI can be degraded by certain limiting factors which are specific to the study site and dataset. In case of Sondershausen, the main restrictions include temporal decorrelation in vegetated areas, non-linear components of the subsidence, irregular distributions of acquisitions in time and low numbers of SAR scenes in the time series.

In this research it is demonstrated that, in spite of these limitations, the PSI deformation maps provide precise measurements of the millimeter scale ground subsidence in Sondershausen. However, the validation of the PSI results in comparison to surveying data also indicates local differences between these two sets of observations. The inaccuracies

in the surveying measurements, as well as the error contributions due to the surveying data processing, have an influence on the deviations. Moreover, the limitations associated with the PSI analysis and the restrictions in the methodologies used in this research contribute to the differences. The potential source of such contributions is discussed based on the premises of the methodology. Furthermore, the alternatives of application areas are discussed from the perspective of transferability of the methodology.

### 7.1.1 Premises of the methodology

The assumptions made during the analysis introduce uncertainties in the application in case the condition is not entirely satisfied. One assumption refers to the negligence of horizontal subsidence components in the translation of the LOS rates to vertical values. Although the horizontal component is small and its surface effects are much less pronounced compared to strain and curvature, accounting for this component would improve the precision. The influence of this assumption is expected to be more prominent in the areas where the horizontal movement is at its maximum, i.e. at inflection points of the subsidence trough. In order to eliminate the error contribution stemming from this assumption, acquisitions from different viewing geometries, e.g. ascending and descending orbits, can be combined to derive the vertical and horizontal components of the LOS estimations.

Another assumption refers to the usage of a linear subsidence model in PSI processing. A 2D regression analysis is performed with the dimensions being the perpendicular and temporal baseline of the interferometric pairs. The analysis is based on the linear dependencies of the temporal and spatial baselines, on the deformation rates and topographic phase, respectively. However, the annual estimations of surveying in Sondershausen clearly indicate a non-linear trend, especially for the fast moving areas. Therefore, ignoring this component degrades the precision of the PSI measurements in both, spatial and temporal dimension. In the case of a large non-linear component, the estimations show high deviations from the linear model. Therefore, these points are eliminated due to their low quality measure (high deviation from the linear fit). Since the non-linear component of the subsidence is especially prominent during ERS acquisitions, the impact of this component on the ERS PSI result is also larger. Therefore, from a spatial viewpoint, the assumption of a linear subsidence model might cause spatial gaps in the resulting deformation maps. The loss can be reduced by the efforts dedicated to the usage of multi-master approach similar to the work of WEGMÜLLER et al. [2010]. Thereby, the need for model refinement can be reduced. From a temporal perspective, the description of the non-linear characteristic of the subsidence for a single stack is limited to a linear model due to this assumption. With a multi-master approach this can also be improved to the extend of defining the trend with a piecewise linear function.

The methodology of integration to overcome the common problem of spatial gaps in the PSI estimations, i.e. synergistic usage of multi-sensor data, relies on the assumption that the spatial pattern of the subsidence is not changing. Therefore, the area of application of this method is restricted to study sites where the subsidence is not affected by, e.g. any major tectonic event or fault which alters the shape of the subsidence. Alternatively, the necessary modifications have to be made for adaptation of the methodology to the site specific conditions.

Furthermore, the method of model refinement is also restricted to the case that the range of deformation values should be known so that the surfaces can be divided into the same number of clusters. In the application of the Sondershausen subsidence, the maximum subsidence values could be approximated by the initial model, therefore, the same number of clusters is used to obtain the scale factors. However, in case of missing clusters (if the initial surface does not represent the range of subsidence values due to the spatial gaps), the maximum rates should be first approximated. For instance, by extrapolation of the mean values of each cluster, the larger values can be predicted. However, the number of missing clusters is a priori knowledge for this approach, too.

### 7.1.2 Transferability of the synergistic modeling

The primary aim of the model refinement is the filling of the voids in the spatial sampling of a deformational surface. To pursue the refinement process, a strategy for the extraction of synergistic information is developed based on the relevant characteristics of the observed phenomenon and the dataset. The deformation observed at the study site can be characterized by (1) gradual - long term deformation (2) subsidence in the form of a subsidence trough, (3) constant spatial pattern throughout its evolution. The important aspect of the data configuration can be described as multi-sensor data covering different time spans. However, the application of the synergistic algorithm is not limited to each of these characteristics. The algorithm designed for synergy uses the geometric proportion of the surfaces to estimate the missing values at one surface. Therefore, the essential aspects are (1) multi-source datasets (at least two, otherwise synergy is not possible) and (2) a constant shape (so that geometries can be scaled). It is, nevertheless, possible to adapt and improve the algorithm to the conditions where the geometry also changes. For this purpose, a different equation for the calculation of the scaling factor can be developed. Such implementations should derive the mathematical relation between two surfaces with different spatial patterns.

The synergistic methodology developed here can be applied to deformations with different origins. Mining induced subsidence is the focus of this study, however, it can also be utilized for the deformations originated from different mechanisms such as volcanoes,

earthquakes and landslides. Since the origin of the displacement defines its characteristics, the varieties of deformation characteristics should be considered in such applications. On volcanoes uplift and subsidence can be observed, earthquakes can produce lateral or rapid motions, landslides may also vary in geometry and speed. The important point in the adaptation of the synergistic methodology is that the relationship between the two surfaces is described mathematically in the form of a scaling factor. If this is achieved, the transferability will also inherently cover the topic of sensor-based characteristics. This implies that the algorithm can be used between different sensors, from X-band to L-band as well as back and forth in time.

## 7.2 Interpretation of the study results

### Does PSI work for Sondershausen?

Providing insight into the question of “can PSI be an alternative or complimentary method in the application to Sondershausen mine subsidence monitoring?” requires description of the limitations and strengths of the PSI deformation maps. In this application the results are restricted to the measurements in urban areas and only the linear rates are estimated. Furthermore, a spatial gap in a high-risk area is observed. On the other hand, PSI maps provide precise estimations over a large area. The coverage is not restricted to the main deformational region like in surveying data, hence a secondary subsidence area in Großfurra could also be investigated without any additional effort. Although there are not enough estimations over rural areas, high spatial sampling is achieved in regions with settlements, where the risk to life is much higher. Despite the fact that the precision of surveying data of 1 mm per measurement and the availability of estimations at a critical location could not be achieved by PSI, the strengths described above suggest that PSI can provide valuable insight into the characteristics of the subsidence. Moreover, it can improve the information gained by ground-based measurements.

The actual accuracy of the PSI deformation estimates in comparison to the surveying data is difficult to evaluate, because of the spatial separation between the PSI and surveying measurements, i.e. they may not represent the same regime of the subsidence [ADAM et al. 2009]. The subsidence rate of up to 35 mm/yr is estimated by PSI analysis on the field of Sondershausen mine with maximum difference of 15 mm/yr at the high gradient area where the impact of the distance between PS and surveying benchmark to the deviation is at maximum. Such difficulties are also reported by several authors including NG et al. [2012] and WEGMÜLLER et al. [2010], who suggest that the high deviations observed in their study are influenced by the mismatch in target points between PSI and ground-based techniques. Despite the fact that large differences are observed at few locations, in this

application the overall match between PSI and surveying measurements are fairly good as indicated by the normalized RMSE values, which are higher than 0.159 for each dataset.

Similar to the assessment of the accuracy, the comparison of the achieved accuracy by PSI in the present work and the previous studies in the literature is also difficult since the deformation and dataset characteristics, as well as the validation strategies (if applied) differ from one application to another. Table 7–1 summarizes the validation assessments for some selected studies that are dedicated to the ground subsidence monitoring by the PSI technique. As it can be seen in this table the comparison is further challenged by the fact that the validation statistics are not equally expressed for each study. Nevertheless, as indicated by the statistical evaluation, it can be concluded that as an alternative or complimentary method, PSI offers precise estimations for ground subsidence studies in Sondershausen. Moreover, the new generation satellites with high spatial resolution, more frequent acquisitions and more stable observations offer promising enhancements in the study of subsidence in Sondershausen.

**Table 7–1:** Validation measures for some selected PSI studies. In the table, max. difference refers to the difference between PS and ground-based measurements and std. dev. stands for standard deviation.

	max. subsidence rate (mm/yr)	max. difference (mm/yr)	std. dev. (mm/yr)	RMSE %
Current study	35	15		0.159
Ao et al. [2015]	40	3,61		
RASPINI et al. [2014]	46	4		
LAN et al. [2013]	17	2		
SADEGHI et al. [2013]	160	2		
NG et al. [2012]	260	29	9	
HELENO et al. [2011]	13	3		
HUNG et al. [2011]	13	3		
LIU et al. [2011]	117		5.6	
OSMANOGLU et al. [2011]	300		7	
ZHANG et al. [2011]	30		2.7	
WEGMÜLLER et al. [2010]	50	20		

### What is gained from the synergistic approach?

Integration of information from different data sources can provide improvements in the understanding of surface dynamics both, in temporal and spatial dimension. In the temporal framework, the synergistic approach combines the multi-source information to derive the temporal evolution of the deformation. A non-linearly decreasing trend was determined in Sondershausen by combining the information from three different measurements in time. Although, the curve was modeled to a certain extend by a piecewise linear function with three lines, the essential temporal characteristics of the deformation was successfully derived. In the spatial framework, the synergistic approach improves

the initially modeled geometry from single sensor estimations. The improvement gained by the refinement in the area of spatial gaps (the underestimated area by the PS model) provides a precision of maximum 1 mm/year deviation from the values modeled by the surveying dataset. Furthermore, the deviation in the overestimated area is reduced to a certain extent by the synergistic approach, although, this area is not inside the gap, i.e. there are original PS points. With the objective of filling only the gap and preserving the already existing information, this area is not directly addressed by the refinement algorithm. Therefore, the improvement in this area is restricted to the refinement in another region. However, a further refinement can be easily employed for this area by using a point number threshold larger than 1 in the integration algorithm. Thereby, new points can be transferred to the grid cells where the original PS points overestimate the surface.

Based on these insights, it is demonstrated that the synergistic approach has a potential to improve the spatio-temporal description of the subsidence. The improvement gained by the refinement can be significant in cases where the subsidence behavior, hence the risk, is unknown. In case of Sondershausen, the development of subsidence on the surface is observed by ground measurements for decades. Therefore, the risk is well known and precautions like backfilling have already been taken. However, for the studies of unknown ground deformations, especially with high deformation rates, such improvements in the model of the subsidence characteristics can increase the confidence of risk assessment.



# Chapter 8

## Conclusions and Outlook

The scope of the work presented in this thesis was designed to address two main objectives. These are (1) the detection of spatio-temporal dynamics of the ground deformation by PSI analysis and evaluation of the feasibility of monitoring with PSI techniques, (2) the derivation of synergistic information implicit in the multi-sensor datasets in order to improve the initially detected characteristics of the displacement. The conclusions that were derived from addressing each of the objectives and an outlook are presented in this chapter. For this purpose, Section 8.1 provides an overview on the different aspects, the key findings and the conclusions drawn based on the study objectives. Finally, the directions for future studies are summarized in Section 8.2.

### 8.1 Summary and conclusions

In this study, the spatial and temporal characteristics of the subsidence induced by mining activities in Sondershausen are investigated by utilizing persistent scatterer interferometry. One of the key elements of this research is the exploitation of multi-sensor SAR data, including ERS-1/2 (1995–2005), ASAR (2004–2010) and PALSAR (2007–2010) acquisitions. The usage of multi-sensor data providing opportunities for synergistic analysis has an impact in both, temporal and spatial dimension. Deriving subsidence rates for multiple time spans enables the extension of the monitoring period as well as the derivation of a more detailed model of temporal evolution. In case of the Sondershausen subsidence, 15 years of continuous monitoring with millimeter accuracy is achieved by PSI analysis of ERS, ASAR and PALSAR data. The estimated rates for the first 10 years by ERS indicate 35 mm/year subsidence. In the following years this value drops to approximately 14 mm/year in ASAR, and 13 mm/year in PALSAR estimations. These values have two implications, (i) the rate of subsidence is decreasing over time, which confirms the effectiveness of backfilling of the mine, (ii) the trend of subsidence is non-linear. Although the PSI analysis is restricted to the estimation of linear deformation rates, the combination of information from different sensors reveals the non-linear nature of the subsidence, which is common

for mining induced subsidence. The spatial distribution of displacement estimations in all sets of PSI results corresponds to an ellipsoidal shape extending from northwest to southeast over the urban areas of Sondershausen with a major axis around 3 km. The spatial patterns observed in the ERS, ASAR and PALSAR deformation maps indicate no major change, which suggests that the subsidence is not affected by a significant geological structure altering the geometry of the subsidence trough.

Also confirmed by the study results, PSI is an effective technique for measuring ground surface movements, however, the accuracy is often degraded due to various reasons. The factors identified in this application contain dependencies on the data configuration, the study site characteristics and the processing methodology. The number and distribution of images in the time series strongly influences the attainable precision of the PSI estimations. The more acquisitions with even distribution are used for the processing, the higher the precision of PSI estimations due to statistical reasons. In this application, the impact of a small number of SAR scenes is especially prominent for the PALSAR stack. Since only 15 images are available, the PSI estimations show lower precision, i.e. the PSI deformation map looks noisy. The ERS and ASAR results are influenced by disfavored distribution of the scenes in time to a lesser extent, i.e. low frequent and irregular acquisitions. One of the important factors dependent of study site characteristics is temporal decorrelation. Due to high decorrelation in vegetated areas, the PSI estimations are mainly limited to urban areas. Owing to its longer wavelength, PALSAR provides higher spatial sampling in vegetated terrain, however, the individual estimations are unreliable due to the low number of images. An important study site and processing methodology dependent factor is the application of a linear subsidence model in the PS analysis. The linear model is not entirely appropriate to describe the subsidence behavior in the study site because the subsidence is non-linear. Since the non-linear component is especially prominent in the period of ERS acquisitions, the impact of this factor is also larger for the ERS result.

The mentioned factors affect the output of PSI analysis with regard to the PS density and distribution as well as the accuracy of the individual measurements. In case of Sondershausen, the validation of the PSI deformation maps and models in reference to the available ground-based measurements indicates a high correlation between these sets of estimations (normalized RMSE values are below 0.112 for the geometric models). However, due to the impact of such factors, the individual PS estimations by PALSAR are unreliable. Furthermore, the ERS result suffers from a lack of PS measurements. Inherently, the models generated for those results are also affected. Therefore, the lowest RMSE is obtained by the ASAR model (0.055) due to its high precision estimations and favorable distribution of the PS measurements. On the other hand, the highest RMSE is calculated (0.112) for PALSAR model due to the deviations in the estimations, although, the general outline of the subsidence trough is estimated efficiently. A lower RMSE value is obtained

with the ERS surface (0.061), however, more critical deviations in the high gradient area are observed.

In order to overcome the limitation of low PS density at the critical areas, a methodology for synergistic utilization of multi-sensor PSI estimations is developed. The strategy implemented here for synergy is designed to increase the number of ERS estimations at the center of the subsidence bowl in order to improve the geometrical representation of the subsidence trough. The method relies on the transfer of points found in the recent acquisitions (ASAR or PALSAR) by scaling their values. Since the observed spatial pattern is constant, in Sondershausen the scaling correlates to the ratio of the geometrical models in the same area belonging to different time intervals. The validation of the refined model suggests an improvement in the correlation of two datasets. The deviation of 5 mm/year in the underestimated area is diminished. The maximum deviation in the overestimated area is also decreased from 15 mm/year to 10 mm/year, implying a correction for the overestimation of the interpolation algorithm due to absence of PS estimations in the vicinity. With these improvements, the RMSE calculated for the ERS surface is increased from 0.061 to 0.054. However, 10 mm/year of difference is still observed. The high deviation persisting after the refinement is caused by the overestimation of the original persistent scatterers found in this region. Due to the presence of the original ERS points, this area is not addressed by the synergy.

Based on these insights, the study indicates that PSI is a powerful technique to study the surface dynamics in Sondershausen, although the analysis is restricted by certain factors. Furthermore, the application demonstrates the potential of synergistic approaches to overcome the common problem of gaps in the PSI results, thereby, to improve the PSI based description of the spatio-temporal behavior of the deformation. Since the effect of subsidence on the surface structures varies spatially along the subsidence profile, the improvements gained by synergy in the estimated subsidence profile will also increase the confidence of risk assessment. Especially the new generation satellites with better resolutions and more frequent acquisitions, furthermore, the new advances in the PSI methodologies and SAR technologies promise developments in the field of deformation monitoring and modeling. Relying on the growing SAR archives and upcoming missions, synergy offers further advancements in the ground subsidence studies.

## 8.2 Future directions

In the coming years, several new space borne SAR sensors will be operating in addition to the new generation satellites already in the orbit. The advanced capabilities of these sensors, e.g. TerraSAR-X, Radarsat-2, Sentinel-1, ALOS-2/PALSAR-2 will increase the reliability of the methods developed in this research. The opportunities of future acqui-

sitions will contribute immensely to the application of ground subsidence monitoring. The contribution includes exploiting the range of radar wavelengths from X-band to L-band and even P-band, deriving more precise estimations by more frequent and stable observations as well as mapping the deformation with more measurements owing to their high resolution. The possibilities of synergistic usage will also increase with every new dataset. Furthermore, the availability of a large number of images and longer wavelengths from new sensors, e.g. L-band ALOS-2/PALSAR-2, stable observations can be collected also in the vegetated areas.

In addition to the opportunities of future acquisitions, the improvements in the PSI analysis can contribute to the precision of subsidence monitoring. For instance, the accuracy of the PSI estimations can be improved by usage of a non-linear model in the PSI analysis. Further effort can be committed to the development of a refinement strategy in temporal dimension. For instance, the temporal evolution of the subsidence can be further studied by fitting a curve to the piecewise linear functions provided by the different sensors. Thereby, the non-linear component can be estimated better. Beside such improvements, the understanding of the surface dynamics can be enhanced by additional information such as geological structures, rock properties, mine geometry and depth. Inclusion of any new data will contribute to the understanding of the deformation characteristics. With the growing potentials of PSI analysis and synergy between multi-sensor datasets in deformation monitoring and modeling, the need for the development of new methodologies also increases. Future researches, therefore, can be devoted to the development of synergistic methods to improve the knowledge of deformation behavior both, in spatial and temporal dimensions.

# Bibliography

- ABDIKAN, S., M. ARIKAN, F. B. SANLI, and Z. CAKIR (2013). "Monitoring of coal mining subsidence in peri-urban area of Zonguldak city (NW Turkey) with persistent scatterer interferometry using ALOS-PALSAR". In: *Environmental Earth Sciences* 71, pp. 4081–4089.
- ADAM, N., A. PARIZZI, M. EINEDER, and M. CROSETTO (2009). "Practical persistent scatterer processing validation in the course of the Terrafirma project". In: *Journal of Applied Geophysics* 69, issue 1, pp. 59–65.
- AO, M., C. WANG, R. XIE, X. ZHANG, J. HU, Y. DU, Z. LI, J. ZHU, W. DAI, and C. KUANG (2015). "Monitoring the land subsidence with persistent scatterer interferometry in Nansha District, Guangdong, China". In: *Natural Hazards* 75, pp. 2947–2964.
- BAMLER, R. and P. HARTL (1998). "Synthetic aperture radar interferometry". In: *Inverse Problems* 14, R1–R54.
- BAUER, R. A. (2008). "Planned coal mine subsidence in Illinois". Tech. rep. Illinois Department of Natural Resources, Illinois State Geological Survey.
- BELL, F. G. (2002). "Geological hazards: their assessments, avoidance and mitigation". Taylor & Francis e-Library.
- BERARDINO, P., G. FORNARO, R. LANARI, and E. SANSOSTI (2002). "A new algorithm for surface deformation monitoring based on small baseline differential SAR interferograms". In: *IEEE Transactions on Geoscience and Remote Sensing* 40, no.11, pp. 2375–2383.
- BLM (2009). "Red Cliff Mine draft environmental impact statement (DEIS)". Tech. rep. U.S. Department of Interior, Bureau of Land Management, Colorado.
- CIGNA, F., B. OSMANOGLU, E. CABRAL-CANO, T. H. DIXON, J. A. AVILA-OLIVERA, V. H. GARDUNO-MONROY, C. DEMETS, and W. DOWINSKI S. (2012). "Monitoring land subsidence and its induced geological hazard with synthetic aperture radar interferometry: a case study in Morelia, Mexico". In: *Remote Sensing of Environment* 117, pp. 146–161.
- COLESANTI, C., S. LE MOUÉLIC, M. BENNANI, D. RAUCOULES, C. CARNEC, and A. FERRETTI (2005). "Detection of mining related ground instabilities using the Permanent Scatterers technique—a case study in the east of France". In: *International Journal of Remote Sensing* 26, no. 1, pp. 201–207.

## *Bibliography*

- CROSETTO, M., O. MONSERRAT, R. IGLESIAS, and B. CRIPPA (2010). "Persistent scatterer interferometry: potential, limits and initial C- and X-band comparison". In: *Photogrammetric Engineering and Remote Sensing* 76, no. 9, pp. 1061–1069.
- DING, X. L., Z. W. LI, J. J. ZHU, G. C. FENG, and LONG J. P. (2008). "Atmospheric effects on InSAR measurements and their mitigation". In: *Sensors* 8, pp. 5426–5448.
- DUNRUD, R. and F. W. OSTERWALD (1980). "Effects of coal mine subsidence in the Sheridan, Wyoming, area". United States Government Printing Office, Washington, USA.
- ERLEBNISBERGWERK-BETREIBERGESELLSCHAFT-MBH (2013). "Erlebnisbergwerk Glückauf Sondershausen, das Bergwerk, Geologie". [www.erlebnisbergwerk.com](http://www.erlebnisbergwerk.com), access: 30.04.2013.
- FALCIDIENO, B., C. PIENOVI, and M. SPAGNUOLO (1992). "Descriptive modeling and prescriptive modeling in spatial data handling". In: *Proceedings International Conference GIS - From Space to Territory: Theories and Methods of Spatio-Temporal Reasoning*, Pisa, Italy, 21-23 September.
- FERRETTI, A., A. MONTI-GUARNIERI, C. PRATI, F. ROCCA, and D. MASSONNET (2007). "InSAR principles : guidelines for SAR interferometry processing and interpretation". ESA Publications, ESTEC, Noordwijk, the Netherlands.
- FERRETTI, A., A. PRATI, F. ROCCA, N. CASAGLI, P. FARINA, and B. YOUNG (2005). "Permanent scatterers technology: a powerful state of the art tool for historic and future monitoring of landslides and other terrain instability phenomena". In: *Proceedings of International Conference on Landslide Risk Management, 18th Annual Vancouver Geotechnical Society Symposium, Canada, 31 May-3 June*.
- FERRETTI, A., C. PRATI, and ROCCA F. (2001). "Permanent scatterers in SAR interferometry". In: *IEEE Transactions on Geoscience and Remote Sensing* 39, no. 1, pp. 8–20.
- FLISS, T., H. MARX, H. THOMA, A. STÄUBERT, A. LINDENAU, and D. LACK (2011). "Back-filling and pillar re-mining in potash industry". In: *Proceedings of MINEFILL 2011 - International Conference on Mining with Backfill, Cape Town South Africa, 21-25 March*.
- FROGER, J. L., Y. FUKUSHIMA, P. TINARD, V. CAYOL, T. SOURIOT, O. MORA, T. STAUDACHER, P. DURAND, B. FRUNEAU, and N. VILLENEUVE (2007). "Multi sensor InSAR monitoring of volcanic activity: the February & April 2007 eruptions at Piton de la Fournaise, Reunion Island, imaged with Envisat-ASAR and ALOS-PALSAR data". In: *Proceedings of FRINGE 2007 Workshop, Frascati, Italy, 26 – 30 November*.
- GE, L., H. C. CHANG, and C. RIZOS (2004). "Monitoring ground subsidence due to underground mining using integrated space geodetic techniques". Tech. rep. Australian Coal Association Research Program (ACARP) Report C11029.
- GE, L., H. C. CHANG, and C. RIZOS (2007). "Mine subsidence monitoring using multi-source satellite SAR images". In: *Photogrammetric Engineering and Remote Sensing* 73, no. 3, pp. 259–266.

- GUÉGUEN, Y., B. DEFFONTAINES, B. FRUNEAU, M. AL HEIB, M. DE MICHELE, D. RAUCOULES, Y. GUISE, and J. PLANCHENAULT (2009). "Monitoring residual mining subsidence of Nord/Pas-de-Calais coal basin from differential and persistent scatterer interferometry (Northern France)". In: *Journal of Applied Geophysics* 69, pp. 24–34.
- HANSSEN, R. F. (2001). "Radar interferometry, data interpretation and error analysis". Kluwer Academic Publishers, Dordrecht, The Netherlands.
- HANSSEN, R. F. (2004). "Satellite radar interferometry for deformation monitoring: a priori assessment of feasibility and accuracy". In: *International Journal of Applied Earth Observation and Geoinformation* 6, pp. 253–260.
- HELENO, S. I. N., L. G. S. OLIVEIRA, M. J. HENRIQUES, A. P. FALCAO, J. N. P. LIMA, G. COOKSLEY, A. FERRETTI, A. M. FONSECA, J. P. LOBO-FERREIRA, and J. F. B. D. FONSECA (2011). "Persistent scatterers interferometry detects and measures ground subsidence in Lisbon". In: *Remote Sensing of Environment* 115, pp. 2152–2167.
- HOOPER, A. (2006). "Persistent scatterer radar interferometry for crustal deformation studies and modeling of volcanic deformation". PhD thesis. The Department of Geophysics, Stanford University.
- HOOPER, A., D. BEKAERT, K. SPAANS, and M. ARIKAN (2012). "Recent advances in SAR interferometry time series analysis for measuring crustal deformation". In: *Tectonophysics* 514-517, pp. 1–13.
- HOOPER, A., P. SEGALL, and H. ZEBKER (2007). "Persistent scatterer interferometric synthetic aperture radar for crustal deformation analysis, with application to Volcan Alcedo, Galapagos". In: *Journal of Geophysical Research* 112, B07407.
- HOPPE, W. (1959). "Exkursionsführer Thüringer Becken, Jahrestagung der Geologischen Gesellschaft in der Deutschen Demokratischen Republik". Akademie-Verlag-Berlin, Berlin, Germany.
- HUNG, W. C., C. HWANG, Y. A. CHEN, J. Y. CHANG, C. P. YEN, A. HOOPER, and C. Y. YANG (2011). "Surface deformation from persistent scatterer SAR interferometry and fusion with leveling data: A case study over the Choushui River Alluvial Fan, Taiwan". In: *Remote Sensing of Environment* 115, pp. 957–967.
- ISAAKS, E. H. and R. M. SRIVASTAVA (1989). "An introduction to applied geostatistics". Oxford University Press, New York, USA.
- JUNG, H. C., S. W. KIM, H. S. JUNG, K. D. MIN, and J. S. WON (2007). "Satellite observation of coal mining subsidence by persistent scatterer analysis". In: *Engineering Geology* 92, pp. 1–13.
- KAMPES, B. M. (2006). "Radar interferometry: persistent scatterer technique". Springer, Dordrecht, The Netherlands.

## *Bibliography*

- KETELAAR, V.B.H. (GINI) (2009). "Satellite radar interferometry: subsidence monitoring techniques (remote sensing and digital image processing)". Springer, Assen, The Netherlands.
- KIRCHER, M., J. HOFFMANN, A. ROTH, B. KAMPES, N. ADAM, and H. J. NEUGEBAUER (2003). "Application of permanent scatterers on mining-induced subsidence". In: Proceedings of FRINGE 2003 Workshop, Frascati, Italy, 1-5 December.
- KRATZSCH, H. (1997). "Bergschadenkunde". Deutscher Markscheider-Verein e.V., Bochum, Germany,
- KUEHL, A., N. SALEPCI, C. THIEL, and C. SCHMULLIUS (2013). "A flexible scoring system to simplify reference scene selection for permanent scatterer interferometry using supplementary data". In: Proceedings of IEEE International Geoscience and Remote Sensing Symposium IGARSS 2013, Melbourne, Australia, 21 - 26 July.
- LAN, H., X. GAO, H. LIU, Z. YANG, and L. LI (2013). "Integration of TerraSAR-X and PALSAR PSI for detecting ground deformation". In: International Journal of Remote Sensing 34, no. 15, pp. 5393–5408.
- LIU, G., H. JIA, R. ZHANG, H. ZHANG, H. JIA, B. YU, and M. SANG (2011). "Exploration of subsidence estimation by persistent scatterer InSAR on time series of high resolution TerraSAR-X images". In: IEEE Journal of Selected Topics in Applied Earth Observations and Remote Sensing 4, no. 1, pp. 159–170.
- LUO, Q., D. PERISSIN, H. LIN, Y. ZHANG, and W. WANG (2014). "Subsidence monitoring of Tianjin suburbs by TerraSAR-X persistent scatterers interferometry". In: IEEE Journal of Selected Topics in Applied Earth Observations and Remote Sensing 7, no. 5, pp. 1642–1650.
- MALZ, A., D. BEYER, S. DONNDORF, P. NAVABPOUR, T. VOIGT, M. AEHNELT, and J. KLEY (2014). "The evolution of the Thuringian Syncline (Central Germany) - an interdisciplinary approach to basin reconstruction". In: Proceedings of EGU 2014, Vienna, Austria, 27 April - 02 May.
- MARX, H., D. LACK, and W. KRAUKE (2005). "Substantial aspects of the recycling of industrial wastes as backfilling material in salt mines". In: Proceedings of 20th World Mining Congress & Expo2005, Tehran, Iran, 7-11 November.
- MASSONNET, D., P. BRIOLE, and A. ARNAUD (1995). "Deflation of Mount Etna monitored by spaceborne radar interferometry". In: Nature 375, pp. 567–570.
- MASSONNET, D. and K. L. FEIGL (1998). "Radar interferometry and its application to changes in the Earth's surface". In: Reviews of Geophysics 36, pp. 441–500.
- MASSONNET, D., M. ROSSI, C. CARMONA, F. ADRAGNA, G. PELTZER, K. FEIGL, and T. RABAUTE (1993). "The displacement field of the Landers earthquake mapped by radar interferometry". In: Nature 364, pp. 138–142.



- MIRANDA, N., B. ROSICH, C. SANTELLA, and M. GRION (2003). "Review of the impact of ERS-2 piloting modes on the SAR Doppler stability". In: Proceedings of FRINGE 2003 Workshop, Frascati, Italy, 1 – 5 December.
- MSB (2007). "A guide to designing for mine subsidence". Tech. rep. Mine Subsidence Board.
- MSE (2007). "Introduction to longwall mining and subsidence". Tech. rep. Mine Subsidence Engineering Consultants.
- NG, A. H-M., H.C. CHANG, L. GE, C. RIZOS, and M. OMURA (2010). "Assessment of radar interferometry performance for ground subsidence monitoring due to underground mining". In: *Earth Planets Space* 61, pp. 733–745.
- NG, A. H-M. and L. GE (2007). "Application of persistent scatterer InSAR and GIS for urban subsidence monitoring". In: IEEE International Geoscience and Remote Sensing Symposium IGARSS, Barcelona, Spain 23-28 July, pp. 1091–1094.
- NG, A. H-M., L. GE, X. LI, H. Z. ABIDIN, H. ANDREAS, and K. ZHANG (2012). "Mapping land subsidence in Jakarta, Indonesia using persistent scatterer interferometry (PSI) technique with ALOS PALSAR". In: *International Journal of Applied Earth Observation and Geoinformation* 18, pp. 232–242.
- NG, A. H-M., L. GE, X. LI, and K. ZHANG (2011). "Monitoring ground deformation in Beijing, China with persistent scatterer SAR interferometry". In: *Journal of Geodesy* 86, pp. 375–392.
- NITTI, D.O., L. DE VITIS, F. BOVENGA, R. NUTRICATO, A. REFICE, and J. WASOWSKI (2010). "Multi-temporal L-band SAR interferometry confirms C- band spatial patterns of subsidence in the ancient Wieliczka salt mine (UNESCO heritage site, Poland)". In: Proceedings of Fringe 2009 Workshop, Frascati, Italy, 30 November – 4 December.
- NSW (2008). "Impacts of underground coal mining on natural features in the Southern Coalfield". Tech. rep. NSW Department of Planning.
- OSMANOGLU, B., T. H. DIXON, W DOWINSKI S., E. CABRAL-CANO, and Y. JIANG (2011). "Mexico City subsidence observed with persistent scatterer InSAR". In: *International Journal of Applied Earth Observation and Geoinformation* 13, pp. 1–12.
- PENG, S. S. (1986). "Coal mine ground control". 2nd. John Wiley & Sons Inc., New York, USA.
- PERSKI, Z., R. HANSEN, A. WOJCIK, and T. WOJCIECHOWSKI (2009). "InSAR analyses of terrain deformation near the Wieliczka Salt Mine, Poland". In: *Engineering Geology* 106, pp. 58–67.
- PRATI, C., A. FERRETTI, and D. PERISSINA (2010). "Recent advances on surface ground deformation measurement by means of repeated space-borne SAR observations". In: *Journal of Geodynamics* 49, pp. 161–170.

## *Bibliography*

- PUERTAS, J. J. G. (2010). "Estimating highway subsidence due to longwall mining". PhD thesis. Swanson School of Engineering, University of Pittsburgh.
- RASPINI, F., C. LOUPASAKIS, D. ROZOS, N. ADAM, and S. MORETTI (2014). "Ground subsidence phenomena in the Delta municipality region (Northern Greece): geotechnical modeling and validation with persistent scatterer interferometry". In: *International Journal of Applied Earth Observation and Geoinformation* 28, pp. 78–89.
- RAUCOULES, D., C. CARTANNAZ, F. MATHIEU, and D. MIDOT (2013). "Combined use of space-borne SAR interferometric techniques and ground-based measurements on a 0.3 km<sup>2</sup> subsidence phenomenon". In: *Remote Sensing of Environment* 139, pp. 331–339.
- RAUCOULES, D., C. COLESANTI, and C. CARNEC (2007). "Use of SAR interferometry for detecting and assessing ground subsidence". In: *Comptes Rendus Geoscience* 339, pp. 289–302.
- RAUCOULES, D., C. MAISONS, C. CARNEC, S. LE MOUÉLIC, C. KING, and S. HOSFORD (2003). "Monitoring of slow ground deformation by ERS radar interferometry on the Vauvert salt mine (France), comparison with ground-based measurement". In: *Remote Sensing of Environment* 88, pp. 468–478.
- ROSEN, P.A., S. HENSLEY, I.R. JOUGHIN, FUK K.LI, S.N. MADSEN, E. RODRIGUEZ, and RICHARD M. GOLDSTEIN (2000). "Synthetic aperture radar interferometry". In: *Proceedings of the IEEE*, vol. 88, no. 3, 25 March.
- ROSENQVIST, A., M. SHIMADA, S. SUZUKI, F. OHGUSHI, T. TADONO, M. WATANABE, K. TSUZUKUC, T. WATANABE, S. KAMIJOC, and E. AOKI (2014). "Operational performance of the ALOS global systematic acquisition strategy and observation plans for ALOS-2 PALSAR-2". In: *Remote Sensing of Environment*, 155, pp. 3–12.
- ROSICH, B., D. ESTEBAN, G. EMILIANI, P. MEADOWS, and B. SCHÄTTLER (2000). "Assessment of the new ERS-2 mono-gyro piloting mode on the quality of ERS SAR data and ERS SAR applications performance". In: *Proceedings of ERS-Envisat Symposium*, Gothenburg, Sweden, 16-20 October.
- RUCCI, A., A. FERRETTI, A. M. GUARNIERI, and F. ROCCA (2012). "Sentinel 1 SAR interferometry applications: the outlook for sub millimeter measurements." In: *Remote Sensing of Environment* 120, pp. 156–163.
- SADEGHI, Z., V. ZOEJ, and M. DEGHANI (2013). "An Improved Persistent Scatterer Interferometry for Subsidence Monitoring in the Tehran Basin". In: *IEEE Journal Of Selected Topics In Applied Earth Observations And Remote Sensing* 6, no. 3, pp. 1571–1577.
- SALVI, S., S. STRAMONDO, G.J. FUNNING, A. FERRETTI, F. SARTI, and A. MOURATIDIS (2012). "The Sentinel-1 mission for the improvement of the scientific understanding and the operational monitoring of the seismic cycle". In: *Remote Sensing of Environment* 120, pp. 164–174.

- SAMSONOV, S. and N. D'OREYE (2012). "Multidimensional time-series analysis of ground deformation from multiple InSAR data sets applied to Virunga Volcanic Province". In: *Geophysical Journal International* 191, issue 3, pp. 1095–1108.
- SAMSONOV, S., N. D'OREYE, and B. SMETS (2013). "Ground deformation associated with post-mining activity at the French-German border revealed by novel InSAR time series method". In: *International Journal of Applied Earth Observation and Geoinformation* 23, pp. 142–154.
- SAMSONOV, S., P. J. GONZALEZ, TIAMPO K.F., and N. D'OREYE (2014). "Modeling of fast ground subsidence observed in southern Saskatchewan (Canada) during 2008-2011". In: *Natural Hazards and Earth System Sciences* 14, pp. 247–257.
- SEIDEL, G. (2003). "Geologie von Thüringen". 2nd. Schweizerbart'sche Verlagsbuchhandlung, Stuttgart, Germany.
- TEATINI, P., L. TOSI, T. STROZZI, L. CARBOGNIN, G. CECCONI, R. ROSSELLI, and S. LIBARDO (2012). "Resolving land subsidence within the Venice Lagoon by persistent scatterer SAR interferometry". In: *Physics and Chemistry of the Earth* 40-41, pp. 72–79.
- TLUG (2005). "Thüringen Untertage". Thüringer Landesanstalt für Umwelt und Geologie, Jena, Germany.
- TRAUTH, M. H. (2010). "MATLAB Recipes for Earth Sciences". Springer-Verlag Berlin Heidelberg, Germany.
- VAN LEIJEN, F.J., V. B. H. KETELAAR, P.S. MARINKOVIC, and R. F. HANSEN (2005). "Persistent scatterer interferometry: precision, reliability and integration". In: *Proceedings of ISPRS Hannover Workshop 2005*, Hannover, Germany, 17-20 May.
- WALTER, D., J. HOFFMANN, B. KAMPES, and A. SROKA (2004). "Radar interferometric analysis of mining induced surface subsidence using permanent scatterer". In: *Proceedings of ESA Envisat Symposium 2004*, Salzburg, Austria, 6-10 September.
- WALTER, D., U. WEGMÜLLER, SPRECKELS V., W. HANNEMANN, and W. BUSCH (2009). "Interferometric monitoring of an active underground mining field with high-resolution SAR sensors". In: *Proceedings of ISPRS Hannover Workshop 2009*, WG I/2, I/4, IV/2, IV/3, VII/2, High-Resolution Earth Imaging for Geospatial Information, Hannover, Germany, 2 - 5 June.
- WEGMÜLLER, U., T. STROZZI, N. BENECKE, L. PETRAT, M. SCHLAUTMANN, R. KUCHENBECKER, J. DEUTSCHMANN, V. SPRECKELS, M. SCHÄFER, W. BUSCH, M. SCHADE, W. PAAR, R. MALY, H. STAISCH, F. HOFFMANN, and A. AL-ENEZI (2007a). "Monitoring mining induced ground-movements using SAR interferometric techniques". In: *Proceedings of Envisat Symposium 2007*, Montreux, Switzerland, 23–27 April.
- WEGMÜLLER, U., T. STROZZI, C. WERNER, A. WIESMANN, V. SPRECKELS, N. BENECKE, and D. WALTER (2007b). "Monitoring of mining induced surface deformation". In: *Proceedings*

## *Bibliography*

- of PI Symposium of ALOS Data Nodes for ALOS Science Program. Kyoto, Japan, 19-23 November.
- WEGMÜLLER, U., D. WALTER, V. SPRECKELS, and C. L. WERNER (2010). "Nonuniform ground motion monitoring with TerraSAR-X persistent scatterer interferometry". In: *IEEE Transactions on Geoscience and Remote Sensing* 48, no. 2, pp. 895–904.
- WEGMÜLLER, U., C. WERNER, T. STROZZI, and A. WIESMANN (2006). "Application of SAR interferometric techniques for surface deformation monitoring". In: *Proceedings of 3rd IAG / 12th FIG Symposium, Baden, Germany, 22-24 May*.
- WERNER, C., U. WEGMÜLLER, T. STROZZI, and A. WIESMANN (2003). "Interferometric point target analysis for deformation mapping". In: *Proceedings of IEEE International Geoscience and Remote Sensing Symposium IGARSS 2003, Toulouse, France, 21-25 July*.
- WERNER, C., U. WEGMÜLLER, T. STROZZI, A. WIESMANN, and M. SANTORO (2007). "PALSAR multi-mode interferometric processing". In: *Proceedings of First Joint PI Symposium of ALOS data nodes for ALOS Science Program, Kyoto, Japan, 19-23 November*.
- WHITTAKER, B.N. and D.J. REDDISH (1989). "Subsidence: occurrence, prediction and control". Elsevier Science Publishers B.V., Amsterdam, The Netherlands.
- WOODHOUSE, I. H. (2006). "Introduction to microwave remote sensing". CRC Press, Taylor & Francis, New York, USA.
- YASEEN, M., N.A.S. HAMM, T. WOLDAI, V.A. TOLPEKIN, and A. STEIN (2013). "Local interpolation of coseismic displacements measured by InSAR". In: *International Journal of Applied Earth Observation and Geoinformation* 23, pp. 1–17.
- YERRO, A., J. COROMINAS, D. MONELLS, and J. J. MALLORQUI (2014). "Analysis of the evolution of ground movements in a low densely urban area by means of DInSAR technique". In: *Engineering Geology* 170, pp. 52–65.
- ZEBKER, H.A., P.A. ROSEN, and S. HENSLEY (1997). "Atmospheric effects in interferometric synthetic aperture radar surface deformation and topographic maps". In: *Journal of Geophysical Research* 10, no. B4, pp. 7547–7563.
- ZHANG, Y., J. ZHANG, H. WU, and S. ZHONG L. GUANGTONG (2011). "Monitoring of urban subsidence with SAR interferometric point target analysis: A case study in Suzhou, China". In: *International Journal of Applied Earth Observation and Geoinformation* 13, pp. 812–818.
- ZHAO, Q., H. LIN, L. JIANG, F. CHEN, and S. CHENG (2009). "A study of ground deformation in the Guangzhou urban area with persistent scatterer interferometry". In: *Sensors* 9, pp. 503–518.
- ZHOU, X., N. B. CHANG, and S. LI (2009). "Applications of SAR interferometry in Earth and environmental science research". In: *Sensors* 9, pp. 1876–1912.

# Appendix A

## Complementary Figures

Appendix A Complementary Figures

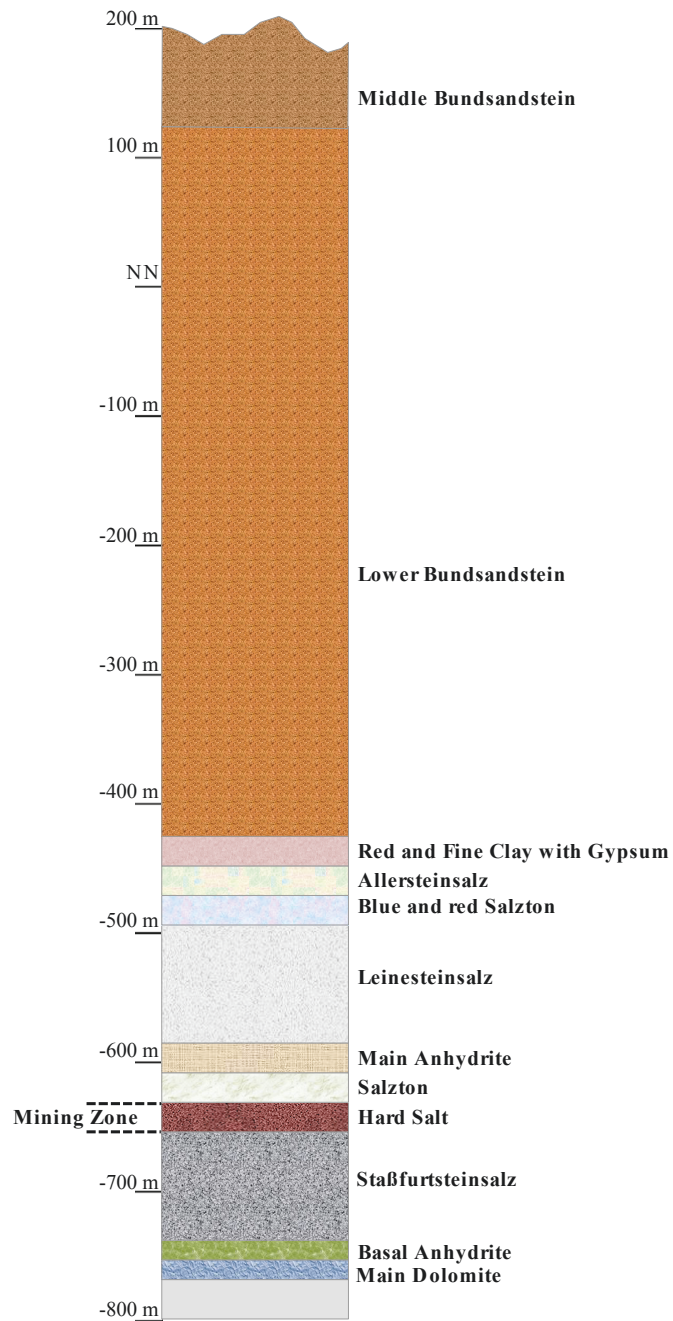


**Figure A-1:** Geological columnar section at the research site drawn based on the illustration by ERLEBNISBERGWERK-BETREIBERGESELLSCHAFT-MBH [2013].

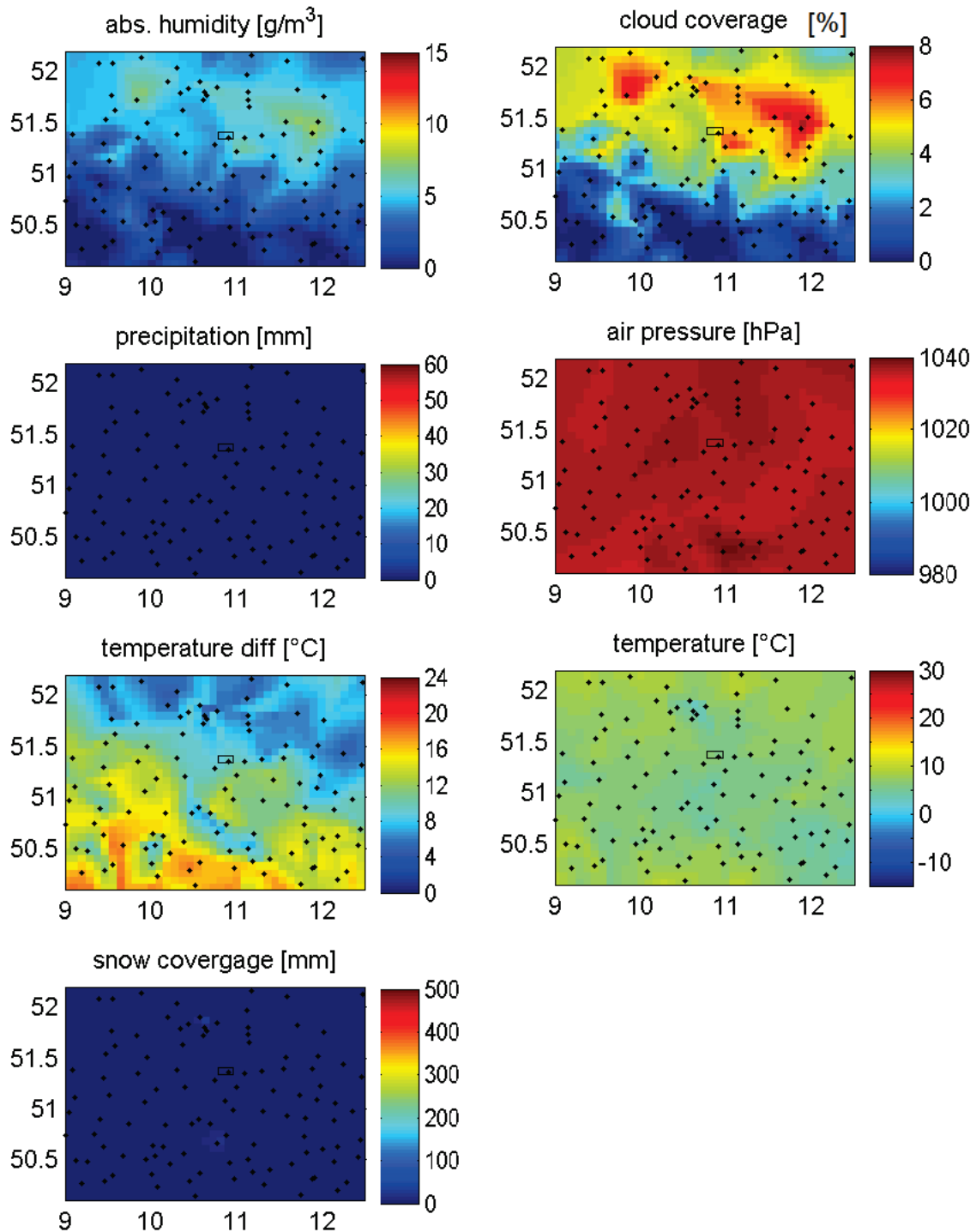


**Figure A-2:** Weather parameter maps of the master scene of the ERS stack acquired in 09.03.1997. The dots represent the weather stations and the rectangle indicates the study site. The units are provided in the title of each plot. The maps are generated by interpolation of the values acquired at that day by the weather stations.

Appendix A Complementary Figures

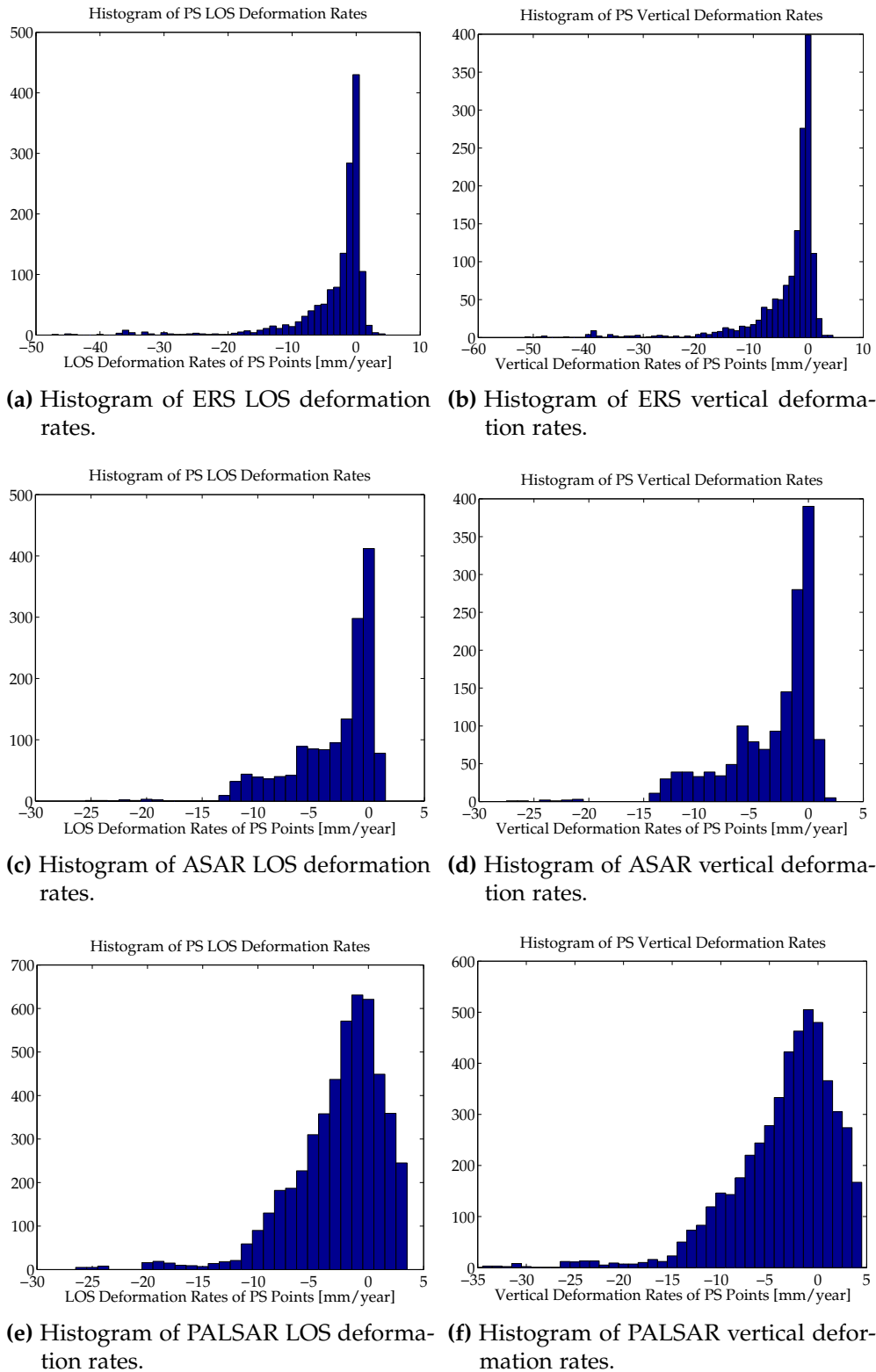
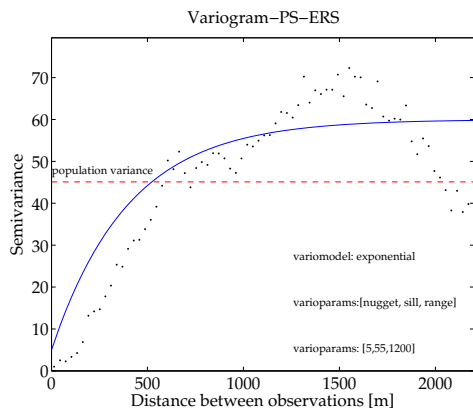
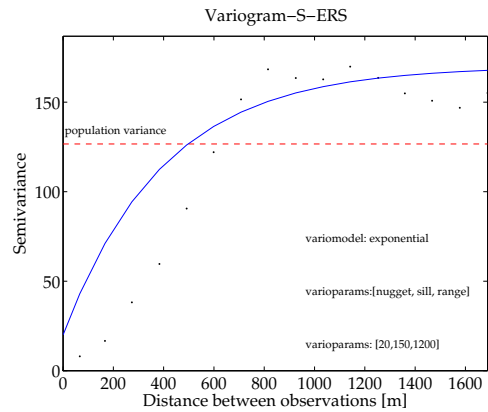


**Figure A-3:** Histograms of the ERS, ASAR and PALSAR stacks for LOS and vertical deformation rates.

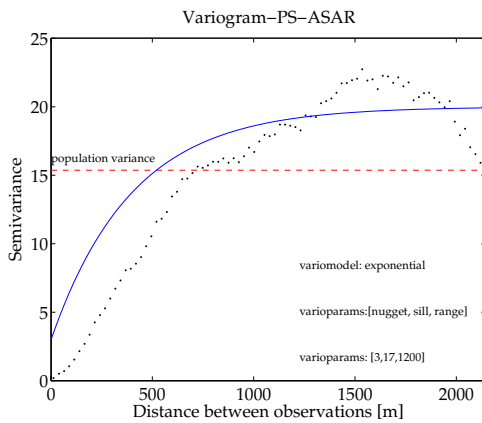




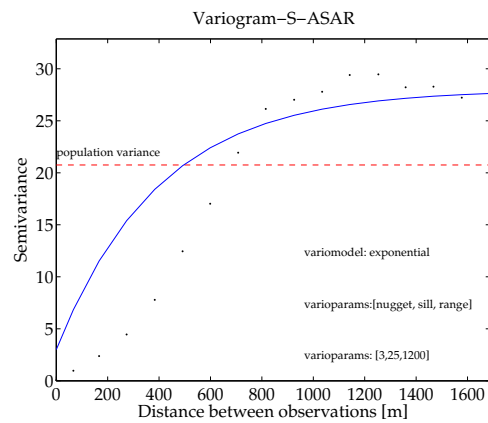
(a) Variogram of ERS PS surface



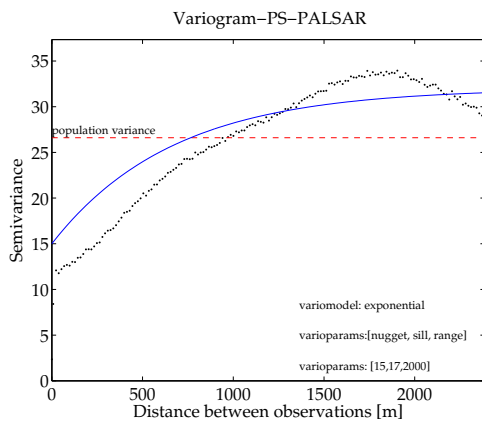
(b) Variogram of ERS surveying surface



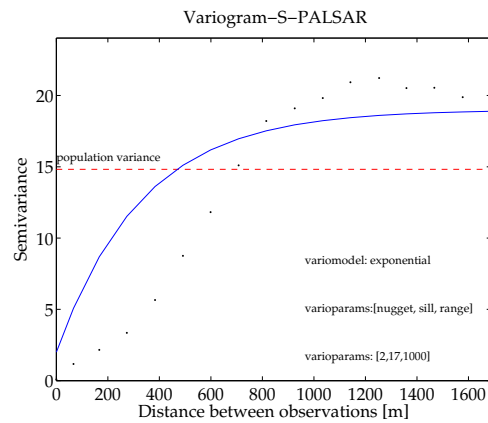
(c) Variogram of ASAR PS surface



(d) Variogram of ASAR surveying surface.



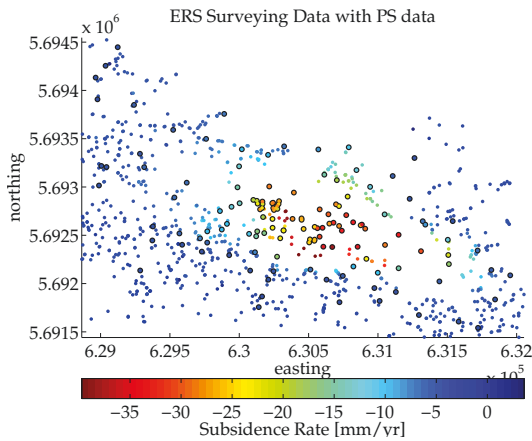
(e) Variogram of PALSAR PS surface



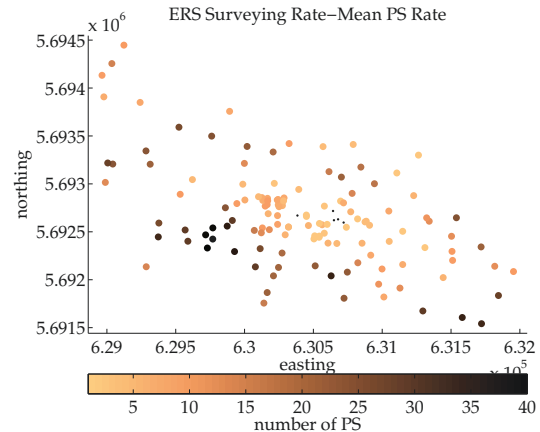
(f) Variogram of PALSAR surveying surface.

**Figure A-4:** Variograms of PS and surveying surfaces for the ERS, ASAR and PALSAR stacks. The blue curve is the model function with the parameters printed on the plots.

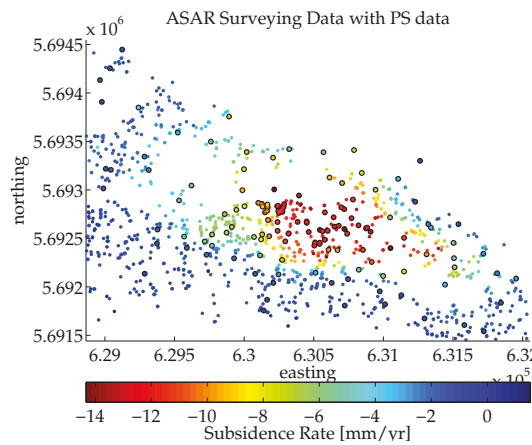
Appendix A Complementary Figures



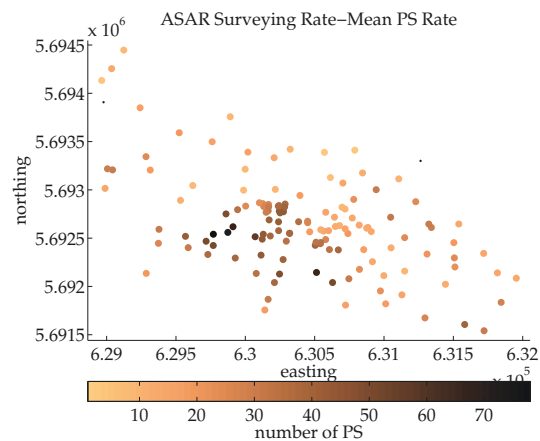
(a) Plot of ERS PS and surveying points



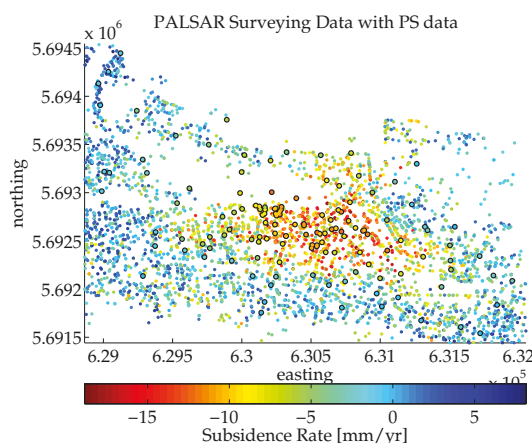
(b) Plot of number of ERS PS points used for comparison.



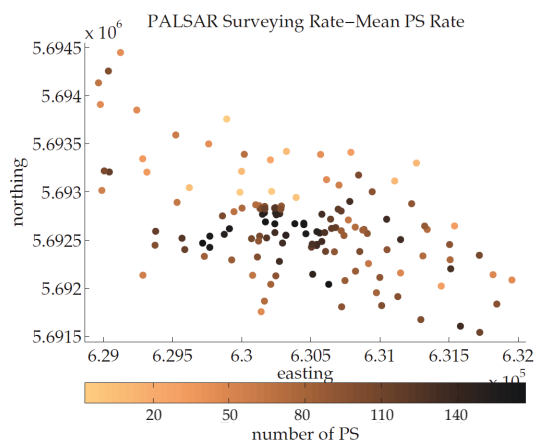
(c) Plot of ASAR PS and surveying points



(d) Plot of number of ASAR PS points used for comparison.



(e) Plot of PALSAR PS and surveying points



(f) Plot of number of PALSAR PS points used for comparison.

**Figure A-5:** Plots on the right column show the relative distribution of PS and surveying points (with black frame). The left column of plots indicate the number of PS points used for the calculation of the mean at surveying benchmarks .

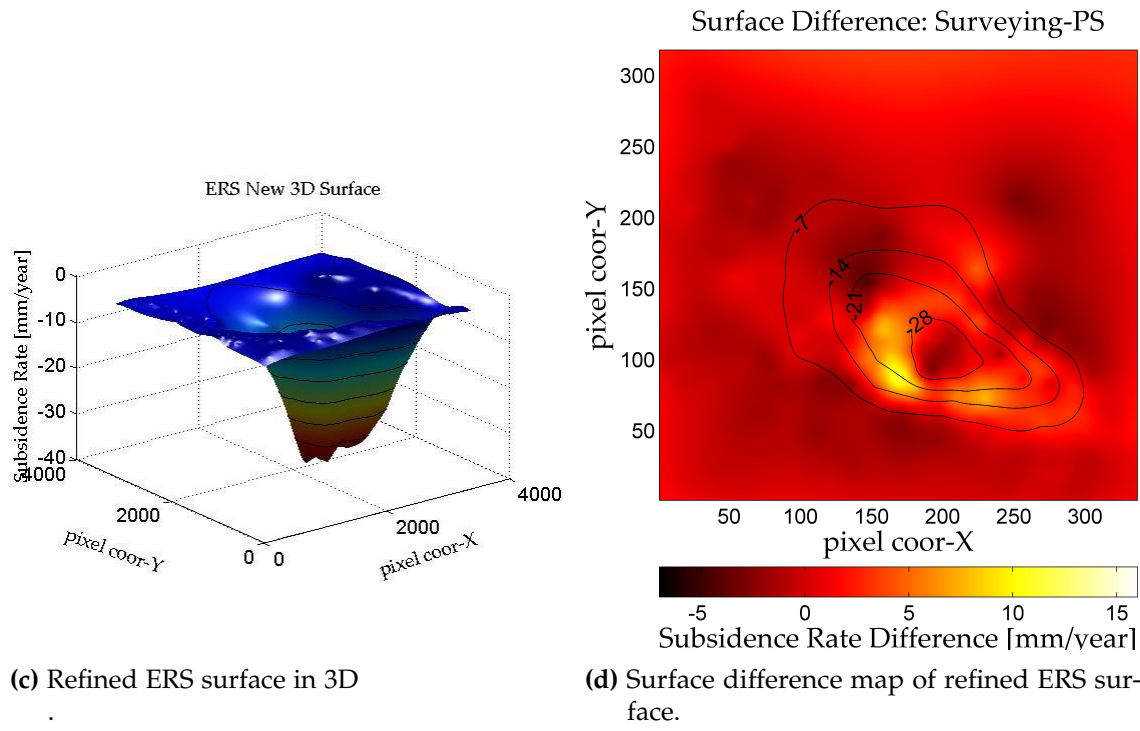
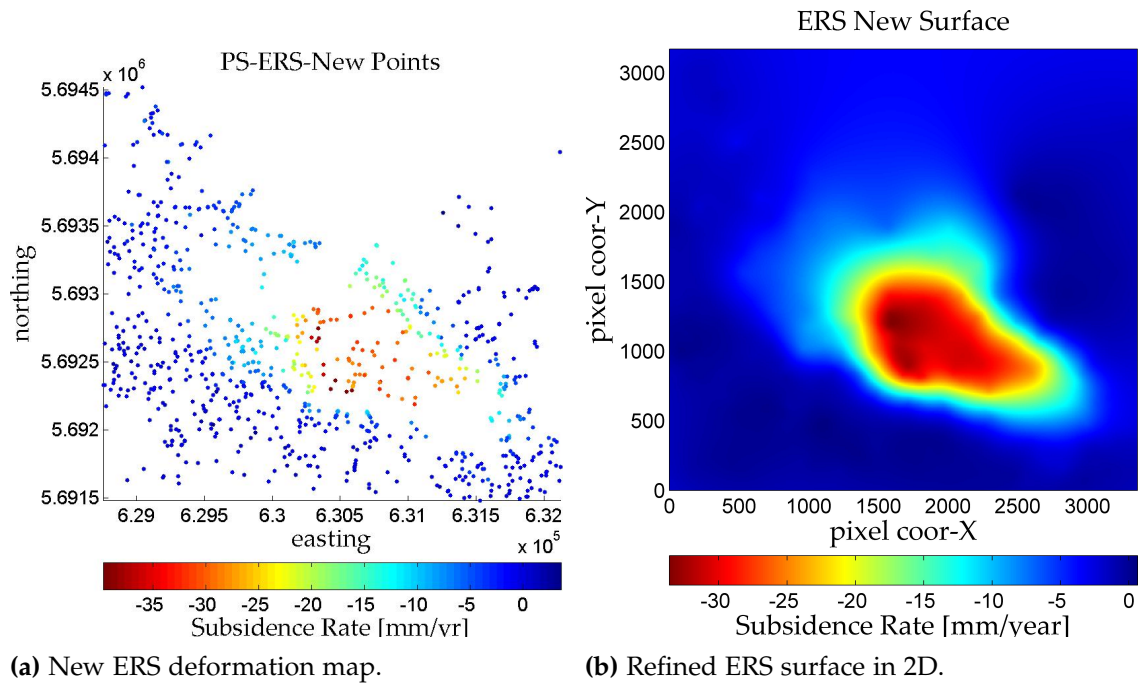
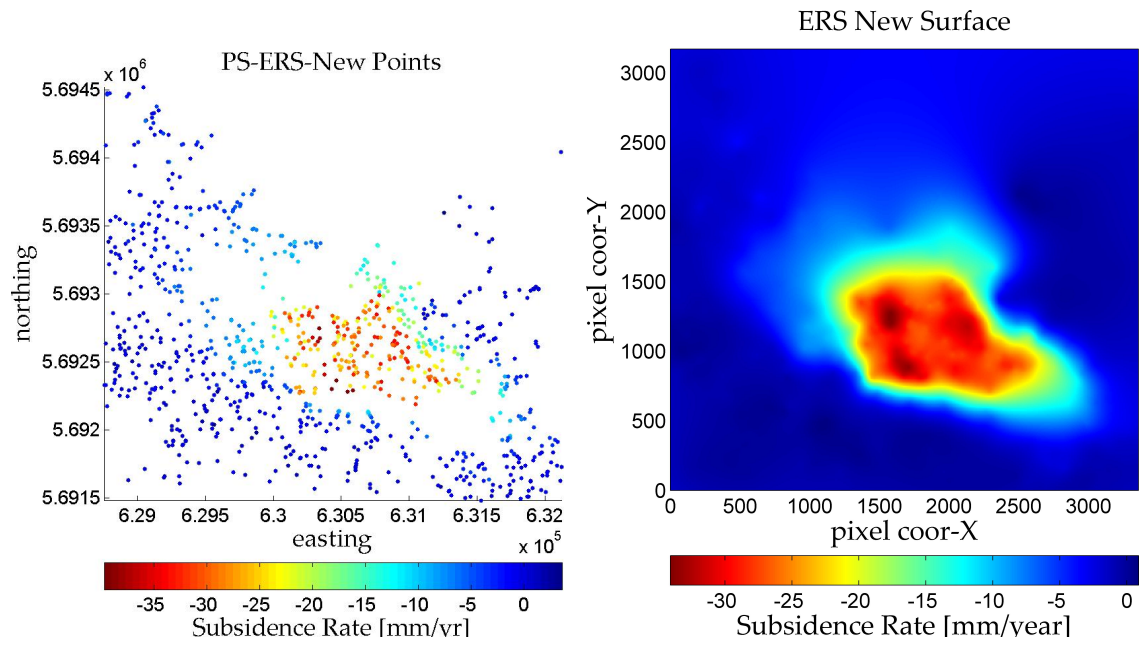


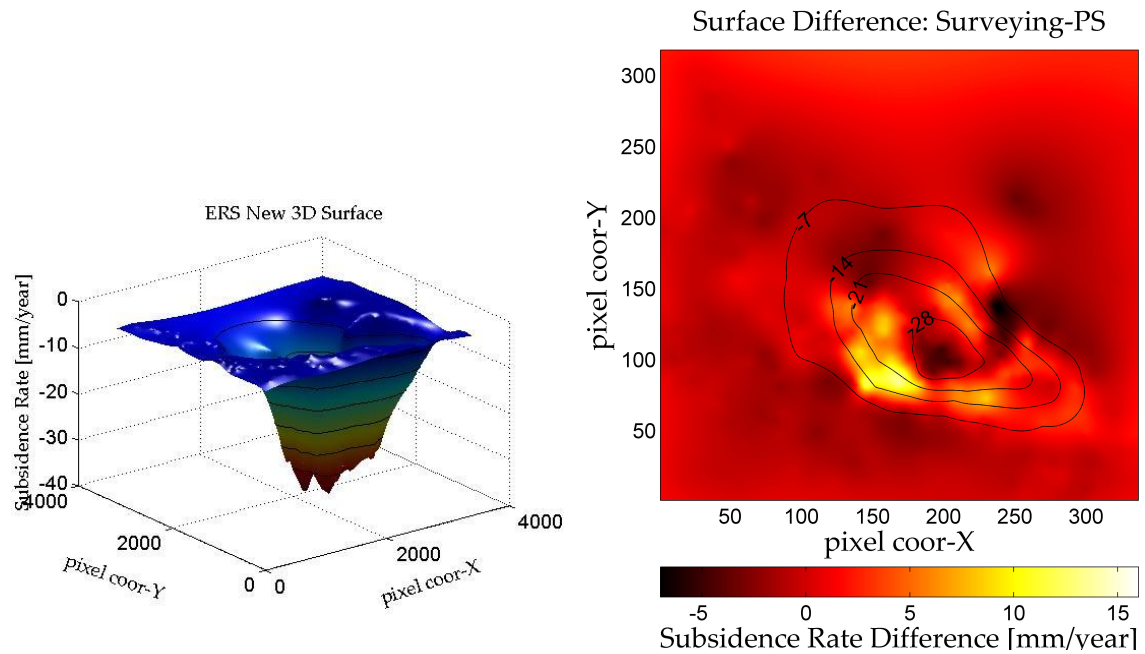
Figure A-6: Results of ERS-ASAR integration for three clusters.

Appendix A Complementary Figures



(a) New ERS deformation map.

(b) Refined ERS surface in 2D.



(c) Refined ERS surface in 3D

(d) Surface difference map of refined ERS surface.

Figure A-7: Results of ERS-PALSAR integration for three clusters.

# Selbständigkeitserklärung

Ich erkläre, dass ich die vorliegende Arbeit selbständig und unter Verwendung der angegebenen Hilfsmittel, persönlichen Mitteilungen und Quellen angefertigt habe.

Jena, 24.09.2014

Unterschrift der Verfasserin

A handwritten signature in black ink, appearing to read 'Nesrin Salepci', with a stylized flourish at the end.

Nesrin Salepci